TEST RIG DESIGN TO SIMULATE ASHLOCK VALVE EROSION IN COAL GASIFICATION SYSTEMS

by

SIMON WILLMOTT

A thesis submitted to the Faculty of Engineering, University of Cape Town in fulfilment of the degree of Master of Science in Applied Science.

Department of Metallurgy and Materials Science.

January 1984.

ACKNOWLEDGEMENTS

I wish to thank all those who assisted in the realization of this research project. Special thanks are extended to:

My supervisor, Professor Tony Ball, for his encouragement and guidance.

Charlie Forse, who assisted with the design.

Nic Dreze, Reggie Hendriks and James Peterson in the workshop.

Andy Rapley for his considerable effort and practical assistance throughout the duration of the project.

Helgard Böhm and Anne Squires respectively for the diagrams and efficient typing and preparation of the script.

Bernard Greeves for his darkroom expertise.

My colleagues in the Department for their support.

The sponsors of this research for their patience and financial assistance.

ABSTRACT

The erosion of ashlock hopper valves in coal gasification systems, and the maintainance downtime resulting from this erosion, is a cause of considerable concern to the coal conversion industry. After an assessment of the factors considered relevant to solid particle erosion as presented in literature, a design for a laboratory test apparatus to closely simulate the in-service problem was proposed. A test rig prototype, reproducing service conditions of temperature, pressure and geometry, was constructed and preliminary testing conducted. Various problems impairing the efficient operation of the test facility became apparent and these, together with the proposed solutions and modifications to the prototype rig, are discussed. Both room temperature and elevated temperature (400°C) erosion tests were conducted on the hardfacing seat material presently used on site as well as a on selection of common engineering materials. Optical and scanning electron microscopy (SEM) studies revealed a close correlation between in-situ and laboratory erosion damage, suggesting that the test apparatus is a valid simulation of the service problem.

In all materials tested, a reduction in erosion rate was observed with increasing test temperature. An investigation into the effect of various heat treatments on the erosion rate of a medium carbon steel standard (080M40) was also conducted. The specimen rates were found to be indepenent of microstructural changes induced by thermal treatments, although these treatments resulted in up to threefold hardness increases in this steel. Further, the effect of changing the seat/cone inlet angle on erosion rate was investigated. It was noted that the angle change affected the specimen mass loss most detrimentally at 30°, with the presently used 45° angle giving least erosion loss.

The eroded surfaces of selected specimens were examined by optical and SEM in a preliminary attempt to characterize and quantify the surface damage in terms of previously proposed material removal mechanisms.

Limited preliminary testing was performed on selected 'special' materials and the results are discussed. A brief discussion, based on the experience gained during this work, of an alternate test rig design is also presented.

CONTENTS

CHAPTER ONE

INTRODUCTION

Material loss by the impact of gas-borne abrasive particles has plagued industry for many years. Coal conversion systems and, more recently, the aerospace industry, have been noted to be especially susceptible to general materials' problems and more pertinently, materials erosion due to severe, high tolerance operating conditions.

While much research has been conducted in the field of erosive wear, the diversity of operating conditions and environments in erosion situations make a simple analysis of the problem impractical. Over the years, researchers have worked to isolate and correlate the variables affecting erosion and, in a number of cases, have proposed 'models' or equations by which erosion rates may be estimated. However, equations have been found to be of limited practical significance to plant engineers who require a more direct approach and solution to their problems.

In continuous-operation coal gasification plants, any unscheduled shutdown of a gasifier manifests itself as a financial loss. Such problems exist as a result of erosion of both top and bottom lockhopper valves of ashlocks in gasification plants. A schematic representation of a typical gasifier layout is presented in Figure 1.1. The continuous coal-burning process at elevated temperature and pressure to extract resultant hydrocabon gases, necessitates a sequential operating procedure as specified overleaf.

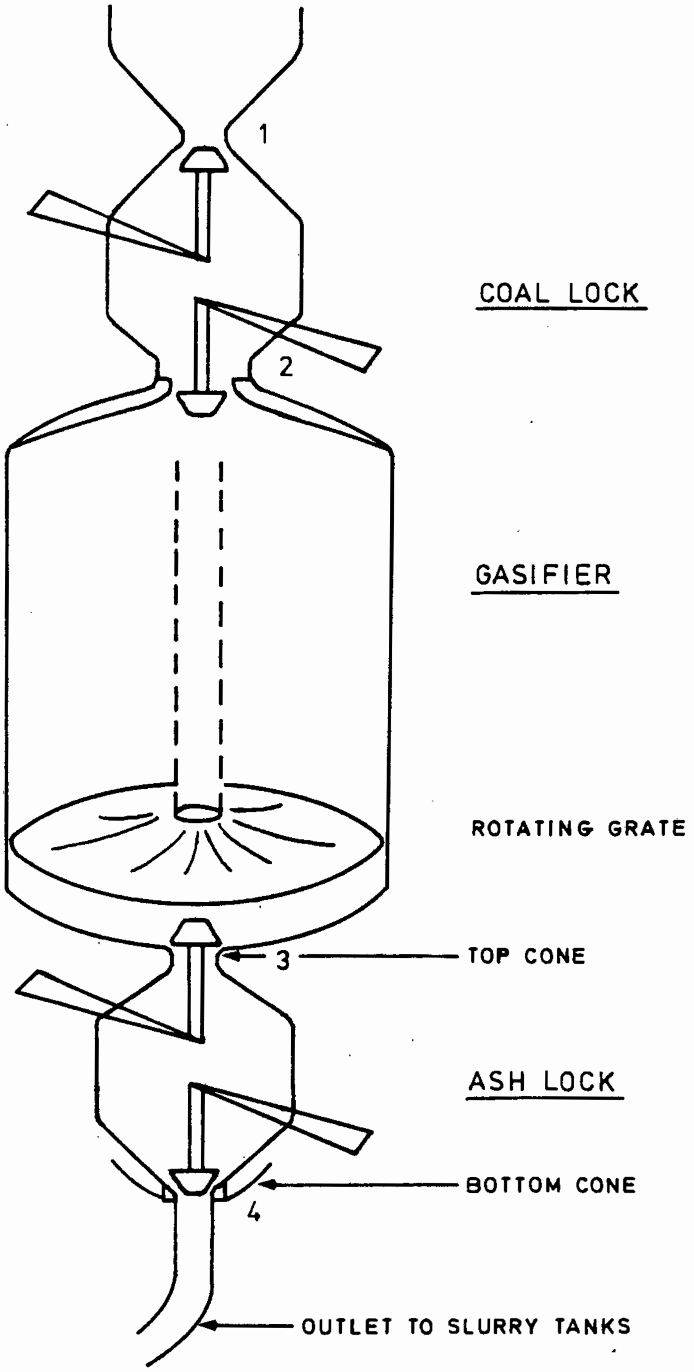

FIG: 1.1 Schematic gasifier and ashlock configuration showing position of top (3) and bottom (4) valves.

With reference to Figure 1.1:

1. Valves 2 and 4 closed, 1 and 3 open.
2. Charge coal lock.
3. Seal valve 1 and pressurize coal lock to 2,5 MPa working pressure with high pressure steam.
4. Open valve 2 to charge gasifier.
5. Close 2 and de-pressurize coal lock.

The de-ashing procedure continues:

6. When ash lock is full (ash and clinker from burning process), seal 3.
7. Depressurize ash lock.
8. Open ash lock bottom cone (4) to de-ash vessel (gravity feed).
9. Reseal 4 and pressurize ash lock.
10. Open 3.

This de-ashing process, approximately every twenty five minutes, results in a periodic pressure differential of 2,5 MPa (368 psi) across valves 3 and 4 (Figure 1.1).

The hydraulic valve closure system is manually operated, and therefore efficient seating is largely dependent on operator skill, experience and application.
The problem therefore is severe erosion of the 450 mm diameter valve seat by ash particles due to misalignment of the seat and cone sections, this erosion being aggravated by the aggressive environment of pressure and temperature. The progressive degeneration of the valve seat leads ultimately to failure of the valve after periods of between two and sixty days (Figure 1.2). Although both the top cone and bottom cone valves are similarly affected by the erodent ash, the bottom valve can be replaced with the gasifer remaining in operation, while the top seat requires total gasifer shut-down before maintainance may be affected.

FIG: 1.2 Erosion damage on a failed in-situ valve seat.

Initially investigation of the problem required an analysis of operating conditions and an indication of the initiation and progress of the valve erosion. The latter unknown may be portrayed as the two extreme plots of erosion versus service life in Figure 1.3.

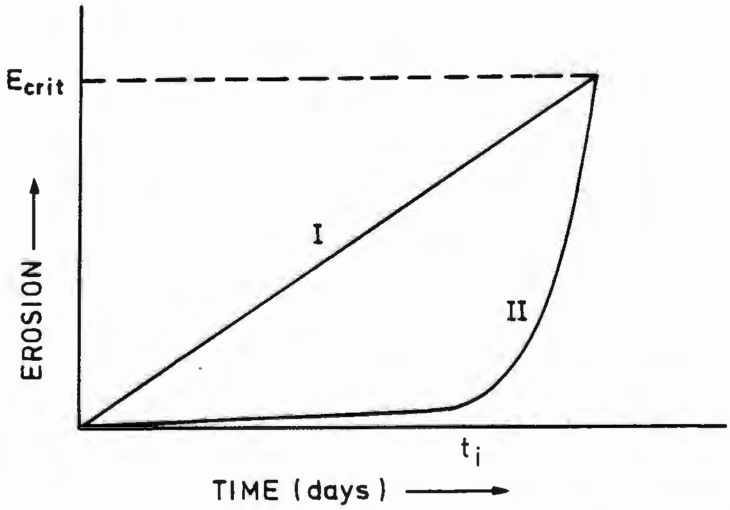

FIG: 1.3 Plot of seat erosion versus time showing two possible erosion paths (I and II) to valve failure at E_{crit}.

Curve I suggests a steady state seat erosion loss from installation while curve II intimates a definite erosion initiation event at t_i, followed by rapid and severe material loss until valve failure at some critical erosion value, E_{crit}. In the event of a "Curve II" situation predominating, the rapidity of material loss makes it unlikely that any known material would resist erosion to any significant degree. Acoustic emission results, however, taken from the seat area, revealed a steady state situation as suggested by plot I to prevail. In this case the choice of material could have a very significant influence on the (slope of the dE/dt) rate of erosion.

The undesirability of in-plant material trials without any prior guidelines from laboratory studies, is self-evident. Downtime during installation and the risk of unknown materials performances are financially unacceptable. Due to the noted diversity of erosion conditions, a survey of the relevant literature would also have limited independent benefit. As a result, a laboratory simulation of the problem was considered as a means of investigating the viability of suggested erosion resistant materials as well as possible seat/cone geometry changes. The primary advantage of a laboratory simulation of an in-service component condition is the capacity for accurate variable control, thereby obtaining an accurate assessment of a materials performance under specific conditions without jeopardizing production. The feedback from such a project may thus be directly applied to the plant and thereby supplement the understanding of the problem while improving efficiency.

This programme was therefore initiated to reduce the ash lock valve erosion, primarily via materials investigation, but also in terms of limited valve geometry change. A preliminary review of the relevant literature revealed parameters such as, inter alia, erodent, geometry and aerodynamic effects to play an important role in the erosion performance of materials (Chapter 2).

As a result of this conclusion, together with the uncertainty expressed by some authors as to the validity of erosion test rig results with regard to environmentally diverse in-situ problems, it was deemed imperative to duplicate the service conditions in the test apparatus exactly. This approach is supported by the unavailability of certain relevant data relating to the in-situ erosive conditions. These unknowns include such factors as ash flow rates through the initiated erosion tubes and the velocity of the erodent particles entrained in the carrier gas. It was envisaged that it would only be by careful reproduction of the service conditions of pressure, temperature, erodent and geometry, that these 'unknowns' could be most readily and faithfully modelled in the laboratory.

CHAPTER TWO

LITERATURE REVIEW

Before embarking on a erosion design project of this nature, a survey of the relevant literature is mandatory in order to assess the state of the art and, in particular, to identify the physical parameters that influence the erosion of materials, and to estimate their relative importance. Furthermore, it is necessary to investigate the erosion apparatus designs currently in use, noting the design requirements of the present research.

A great deal of work on erosion is primarily motivated towards understanding the fundamentals of erosion by way of noting the effect of changing the erosion parameters as well as by mechanistic studies. It is therefore desirable, even in less theoretical studies such as the present, to include the current thinking of researchers as regards erosion mechanisms and the suggested materials selection to combat erosive wear.

As a result, the literature review was approached so as to address four questions :

- (i) what variables are deemed significant when considering solid particle erosion, and what influence do they have on erosion rate,
- (ii) what experimental rigs have been constructed to simulate erosion
- (iii) what material removal mechanisms have been proposed, and
- (iv) what are the current approaches to erosion prevention

2.1 VARIABLES AFFECTING PARTICULATE EROSION

The factors influencing erosion may be divided into four groupings as presented below, and while approached individually in this review, the variables may interact and affect the relative importance of other parameters.

2.1.1 ERODENT VARIABLES

2.1.1.1 Size

Apart from the fundamental influence of size on erosion rate found by various researchers and presented in this section, the particle size has been found to influence the flow pattern and consequently the velocities attained in two-phase air-erodent flow streams. These effects are approached in more detail in subsequent sections.

I.M. Hutchings (1) has suggested that the particles responsible for erosion lie typically within the size range of 5 to 500μm. Indeed, with few exceptions, most research using laboratory testing rigs has been conducted with erodent particles within this range. However erosion studies have been approached using macro-particles. These include the use of 5 mm to 6 mm chromium steel "particles" (2), 3 mm diameter ball bearings (3), and 3 mm diameter steel balls (4). The validity of these experiments are based on the findings of various researchers who assert that erosion is independent of particle size effect greater than approximately 200μm.

Notwithstanding this assumption, doubts as to the validity of macro-scaled tests have been aired (5,6). The presence of a particle size threshold above which increasing particle size has little effect has been postulated by various authors (7,8,9,10).

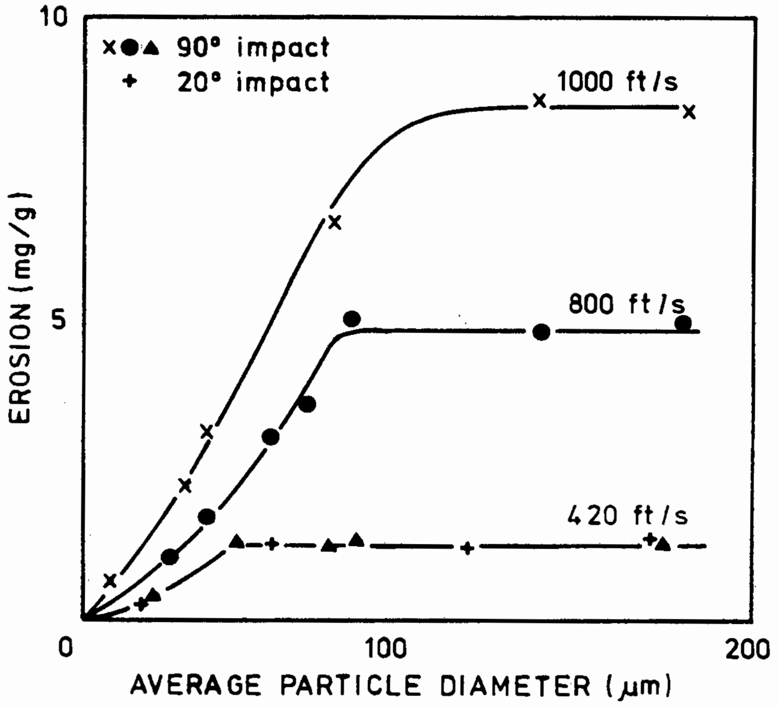

FIG: 2.1 Variation of erosion with particle size at various impingement velocities and angles. (After Hansen et al (17)).

This size threshold has been suggested at 100μm (11) while other authors (12) found an increase in erosion with particle size up to 300 μm for a constant velocity. Certain contention is apparent in these findings as Bhattacharyya, Yates and Hill (13), in an erosion-corrosion test series using "coarse" (630μm mean) and "fine" (127 μm mean) erodent fractions, reported little effect of particle size on erosion.

Similarly (14), in a study of particle erosion on pipe bends, particle size was found to have no effect on the erosion rate, influencing only the erosion pattern. The proponents of a particle size threshold all noted that the erosion rate decreases with decreasing particle size below the theshold limit (Figure 2.1). Reasons put forward for this behaviour include reduced target surface temperature rises (increases) as the erodent size decreases (10), and a reduction in input energy of each particle (12) resulting in less erosive loss. Physical reasons for the theshold size effect, as suggested by various authors, have been noted by Finnie (11).

Having noted the implications of particle size variation, the importance of the particle size distribution within a sample is evident. Erodent size distribution within a sample may result in extraneous test results in addition to the nominal size effect. The importance of size distribution has been stressed (8), not only as a fundamental size effect, but also the "large effect" of the airflow in gas-blast type testers where the large particles accelerate more slowly and the fines tend to follow the flow lines of the gas stream and fail to impact. The influence of size distribution on the number of particles actually impacting on the erosion surface is also presented by Gat and Tabakoff (15), while it is further emphasized (16) that particle size is a critical factor relating to particle velocity due to size-induced accelerating variation and, as such, accurate control of the size distribution is necessary to reduce velocity variations during testing.

2.1.1.2 Shape

There is general agreement between researchers as to the importance and effect of erodent particle shape. Hansen, Kelly and Wood (17) state that "sharp particles produce greater erosion in ductile materials than do rounded particles." The shape or "sharpness" of impacting particles is also noted as important (8,18), while in erosion testing with equal masses of glass beads and crushed glass of average diameter of 15μm, Salik and Buckley (19) found the erosion rate strongly dependent on particle shape, the erosion loss being an order of magnitude higher with crushed glass.

The importance of careful control of erodent shape during laboratory tests was highlighted (14) in erosion testing of pipe bends. Using sand as the erodent, four times the erosion was observed using fresh sand compared to testing using previously run sand. Scanning electron microscopy revealed considerable 'rounding off' of the sand after an initial test run, this roundness accounting for the decreased erosion rate.

A more theoretical approach to particle shape has also been taken by some researchers. The strong dependence of the configuration of the leading surface of the impacting particle on erosion was reported (6). These workers distinguished between "flat" or "corner" impact strikes for angular incident particles as shown schematically in Figure 2.2 overleaf.
The importance of this "rake" angle was similarly noted in (2) and (20). Further, the orientation of the erodent particle on impact or the "attack angle" or erosion was used as the basis of a mechanistic

study of the transition from material removal by ploughing to cutting in erosive wear by Gane and Murray (21).

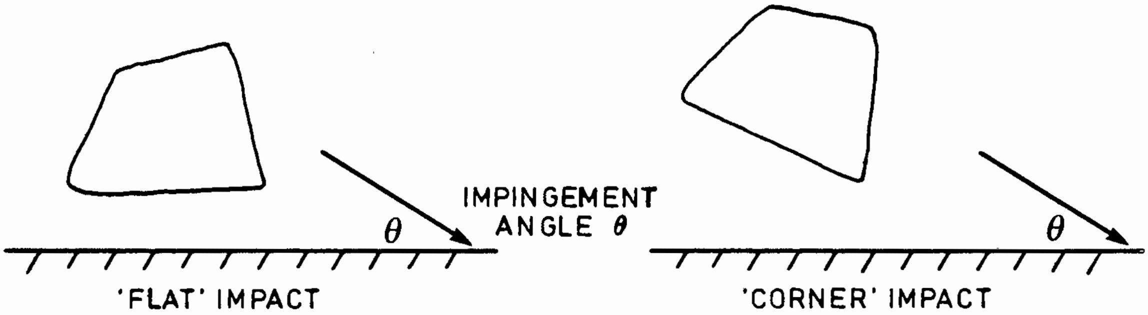

FIG: 2.2 Schematic representation of different particle orientations on impact thereby affecting particle 'shape'.

Particle shape has also been investigated in terms of effect in two-phase gas/solid flow. In a study on the particle size distribution on high speed flow, it was found (22) that irregular shaped quartz particles may change the drag coefficient of the entrained medium, thereby introducing error into the two-phase flow analysis and affecting particle velocities. Having considered the effects of particle shape on erosion, notwithstanding the 'acedemic' analysis of rake angles on impact, any erosive environment, laboratory or industrial, will be highly influenced by this parameter.

2.1.1.3 Hardness

Erosive particles, although varying in composition, dimensions and shape, are almost universally harder than the material which they erode. Although 'softer' particles do erode hard materials as in the case of rain erosion of windscreens in supersonic aircraft, particulate erosion problems in industry are almost exclusively due to the impact of 'hard' particles on 'softer' targets. Hutchings (1) suggests that the hardness of the eroding particle only becomes important if the hardness of the material being eroded approaches one half that of the grit. Other authors (17) go further, stating that erodent hardness will not influence the erosion of ductile materials provided the particles are harder than the material they are striking. Conversely, it was determined (18) that erosion rate increased with increasing particle hardness to a constant rate for particles with $H_v > 700$ kgfmm^{-2}, the constant rate being attained when the particles were strong enough not to fragment on impact. In experiments using both alumina (Al_2O_3) and Arizona desert dust, the harder alumina was found to be more erosive than the desert dust (6). However, factors such as size distribution, shape, and chemical composition may also influence results of this nature.

Finally softer particles appear more susceptible to fragmentation on impact, thereby introducing a possible secondary erosion mechanism (section 2.3) of lip removal by radially flung fragments. Therefore, the hardness of the erodent should be kept constant in a controlled laboratory environment to forestall potential errors due to this variable.

2.1.1.4 Chemical composition

The hardness of the erosive particles, as well as the shape of both the original particle and any subsequent fragments issuing from it on impact, may be a function of the chemical nature. Varying particle types (FMC, Husky Char and dolomite) gave differing erosion rates (13), while in a study using silicon carbide (SiC) and ash as erodents, it was suggested (7) that ash could give differing results in erosion tests. Within the particle types tested, authors found certain abrasives to give enhanced erosion over others. Workers (23) have reported that erosion by Al_2O_3 particles is more severe than that of coal ash of nominal composition 45% SiO_2, 27% Al_2O_3 and 28% oxides. This observation was the result of the ash being more friable and susceptible to break up on impact. Raask (24) concluded that the abrasiveness of coal ash depends mainly on the quartz and pyrite fractions which similarly break into sharp-edged fragments on impact. The increased erosion of materials with increasing quartz contents of dust is also proposed (8). These authors further propose that erosion studies should be conducted with quartz particles as the major fraction of the erodent in order to minimize any discrepencies arising from variations in chemical composition of the erodent. When considering erosion in coal gasification environments therefore, it is important to note the ash contents of the particular coals used in the burning process. Coal used in South African applications may approach a relatively high ash content of 35% by weight, compared to a number of British coal-fired power stations using coal of 18 to 20% ash by weight. This feature should thus be considered when selecting an erodent material for a laboratory test rig application.

2.1.1.5 Mass

The mass or concentration of erodent describes the amount of particles impinging on the target surface during the period of an erosion test. Intuitively, it would appear that an increase in the amount of erodent or number of impacting particles would result in a proportional increase in the erosion rate. While this approach is valid in many instances, literature has also shown anomalous results as regards ash flow rate on erosion. Based on the assumption that each particle plays an effective role in erosion at the target surface, the specimen erosion loss in mgs is directly proportional to the mass of erodent used (1). A similar result was observed (17) when, at 'low concentrations' an increase in erosion with increased particle flux was recorded. However, at 'high concentrations' the authors reported a decrease in erosion efficiency due to a suggested energy loss resulting from particle/particle interactions. This explanation is supported by authors (6) who state that for a given weight of dust at both room temperature and at 371°C, the erosion produced increases with decreasing dust concentrations. Others (12), however, reported concentration to be unimportant in their test series. Although a 'small' concentration effect was noted by Finnie (11), it was felt that, to date, no satisfactory explanation had been offered as regards the erodent mass effect. The situation is further confused in work on the erosion of polymer coatings (25), where it was reported that in two thirds of the specimens tested, the erosion rate was independent of the mass of impacting sand at a constant impingement angle.

While energy loss due to particle interactions at high concentrations has been suggested (17), a more practical approach was forwarded (16), maintaining that although the nominal concentration or ash flow rate may be controlled, transients occuring during a test run are essentially non-controllable. These differences may, therefore, influence the resultant erosion data.

It would thus appear that in sandblast-type erosion testers the particle flow rate can vary and therefore could affect results. This could be due to particle energy losses on colliding, to transients in the erodent flow or due to fluctuating two-phase flow patterns resulting in aerodynamic changes.

2.1.1.6 Fragmentation

The importance of fragmentation or degradation of particles on impacting an erosion surface has been noted both as a prospective material removal mechanism and in terms of resultant fragment shape. Fragmentation has been reported by a number of authors (8, 11, 23, 26, 27). Quartz (SiO_2) particles have been shown to undergo considerable breakup (8, 26) as does 270 μm diameter steel shot (28) and fly ash (23). However, alumina (Al_2O_3) particles seem less prone to fragmentation as reported by various authors (23,28) who reported no clear differences in particle dimension before and after erosion. The relevance to laboratory testing is due to the incidence of sharp angular fragments issuing from the original particle as reported occuring in quartz (24), and influencing erosion results.

2.1.2 FLOW CONDITIONS

2.1.2.1 Gas/particle velocity

On examining the effect of particle velocity on erosion, it should be remembered that the velocities of the carrier gas and the erodent need not necessarily be the same. Factors such as shape and size of particles, particle interactions and aerodynamic flow patterns (Sec.2.1.2.3) all serve to affect the final erodent velocity within the gas stream. However, flow effects may be eliminated by the use of a vacuum whirling arm rig (Sec.2.2) and particle velocities in an airstream may be calculated by the rotating disc method used by Ruff and Ives (29).

Having noted the possible discrepencies that might arise in particle velocity determination, it appears that the effect of velocity on erosion rate has been established. Erosion rate changes with an exponent term of the impact velocity, the relationship being:

$$\text{Erosion} = kV^n f(\theta)$$

where

k is a materials constant

V is the particle velocity

n is the velocity exponent

$f(\theta)$ is a dimensionless function of impact angle

The value of the exponent, n, appears dependent on, inter alia, the degree of ductility of the material being eroded and the impingement angle of the erodent particles. Generally (8,10,17,26,30,31), n values range from between 2,0 and 2,4 for ductile materials, while values from 2.6 (31) to 4.4 (17) for brittle materials has been reported.

Erosion/velocity results (31) for the erosion of nickel are presented in Figure 2.3.

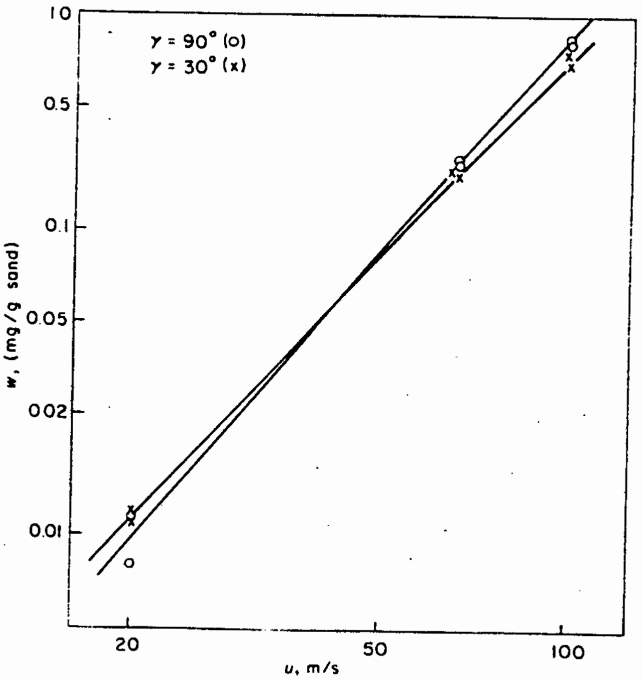

FIG: 2.3 Erosion rate versus particle velocity for erosion of Nickel at various impingement angles (After Soderberg et al (31)).

The reasons for the erosion dependence on the exponent term has been interpreted in terms of both kinetic energy (Energy = $\frac{1}{2}mv^2$) (17) and a local heating effect. It is also suggested (10) that material removal is assisted by heat generated by the strike, therefore a velocity increase results in increased local heating which in turn could manifest itself as enhanced erosion in ductile materials.

Testing at velocities of 15 and 32 ms^{-1}, authors (14) found no velocity effect on erosion but admitted that the lower velocity range of 15 ms^{-1} is approaching the minimum to keep particles entrained in a carrier stream. This conclusion is supported by Raask (24) who found an erosion/velocity cut-off at 15 ms^{-1}.

In contrast, analysis of preliminary results by Smeltzer et al (6), showed the exponent value to be less than 2,0, ranging from 1,64 down to (-)0,3 at which value grade 410 stainless steel in fact gives an improved erosion resistance at higher velocities. Subsequent discussion, however, suggested a exponent range between 1,1 and 1,8. Further, it was found that the exponent values increase with increasing temperatures, as well as being dependent on impingement angle.

2.1.2.2 Impingement angle

The erosion impingement angle may be defined as that angle subtended by the eroded surface and the particle stream. The variation of erosion with changing impact angle is critically dependent on the nature of the material being tested. This is borne out by the comparision of impingement angles on erosion performance of a 'ductile' material, Aluminium and a 'brittle' material, alumina as shown in Figure 2.4 overleaf.

Researchers (6,17,23,25,32,33) have shown that for ductile materials the angle for maximum erosion lies between 20 and 45 degrees while more brittle materials undergo maximum erosion at normal impingement (17,25,33,34,35). These results are independent of particle variations and heat treatments (23), while it is also suggested (15) that curves of the type shown in Figure 2.4 are modified as a function of temperature.

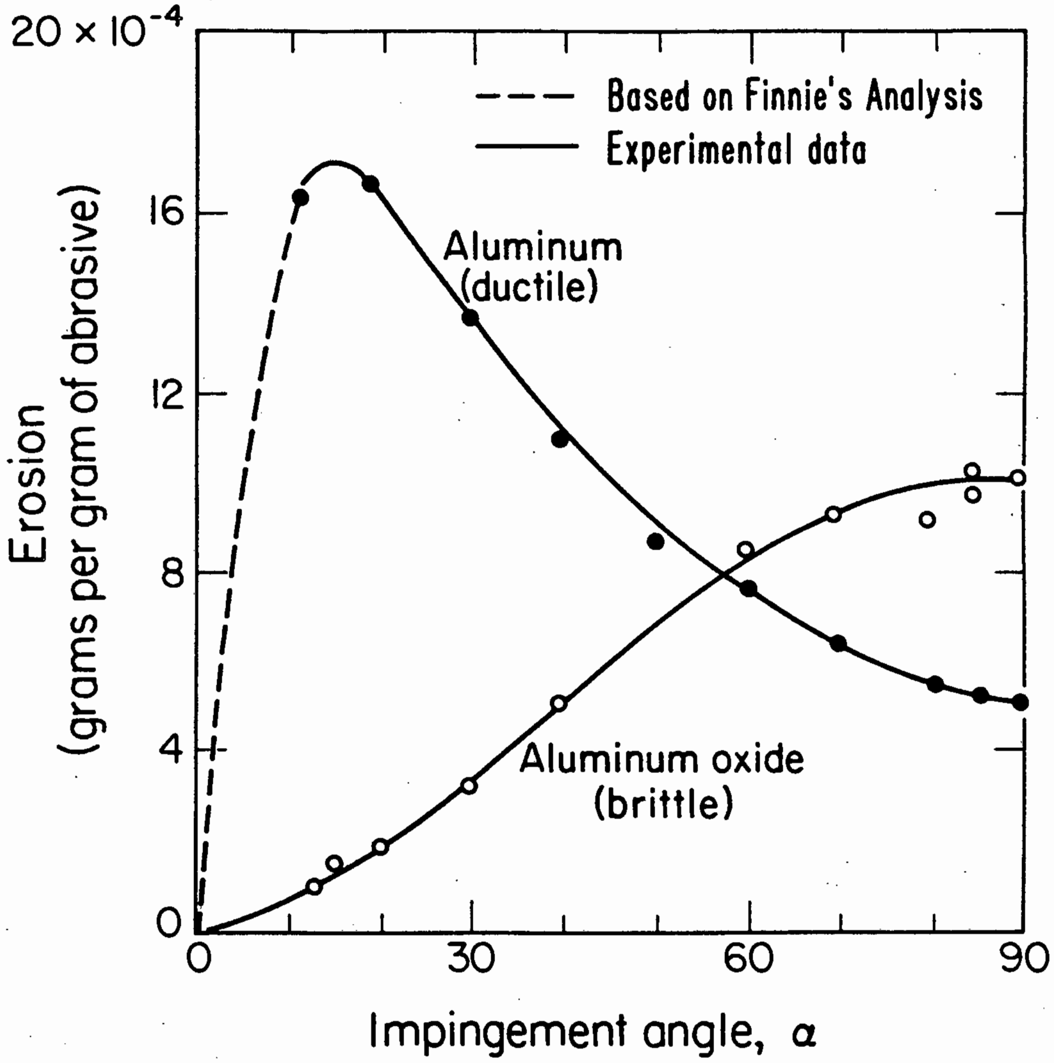

FIG: 2.4 The effect of impingement angle on the erosion performance of ductile and brittle materials (After Zambelli et al (53)).

In contrast the use of a centrifuge tester (31) showed no significant erosion variation with impingement angle after approximately 12 hours of testing (steady state erosion conditions) of various materials groups. While the impingement angle should be noted as an important flow variable, authors (Sec. 2.1.2.3) have noted the influence of particle interactions and aerodynamic effects as factors to possibly alter the pre-supposed impact angle.

These effects are negated by the use of vacuum drop test methods (35), but should be considered when conducting angle testing using sand-blast test methods.

2.1.2.3 Aerodynamic effects

Aerodynamic effects and the interaction of erodent particles have been shown to be important features affecting gas/solid flow. Researches (15) state "the problem is to determine which particles hit at which angle, and which are deflected by the air-stream and miss the surface." The authors thus compiled a work chart of the effect of particle diameter and velocity on the incidence of erosion strikes on an airfoil placed in the gas stream (Figure 2.5).

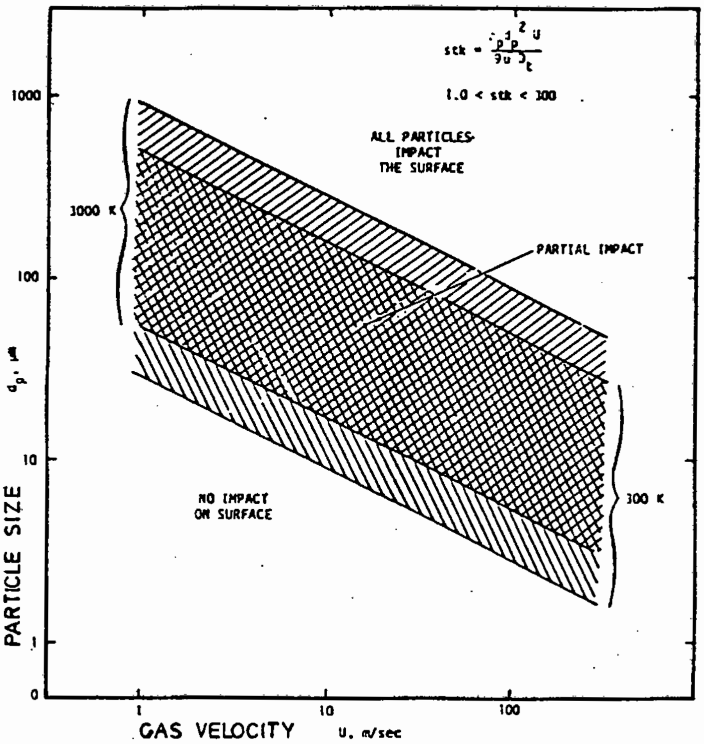

FIG: 2.5 Impaction study work chart to assess the effect on velocity and particle size on strike incidence (After Gat et al (15)).

Aerodynamic effects and particle/particle interactions may therefore influence the flow patterns expected or desired from a test apparatus and are therefore important in a study of this nature.

2.1.2.4 Pressure effects

Although the effect of test pressure on erosion rate has seldom been investigated, a correlation was established (13) in a high temperature erosion/corrosion study. Using test pressures of 101 kPa and 6,9MPa, the authors found a strong trend towards increase erosion/corrosion at increasing operating pressures (Figure 2.6).

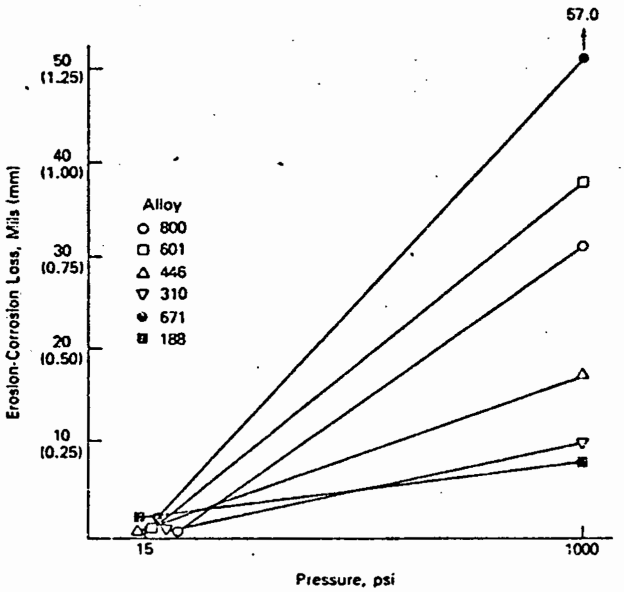

FIG: 2.6 The effect of pressure on erosion/corrosion loss of various metal alloys (After Bhattacharyya et al (13)).

The effect of pressure on pure erosion, however, is unclear and cannot be derived from an erosion-corrosion study as described above. However, this variable should be noted as a possible factor to effect erosion rate in both in service applications and laboratory simulations.

2.1.2.5 Corrosion assisted erosion

Erosion-corrosion studies have produced anomalous results researchers reporting corrosion to play both a minor role (39,40) and to enhance the specimen mass loss (13,41,42,43). In gas-blast erosion studies of coal conversion system materials, Stringer (40) introduced a corrosive element to his tests by the addition of hydrogen sulphide (H_2S) to the propellant gas. He recorded no difference in erosion behaviour of the test pieces, implying that corrosion did not play a significiant part in degradation.

On the other hand, however, authors (13,41,42) have reported that corrosion, in fact, plays a significant part in "a mechanism best described as erosion-hot corrosion synergism". Barkalow and Petit (42) continue "although each aspect of this synergism may be identified, the severity and dependence of each is difficult to predict." While recognising the synergistic effect of erosion and corrosion, researchers (13) found that although increasing the H_2S concentration in the carrier stream generally gave enhanced erosion, certain alloys tested gave inverse results.

It appears that corrosion would assist in the material loss process, and it therefore remains for researchers to decide whether the particular erosion situation under consideration would be susceptible to a corrosive influence or not.

2.1.3 TARGET CONDITION

2.1.3.1 Effect of temperature

Hansen et al (17) state that the effect of target temperature on the erosion rate is not well known and Smeltzer et al (6) report that specimen temperature has "unpredictable, complex effects upon erosion." As can be expected therefore, the influence of temperature on erosion as presented in literature, is shown to have differing effects.

Smeltzer et al (6) go on to indicate a predominant trend towards decreased erosion (up to 50% decrease) with increasing temperature from 200°C to 370°C. This trend is supported by various authors (44,45). Suh (9), also found up to a 50% decrease in erosion rate with temperature up to 370°C of aluminium, stainless steel and titanium alloys. Conversley, an increase in mass loss for nickel at elevated temperature was noted (9). Similarly, titanium alloys were found to show an erosion increase at higher temperature by other researchers (37). These views are further supported by Bhattacharrya et al (13) and Tabakoff, Ramachadran and Hamed (46) (Figure 2.7) overleaf.

The target temperature effect has been analysed in terms of "Type I" and Type II" factors (15). Type I factors are given as those material and erodent variables for which an increase in temperature results in a decrease in erosion resistance, while Type II factors result in an increase in erosion resistance with elevated temperatures.

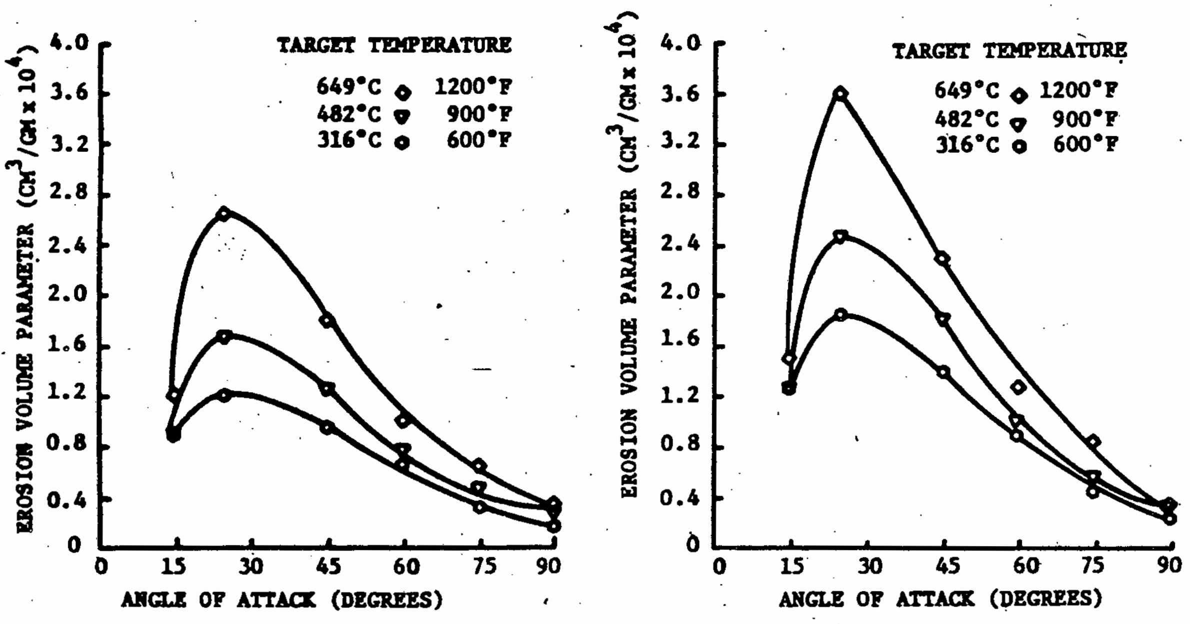

(a) (b)

FIG. 2.7: The effect of target temperature on the erosion of 304 stainless steel at velocities of 244 ms^{-1} (a) and 305 ms^{-1} (b) at different attack angles (After Tabakoff et al (46)).

The situation is further complicated (47) by reports of negligible change in erosion performance of a selection of alloy steels tested up to 950°C. Anomalies such as presented in the erosion behaviour of titanium alloys at elevated temperatures (9,37) illustrate either the discrepencies between test rigs in generating data, or the interpretation of the raw data. In any event, the situation is nebulous and appears largely material dependent, this dependence being further affected by impingement angle (6).

2.1.3.2 Effect of Heat treatment/Microstructure

Finnie et al (30) state that for annealed face centered cubic metals, the erosion rate is inversely proportional to specimen hardness. However, although heat treatments of steels and aluminium alloys can result in threefold increases in bulk hardness, researchers (1,6,10,30,47) have generally found that erosion rates are largely independent of the effects of those heat treatments. Intuitively, this result is somewhat surprising but explanations have been proposed to elucidate this finding. Hutchings (1) maintains that the strain rates generated by the erodent particles on impact are sufficiently high to overshadow or render less important the conventional strengthening mechanisms dependent on dislocation movement at lower strain rates. Foley and Levy (32) continue, stating that most, if not all, heat treatment effects to modify micro-structure are mitigated by adiabatic shear heating of the erosion surface that can cause the recrystallization temperature to be reached. The effects of localized heat generation on particle impact is approached more fully in section 2.1.4.

The effect of particle type on the erosion performace of heat treated grade 1045 steel was investigated (19). It was found that over a range of heat treatments, erosion with crushed glass gave no change in erosion performace, while testing with glass beads as the erodent material resulted in "a profound effect" on the erosion rates, the results being shown in TABLE 2.1. These and similar results (23), should however be interpreted rather as a function of erodent variables (section 2.1.1.) although the influence of heat treatment has been noted.

Heat treatment	Phases present	Hardness (Rockwell A)	Weight loss on erosion for 5 min with crushed glass, g	Weight loss on erosion for 10 min with glass beads, g
Annealed	Ferrite + coarse pearlite	51	0.121	0.0242
Spheroidized	Cementite in ferrite matrix	47	0.119	0.0296
Normalized	Ferrite + fine pearlite	57	0.121	0.0206
Water quenched	Martensite in retained austinite matrix	68	0.117	0.004
Water quenched and tempered at 120° C	Transition carbide in austenite matrix	68	0.115	0.0041
Water quenched and tempered at 315° C	Tempered and untempered martensite	67	0.120	0.0179
Water quenched and tempered at 540° C	Cementite in ferrite matrix	65	0.120	0.0200
Water quenched and tempered at 685° C	Cementite in ferrite matrix	60	0.116	0.0248
Austenitized and austempered at 400° C	Lower bainite	61	0.113	0.0197
Austenitized and austempered at 510° C	Upper bainite	58	0.119	0.0139

TABLE 2.1: Microstructure, hardness, and erosion of 1045 steel subjected to various heat treatments and eroded by equal masses of erodent (After Salik et al (19)).

A direct contradiction appears in other results (23,48). In erosion studies of grade 1050 and 1080 cabron steels, Sargeant et al (23) found the 1050 steel, containing a greater proportion of ferrite, to erode faster than the 1080 steel, this due to the α-phase being leached out in preference to the pearlitic phase. In contrast, Green et al, (48) found that for normalized steels, the erosion rate increased with increasing carbon content.

In other words, pearlite erodes faster than ferrite, the erosive wear being accelerated with increasing pearlite volume fraction. By increasing the carbon content of a steel, the lattice parameter ratio (c/a) is also increased and it has been suggested that this may have an effect on the erosion performace. These authors also maintained that by increasing the hardness by the formation of martensite in plain carbon steels, the erosion rate at 30° impingement angle was accelerated compared to that of a normalized steel. Further, by tempering the same steel at 650°C, a decrease in erosion rate was evident. This trend was also found to a limited extent by other workers (30).

Although all researchers are not in full agreement the affect of thermal hardening of steels on erosion, there is certainly no direct correlation between hardness attained by microstructural changes and erosion resistance of the metal.

2.1.3.3 Effect of prior cold work

Mechanical surface treatments such as cold forming, sandblasting and shot peening have been investigated in terms of effect on erosion by several researchers (4,30,32,44,49). The result of cold working is an increase in surface or bulk hardness together with a corresponding reduction in ductility. As was noted in section 2.1.3.2, hardness need not be the criterion for enhanced erosion resistance, and indeed prior cold work of erosion samples was found to have no effect on erosion performance (19,30,49).

The aforementioned authors reason that, on commencement of erosion, a work-hardened surface layer is formed regardless of the intial surface condition, therefore negating any effect of that condition. Similarly Finnie et al (30) suggest that although a two fold increase in hardness may be attained, the erosion is so severe that workhardening of even annealed material is almost immediate, and therefore the surface hardness is independent of initial conditions. Furthermore, the authors suggest that the flow stress at large strains may be relatively insensitive to the strain imposed by prior work hardening. This is based on metal cutting data which suggests that when metals are deformed at high strain rates to large strains, the stress strain curve at first rises more rapidly than the static curve (due to high strain rates) and then levels off (due to heating) to become almost horizontal.

However, workers have reported results to the contrary. In a investigation on the effect of cold work on 70/30 Brass (4) at impingement angles of 25° and 90°, both instances measured an increase in erosion with a greater degree of cold work. Similarly, in work on grade 304 stainless steel (32), "as-wrought" material gave a 25 percent increase in erosion compared to the annealed metal. In addition, it was found that in erosion tests on 1020 carbon steel, the steel in the hot-rolled condition gave reduced erosive loss compared to the cold rolled specimen. Finally it was shown (44) that a greater amount of cold work on spherodized 1075 steel resulted in increased erosion due to decreased ductility. The dependence on ductility introduces the discussion to the following section.

2.1.3.4 Correlation with mechanical properties

The two previous sections have primarily illustrated the effects of hardness of materials, induced by heat treatments and by cold work, on their erosion performance. Those results point away from hardness and strength as the major contributing factors to the erosion behaviour of ductile materials, and towards consideration of properties such as the ductility and malleability of the metal as the principle properties that determine the ability of a ductile metal to withstand the effects of an erosive particle stream (32). Salik and Buckley (19) continue, stressing "metallurgical structural changes may be more significant to erosion resistance than increases in hardness." The role of plasticity is also emphasized in that it is not necessarily the strength or hardness that influences erosion, but rather the ability of the target to deform and absorbkinetic energy. There is obviously a limit to this theory when either the kinetic energy of the particles is too high or the target materials becomes too weak to resist repeated strikes.

In an experiment to observe any apparent changes in erosion performance of a grade 1020 steel in both the 'ductile' and 'brittle' conditions, it was found (32), at normal impingement, that the brittle specimen gave three times the material loss of the ductile form. As suggested by Figure 2.4, this result could be expected. Increased ductility may serve to improve relative eroson resistance at high impact angles, but conversely, at oblique impingement the more brittle materials perform more favourably.

In an attempt to correlate erosion resistance with mechanical properties, a 'mechanical energy density' term was invoked (50):

Work per unit volume erosion, $w = \frac{1}{2}(\sigma y + \sigma_{uts})\varepsilon f$

Where σy is the yield stress
σ_{uts} is the tensile stress
ε_f is the strain to fracture.

The result is an inverse relationship between erosion and the 'mechanical energy density'. According to this relationship, therefore, an optimum erosion resistant material would have high strength and hardness associated with a high degree of ductility. A material with mechancial properties of this type would quite probably show favourable erosion resistance properties by largely nullifying the impact angle effect.

Nevertheless, researchers have shown that elongation to fracture is a more significant variable than specimen hardness when considering erosion resistant materials, but the subsequent performance of ductile/brittle materials is significantly influenced by impingement angle.

The advantage as erosion resistant materials of metals with high work hardening rates has been demonstrated (71). As a critical strain (ε_f) is necessary for material loss to occur during particle impact, it is clear that a specimen with improved workhardening characteristics would register reduced plastic strain for a given input stress level than would a material with low workhardening character. Furthermore, if further strain is to be imparted into the surface, a strike of higher stress is required, and it is probable that in a uniform erosion environment, the frequency of the higher stress level strikes would become smaller.

2.1.3.5 Oxide layer

The elevated temperatures of a number on erosion environments make materials particularly susceptible to high temperature oxidation. It is therefore important to assess the possible effects of oxide scales on erosion performace of metals in terms of surface adherence and resistance to erosion, and effect on mass loss data obtained from high temperature erosion simulation. Some authors (6) have dismissed the relevance of oxidation, maintaining that it has no effect on specimen mass loss at high temperatures. The relative effect of scale thickness and particle size has been discussed (42). These authors are of the opinion that if the eroding particles are larger than the scale thickness, the rate or mechanism of material removal would not be affected by the oxide scale.

However, more specific investigations into the effect of oxide scale on various substrates have been undertaken revealing a definite affect on erosion resistance. In a study of erosion of oxidation-resistance alloys, Wright (51) showed an "apparent retention of protective oxide scales, even on highly deformed surfaces, by alloys eroding slowest". He continues (52), stating "certain oxide scales may confer erosion/corrosion resistance."

The degree of stability offered by such an oxide layer would therefore depend on the composition of the scale, its thickness and the degree of elastic mismatch between the scale and the substrate material. This view is supported (53) in testing of the erosion performace of nickel oxide scales (20-100 μm) as well as Cr_2O_3 scales on type 310 SS and Al_2O_3 scales formed on an experimental aluminium alloy. These authors noted that erosion behaviour of the scales were a function of both composition and microstructure.

These conclusions suggest that oxide layers may play a role in erosion mass loss, especially in controlled laboratory simulations where specimen mass losses should ideally reflect bulk material removal only.

2.1.4 TARGET RESPONSE

2.1.4.1 Incubation period

An incubation period, or a period of limited erosion before a steady state of erosion is reached, has been reported by various authors (4,54,55,56). This period, if a matter of weeks or months, could have serious implications to in-situ components threatened by an erosive environment. However, possibly more important is the effect this variable would have for laboratory testing. Short duration tests would be affected in that a true reflection of the erosion behaviour of the material under consideration could not be gauged accurately. This problem would be more pertinent if the incubation time were material dependent.

It would appear that the duration of the incubation periods is dependent on the test method employed. Incubation times of 20 seconds for grade 1080 steel (23), and up to "hundreds of hours" with a venturi test apparatus (57) have beeen reported. Reasons for this time dependence include the formation of a work-hardened layer before material is lost, and the stabilization between material loss and particle adherence before a steady state is reached (28,31). However, severe erosion conditions would most likely have little or no incubation.

2.1.4.2 Local heating on erosion

Workers agree that there is a temperature rise associated with particle impacts on the erosion surface. However, there is uncertainty as to whether there is sufficient energy to cause localised melting or whether the heat produced is conducted away at temperatures less than T_m. Local heating on erosion is important both as a possible primary or secondary erosion mechanism as well as affecting the validity of target temperature as an important test parameter. It is proposed (11) that temperatures approaching the melting point of steel are generated locally by impact of erodent particles, therefore indicating that target temperatures are unimportant (other authors (1,2,26,50,54,58,59) have suggested temperature increases ranging from "a few hundred degrees centigrade" (1,2) to approximately 700°C (58), but have however discounted the possibility of surface melting. Finnie re-asserts that even at test temperatures of the order of 400°C, the local heating at the impact site is in excess of that of the bulk specimen (7). But, as a result, the (detached) chip temperatures may exceed the melting point of the material but as the strain rates on impact are extremely high and the duration of cutting extremely short, there would perhaps be no time for melting to occur. Figures 2.8, 2.9, and 2.10 show Hutchings' estimate of the probable energy balance associated with various erodent shapes at differing impingement angles (1).

Figures 2.8 to 2.10 show that the greatest heat generation (aproximately 72% total kinetic energy) occurs at normal impingement with spherical particles while oblique spherical particle impacts result in considerably less heat energy generation (approximately 14% of initial kinetic energy). As a result, a relatively large percentage of generated energy is realized as heat, especially in the normal impingement condition, and indeed researchers have produced experimental evidence to verify theories of local melting during erosion.

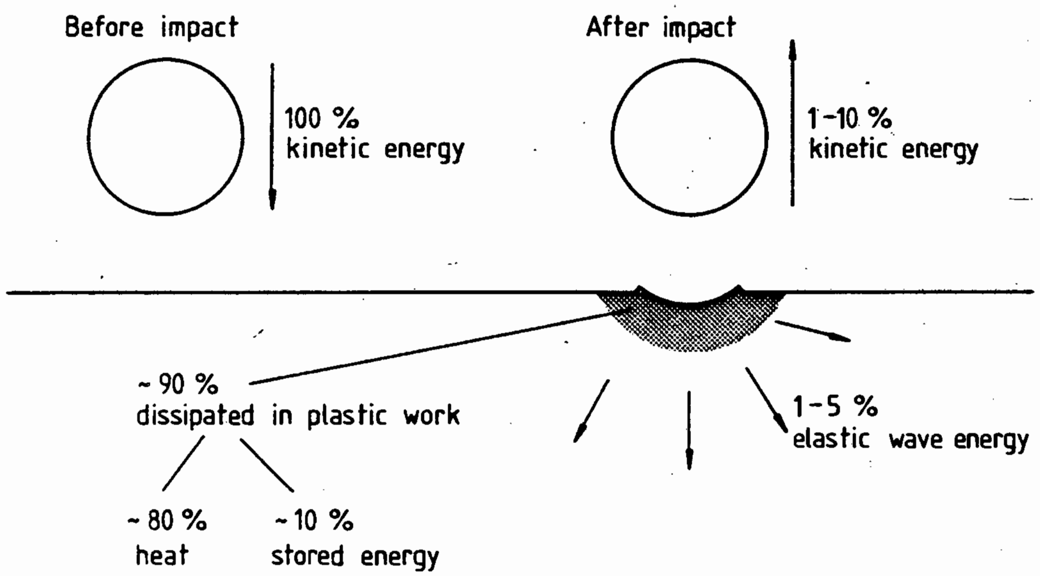

FIG: 2.8 The energy balance in the normal impact of spherical erosive particles on the target surface (After Hutchings (1)).

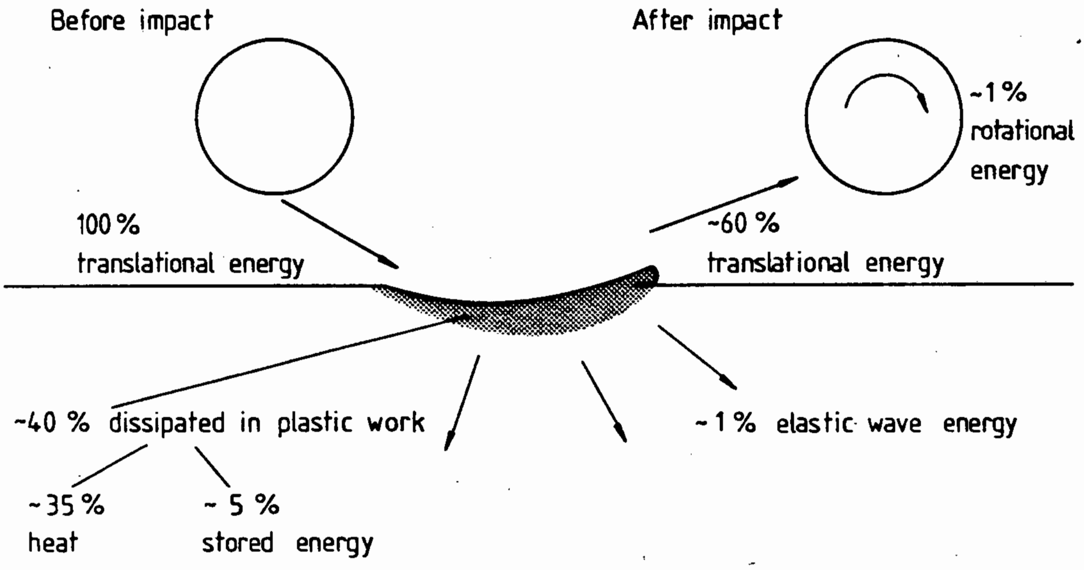

FIG: 2.9 The energy balance in ploughing impacts at 30° impact angles for spherical particles (After Hutchings (1)).

Reports of a direct correlation between melting temperature, T_m and the erosion energy input have been made (59). Further authors (3,6,45,56,60) have related direct evidence of melting in both metals and ceramics (45).

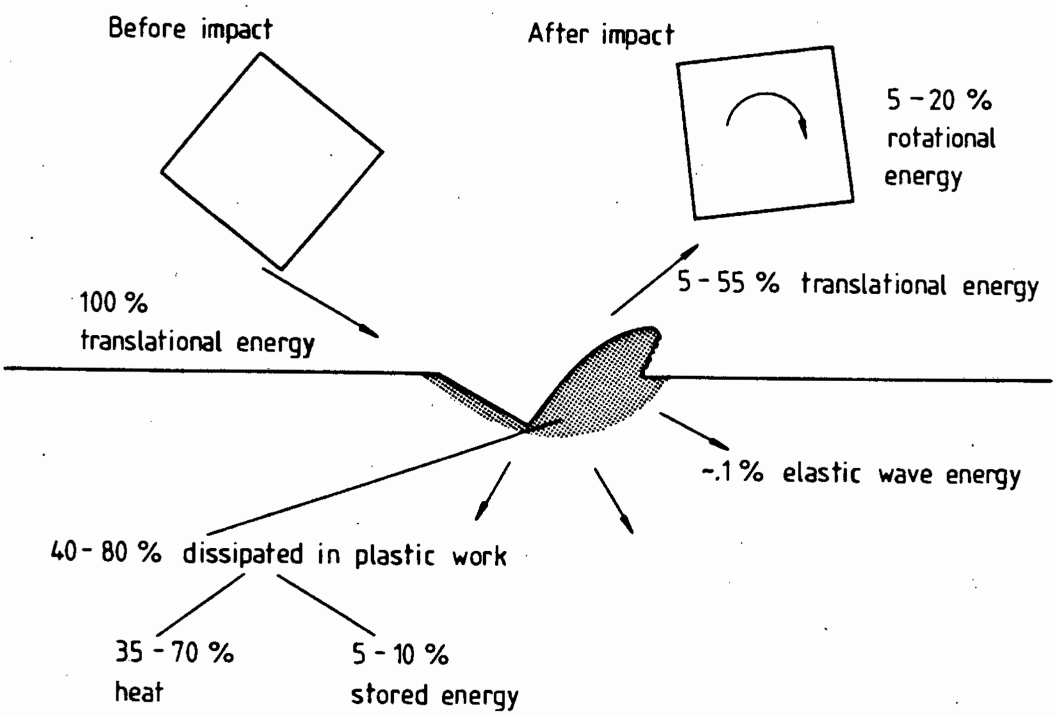

FIG: 2.10 The energy balance in cutting impacts at 30° impact angles for angular particles (After Hutchings (1)).

A metal detachment mechanism due to intense local heating and possible melting on localized shear planes in very strong alloys has been suggested (10), while less conclusive evidence was presented (15) in the form of molten lips on "a few" craters on a tungsten target. The authors, however, conceded the possibility that this layer was molten oxide rather than pure tungsten. In support of the observed

evidence of melting, a quantitative model to approximate the heat generation rate in an assumed near steady state impact system was proposed.
Equating the expression :Heat generation rate $=\sigma_n \mu v$

where σ_n is the normal stress on the surface
μ is the coefficient of friction
v is the tangential velocity

with the heat flux, or rate of heat dissipation, the authors calculated that in brass surface melting would occur.
While all authors are not in agreement as to the feasibility of localized melting, or indeed if melting is the result of a single or multiple strikes (6), it is accepted that a temperature rise is realized. This conclusion has importance for specimen heat treatments or mechanical surface condition, in that recrystallization or even annealing temperatures may be generated to offset prior treatments, rendering them unimportant. The desirability of recrystallization due to frictional heating to improve erosion restistance has been explained (71).

2.1.4.3 Embedded particles

Erodent particles such as quartz, glass fragments, sand and alumina have been found to become embedded on erosion surfaces during erosion testing (23,25,28,54,56,58). In an erosion study of tungsten, evidence of embedded quartz particles was recorded at elevated (203°C) temperatures but not in the room temperature surface, suggesting a target temperature effect (Section 2.1.3.1.).

Authors (31,33) have further observed an initial negative mass loss on commencement of erosion due to the adherence of erodent particles before a steady state erosion condition was reached. This factor should be noted when considering data generated at short test times.

2.1.4.4 Workhardening of surface layers

Microstructural evidence of a sub-surface work hardened layer could be interpreted both mechanistically and in terms of estimated impact-induced heating. Investigation (61) revealed no distinguishable strain hardening effects on the erosion of aluminium, suggesting therefore possible localized adiabatic heating into the recrystallization temperature range. On the other hand, however, extensive work hardening of the indented regions of grade 1075 steel and 70/30 brass respectively has been observed (4,44) causing high levels of strain.
It would thus appear that the formation of a work hardened layer is dependent on various factors including materials tested as well as test apparatus used.

2.1.4.5 Microstructural changes

It has been shown in previous sections that local heating by impacting particles and the formation of a workhardened layer during erosion have been observed by various authors. However, suggested local heating temperatures rises into the recrystallization range conflict with the proposal of a workhardened layer. This dilema as to the magnitude of the local heating is of great significance when considering erosion mechanisms. Local heating induced microstructural changes could support a temperature assisted (or even a melting) material removal mechanism, while evidence of a strain-induced workhardened layer without evidence of a heating effect would discount any temperature related mechanism.

Experimental evidence of microstructural changes during erosion is available (54,56). In SEM and transmission electron microscope (TEM) analyses of erosion debris of copper and α-Iron, these authors showed evidence of detached flakes to be either heavily worked or recrystallized. This recrystallization probably reflects a combination of a large strain and localized heating from impact. This analysis, lending support to both of the above mentioned schools of thought, stresses both the complexity of the situation and the need for careful consideration of surface changes as well as erosion debris.

2.2 EROSION TEST RIGS

Researchers have developed certain test rig 'concepts' with which erosion may be simulated, and the variables isolated and quantified. Four principal types of laboratory test equipment have been listed (31):

(i) free particle fall in vacuum,
(ii) sandblasting,
(iii) whirling arm, and
(iv) centrifugal particle accelerator.

In the investigation of a particular erosion condition it would be beneficial and more representative to select a test apparatus concept most compatible with the problem under review. The advantages and limitations of the four quoted test methods are briefly discussed in the following sections.

2.2.1 GRAVITY FEED VACUUM RIG

Particle free fall under vacuum was used in tests on various materials including glasses, metals and cements (35). Erodent particles are fed into a vertical, evacuated tube of known height and allowed to fall, under gravity, onto the positioned target. The advantage of this method is, as with all vacuum rigs, that the absence of aerodynamic effects ensures a 'true' impingement angle is realized. Furthermore, thesize and shape of the erodent used has no effect on the velocity of impact, this parameter being dependent strictly on drop height. These factors result in efficient control over particle velocities, concentrations and impingement angles, thereby establishing good reproducability in the method. The major limitation of the equipment is the relatively low particle velocities (± 5 ms^{-1}) (31) which has limited application.

2.2.2 SANDBLAST METHOD

The sandblast or gasblast method, by nature the most closely allied to in service erosive conditions, and indeed employed as a useful tool in industry (sandblasting operations), is probably the most frequently used technique.

In this technique the erodent particles are introduced into the gas, [screwfeed (62), venturi (21)] and accelerated by the gas towards the target. An accelerating tube is generally incorporated to allow stabilization of particle velocities and to ensure homogeneity of the particle concentration. The stream is finally directed onto the specimen by positioning the tube nozzle at the predetermined impingement angle a set distance from the surface. The drawbacks of this system are primarily due to the aerodynamic effects of the particle/gas stream which are both difficult to assess and to control. Discussion in section 2.1. has examined the flow variables in a gas/particle system, while authors (1,31) have further stressed the differences in particle velocities compared to that of the carrier gas. Depending on particle flow rate generated, the effect of particle-particle interactions in the flow system will influence erosion to a greater or lesser degree (section 2.1.2.3).

The impingement angle of erodent particles will also be affected by the variation in flow pattern over the specimen surface (38) as shown schematically in Figure 2.11.

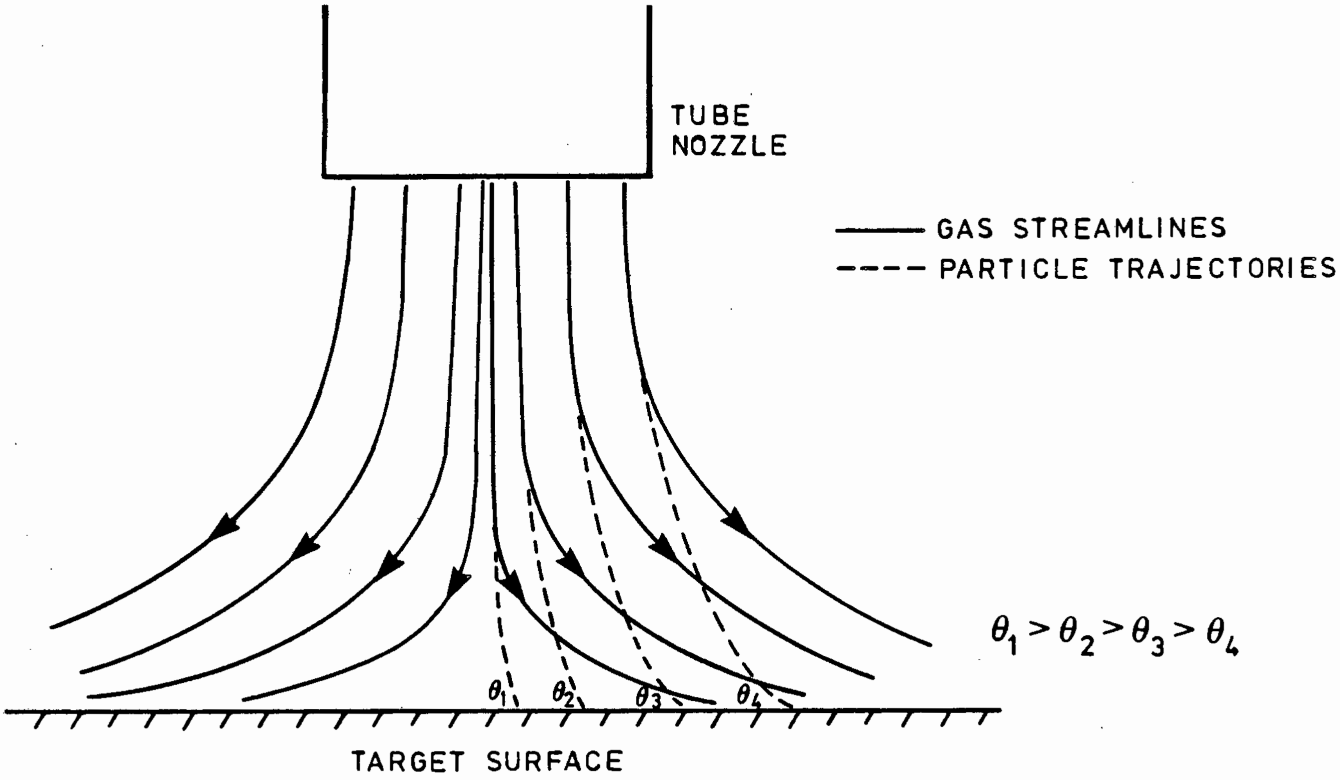

FIG: 2.11 Schematic effect of particle trajectories due to changing gas streamlines during 'normal' impact on target surface (After Laitone (38)).

This effect is naturally dependant on both particle size and gas velocity, and may be similarly interpreted for oblique impact angles. The result, however, is a variation in both impact angle and velocity of the impacting particles which may effect the validity of simulated erosion results. Nothwithstanding the above mentioned drawbacks and control difficulties, the sandblast method most directly reproduces most erosion conditions, especially those experienced in ashlock valves.

2.2.3 WHIRLING ARM TESTERS

With whirling arm test rigs, the target specimens are fixed onto a rotating arm, their velocity accurately calculated by the rotational velocity of the arm. The particles are allowed to fall into the path of the spinning specimens under gravity. The operation of the rig may be modified by evacuating the test chamber (8) to negate aerodynamic effects and gas streamline variations as mentioned in section 2.2.2 above. An advantage of this system is that multiple specimen tests may be conducted simultaneously, thereby reducing the possibility of error due to environmental change.

2.2.4 CENTRIFUGAL PARTICLE ACCELERATOR

A centrifugally accelerated particle erosion method (erofuge) was used in the erosion classification of various materials (31). The erofuge differs principally from the whirling arm rig in that the erodent particles are accelerated by a rotating plate onto essentially stationary target material. A vibratory feed introduces the particles onto the spinning plate, which is chanelled to direct the erodent to the circumference, and then onto the specimens placed circumferentially. As with the whirling arm rig, the impingement velocity is determined by the angular velocity of particle outlets on the plate circumference.Furthermore, the advantages are similar to those of the whirling arm rig and the ease of control of the erosion parameters renders the apparatus suitable for fundamental erosion studies, although erodent concentration control could be difficult.

2.3 EROSION MECHANISMS

In papers presented on erosion, authors generally attempt to quantify the observed surface damage in terms of a material removal mechanism. From examination of the worn surfaces, by SEM and optical microscopy, it is attempted to glean information as to which parameters inhibit the erosive process, and should therefore be selected in future materials design. However, the situation is unfortunately not so clear and certain dissension exists amongst researchers with regard to mechanism nomenclature and observed surface damage.

The relevance of detailed microstructural consideration of the eroded surface is explained by Hutchings :"The removal of metal from a surface by erosive wear results from the impact of the abrasive grit particles with the surface. An understanding of the forces and material deformation induced by the impact is therefore an essential component of any theory of the mechanisms of erosion" (1).

The suggested erosion mechanisms reviewed in literature are found to be a function of both impact angle (oblique vs. normal) and material type (ductile vs. brittle). This interdependence has been illustrated in Figure 2.4. This section has therefore been approached in terms of impingement angle and the predominantly observed material removal mechanisms are outlined. Mention is made of proposed thermal mechanisms as well as wear fragment analysis as a mechanistic tool.

2.3.1 OBLIQUE IMPACT

The mechanisms for oblique erosion are thought to be relatively well understood, the erosion modes encompassing terms such as forging, extrusion, ploughing, cutting, forging-extrusion, flaking and micro-machnining. Low impact angle mechanistic studies have been undertaken using single macroscopic particles, and with the aid of high speed photography, three predominant erosion modes were identified (26). While the validity of single impacts on mechanistic studies has been questioned (31), the 'ploughing' and Type I and Type II cutting mechanisms proposed by Hutchings have been substantiated by other authors. Hutchings' approach is illustrated in Figure 2.12.

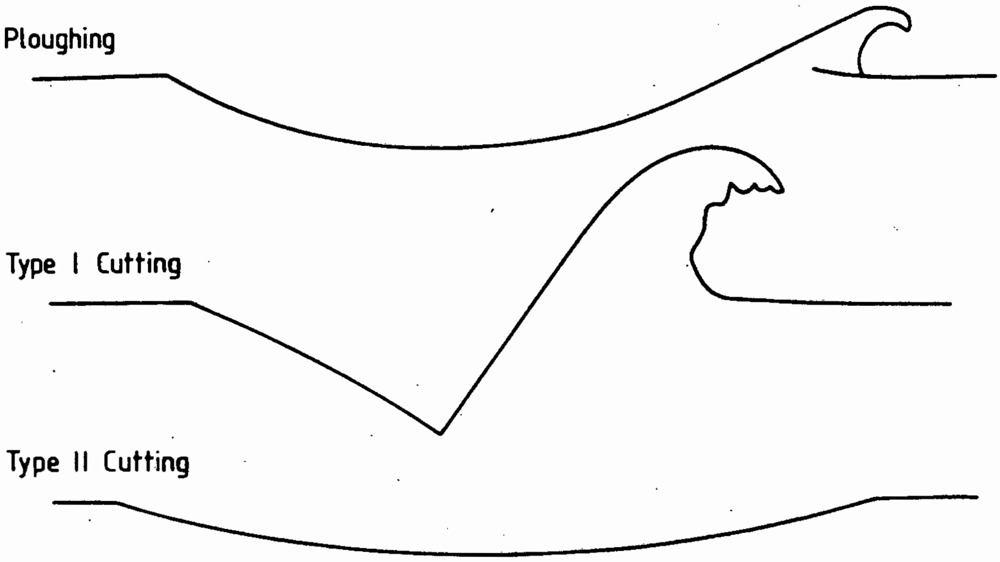

FIG: 2.12 Three types of deformation which can be identified in particle impact at oblique angles. Impact direction is from left to right (After Hutchings (1)).

'Ploughing' is caused by the impact of a spherical particle at approximately 30° impingement and can result in material removal in a single strike. Type I and Type II cutting are a result of impingement of angular particles in opposite rotation. Type I occurs when the particle is rotating anti-clockwise and, on striking the surface creates a lip of material which is then highly susceptible to removal by subsequent impacts. This theory of detachment of raised lips as a primary material removal mechanism is supported by various authors (2,3,8,48).

Type II cutting is the result of clockwise rotation of the particle, the removed chip being very similar to those formed during machining processes, hence the reference 'micromachining'. Again, researchers have proposed similar chip formation mechanisms (9,48).

In a recent study of erosion mechanism of austenitic stainless steels at various impingement angles,two basic mechanisms of cutting erosion and deformation erosion were distinguished (20). The authors have quantified the frequency of occurance of various crater types, the results presented in Figure 2.13 overleaf. Experiments using a lathe to simulate a change from cutting to ploughing indicated the effect of particle orientation (shape) on erosion mechanisms (21). While low angle erosion discusions generally focus on ductile materials due to their relatively high erosion rates compared to brittle materials at oblique angles, Bitter maintains that cutting prevails at small impact angles and that 'brittleness' has little influence on cutting wear (63).

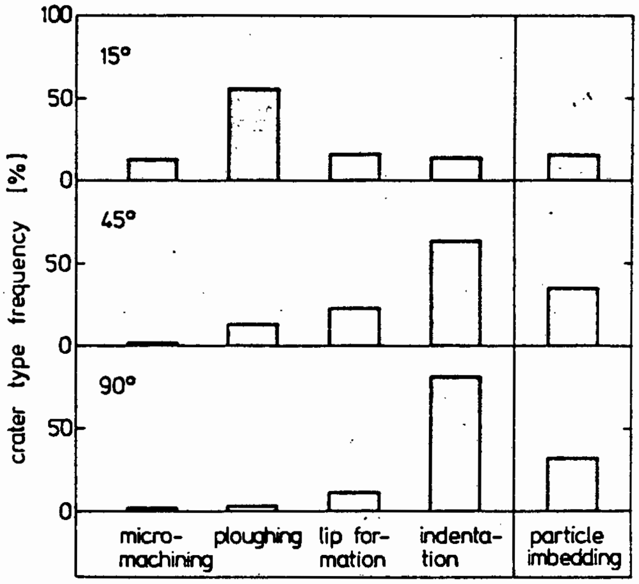

FIG: 2.13 Crater type and particle embedding frequency at 15, 45 and 90 degree angle of impingement and 66 ms^{-1} particle velocity (After Soderberg et al (20)).

A platelet mechanism for the erosion of ductile materials has also been proposed (54,61,62). Bellman and Levy suggest three distinct crater types are formed on impact, regardless of angle of impact (62). They are termed indentation, ploughing and shearing, and, although all three are ever-present on erosion, the relative amount of each varies with the impingement angle. As the angle moves from oblique to normal, the incidence of crater-type increases from shearing, through ploughing to indentation crater. Platelets of material are formed about the rims of the craters, the formation enhanced by the impact generated heating effect which results in a heated surface zone (softer). Simultaneously, the material beneath this heated volume becomes work-hardened (32,64). The work-hardened zone prevents deep particle indentation and consequently the soft surface area is further plastically deformed (forging -extrusion). Platelets of material are removed from this highly deformed surface. The incorporation of a secondary mechanism for the removal of raised lips on erosion surfaces by radially scattered particle fragments has also been supported (1,2,8,11).

As has been shown, the mechanisms invoked for the removal of (ductile) material at low impact angles, with the exception of the platelet option, are generally similar in concept. Hutchings concludes that for low angle impingement "there is no need to invoke any mechanism other than that of plastic indentation followed by removal, by ductile fracture or shear deformation, of part of the displaced metal" (1).

2.3.2 NORMAL IMPACT

Erosion mechanisms at normal or near-normal impingement appear to be less well understood than oblique angle mechanisms (1,63). The concepts of cutting and ploughing cannot be applied under normal impact conditions where, after single impact, original surface markings may often be noted at the bottom of the impact crater. The question, therefore is posed (7): "So how does material get removed by many particles?"

For ductile metals, material removal processes such as local adiabatic shear (Christian and Shewman (1979) [cited in 1],48), back extrusion (Tabor [cited in 1],3,48) and delamination due to workhardening and subsequent fracture from elastic mismatch in the affected regions (32,64) have been proposed. For brittle materials, more susceptible to material loss at normal impact than ductile materials, a 'delamination' or 'subsurface cracking' mechanism has been supported (15,53,54). On impact, radial cracks extend from the plastic zone associated with the strike into the elastic region of the target as shown in Figure 2.14. The force on impaction results in lateral crack formation and consquently finally material being removed on intersection of the two cracking modes.

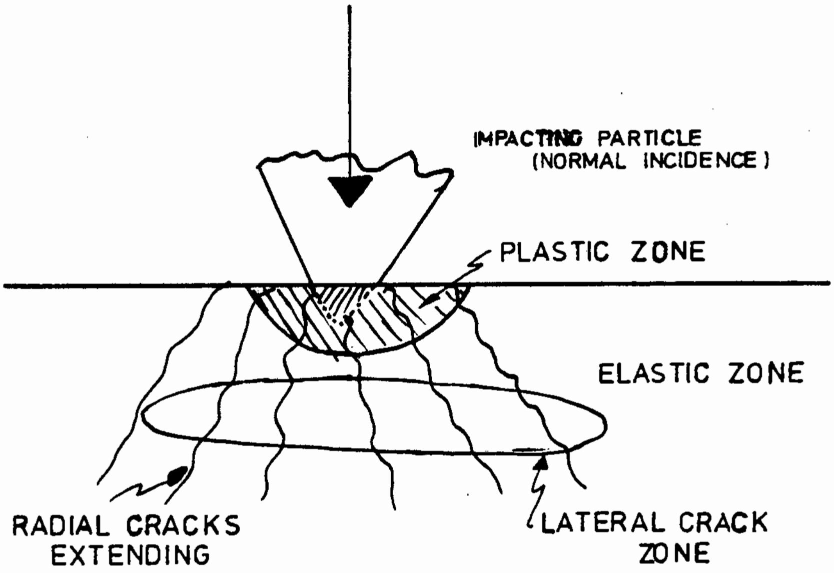

FIG: 2.14 Cracking modes associated with normal particle impact on a brittle target material.

Fatique has been considered as a mechanism in metals (10,11) and in erosion of rubber materials (31). However, it has been suggested that subsurface crack propogation can be confused with high cycle fatique, but that this is inappropriate (54).

2.3.3 THERMAL MECHANISMS

The effects of target temperature and local heating due to particle impacts have been ignored in above sections on erosion mechanisms. However, as has been noted in sections 2.1.3.1 and 2.1.4.1, the temperature effect, especially local heating on impact, is generally regarded as a relevant parameter. As such, "thermal models are of major importance" (47) and constitute a significant role in mechanistic studies, and indeed workers (Ascarelli [cited in 1],6,10,15) have considered melting as a mechanism for material removal. From energy balance calculations, presented in Figure 2.8 in section 2.1.4.1, it is apparent that sufficient energy is dissipated as heat to cause melting or near melting temperatures to be realized. A brittle material at room temperature may therefore become more ductile at elevated temperatures which, in turn, would affect the erosion mechanism.

2.3.4 WEAR FRAGMENT ANALYSIS

A technique which to date has only been applied by relatively few researchers is that of wear fragment analysis. The practical problems associated with the collection of representative 'debris' and the subsequent preparation of such samples for examination are obvious. However, SEM and TEM evaluations of erosion debris of α-iron and copper have been presented (54). Further wear debris was collected and analysed, which illustrated the thermal aspects of surface deformation to be important (47). This finding was supported in a comprehensive study of wear fragments in which the authors (58) identified three representative debris 'classes', namely 'tufts', 'flakes' and 'chips'. It was found that 'tufts' related to high temperature (± 600°C) events and by further analysis of the shapes and microstructures of fragments much mechanistic information could be assimilated.

2.4 EROSION RESISTANT MATERIALS

Researchers, in fundamental erosion studies, have been generally found to use common (engineering) materials such as copper, carbon steels, glass, and alumimum alloys during testing. Erosion studies on single crystals have also been undertaken (54). Having isolated the erosion variables and estimated the requirements for an 'erosion-resistant' material, researchers have initiated test programmes on more 'exotic' materials. For severe service conditions such as experienced in gasification and turbine environments, doubts have been expressed (17) as to whether even the best metals are good enough for effective erosion-resistance in these applications. As a result, ceramics and cements have been suggested as replacement materials in high erosion environments (16,17,55,65). The major drawback to date with ceramic materials are their suspect impact resistant properties.

As regards metals, much interest has been generated by carbide systems (66,67) and the effect of carbide grain sizes, intergranullar spacings and binder content and composition. Coatings have also been proposed as an erosion prevention mechanism and consequently much work is necessary to clarify the worth of these suggestions.

CHAPTER THREE

TEST RIG DESIGN

3.1 INTRODUCTION AND GENERAL PRINCIPLES

In order to reproduce, as faithfully as possible, the flow conditions across the value in question, it was decided to design the test rig on the gas-blast or sandblaster-type principle.

While it was endeavoured to reproduce the in situ situation in the laboratory, certain unknowns in the industrial application made it difficult to accurately assess the precise response of the rig design as a substitute to the service conditions. These factors included ash flow characteristics, the mass flow of ash through the eroding valve, and the velocities of the erodent particles passing through the valve. With reference to the lockhopper valve operation as detailed in Chapter I, the ash flow condition at the top valve on emptying the ash lock is unclear. The regions surrounding a leak area could either be effectively blocked with ash and clinker or alternatively be free of clogging. This information could influence the above mentioned unknowns by limiting the acceleration path, as well as the number of transient ash particles, thereby possibly influencing resultant velocities attained by them.

While acknowledging these inconsistencies, by carefully reproducing the service conditions, it would be most likely to approximate the situation.

3.2 DESIGN DATA

Noting the affect of various physical parameters on the erosion performace of materials, the design data may be interpreted as those parameters that may not be altered as 'constants' of the gasification process.

3.2.1 PRESSURE

The working pressure in the gasification environment is approximately 2,5 MPa (368 psi). This pressure is thus reproduced in the laboratory test facility.

3.2.2 TEMPERATURE

Although temperatures up to 1200°C are reached in the burning section of the continuous gasification process, thermocouples showed the top and bottom ashlock valves to experience temperatures of between 350°C and 400°C.

Apart from the noted effects of temperature on the materials response to erosion, the effects of increased temperature on the flow characteristics of the ash across the valve, and more particularly on the air velocity, need to be considered. It will be noted in section 3.3.4 that the inlet and outlet geometry of the valve seat/cone interface resembles that of a converging-diverging nozzle. Theory suggests that, on satisfying a particular pressure ratio (Appendix A), the flow through a valve or nozzle will become 'choked' ie. attain a flow velocity of Mach I , and this will be the highest velocity attained, at the throat, irrespective of pressure, at a particular temperature.

At a temperature of 400°C (673K), the calculated theoretical velocity of gas across the 'choked' test nozzle is therefore 520 ms^{-1} as opposed to approximately 340 ms^{-1} at room temperature (Appendix A).

A variety of flow situations are possible, varying from normal shock waves in the 'nozzle' to perfectly expanded flow (no shock waves in the nozzle or outside of it, $M = 2,77$ approximately) to oblique shock waves at the exit, finally expansion waves (Prandtl-Meyer flow) at exit. As this theoretical approach neglects any possible effects of entrained erodent particles in the stream which need not necessarily behave as the carrier gas (38), the practical situation is further compounded.

It was therefore necessary, in an attempt to reproduce the ashlock valve environment, to design for 400°C in the test rig; the various options and theoretical calculations for heating the erodent are dealt with in detail in section 3.3.6.

3.2.3 GEOMETRY

Changes in the valve geometry could seriously affect the performance of the valve by changing the flow patterns across it, and consequently this parameter should, at least initially, be kept constant. The option should remain however to alter valve geometry to assess possible improvement in erosion.

3.2.4 ERODENT

After the burning process, the ash and clinker residue varies considerably in size and shape. Samples of this ash fraction were obtained and the particles and conglomerates ranged in size from 30 mm down to submicron fines (Figure 3.1).

FIG: 3.1 Size and shape variations in an ash and clinker sample taken from the gasifier after the burning process.

As literature emphasizes the importance of erodent nature on erosion, it was considered essential, in a study of this nature, to use samples of the actual ash from the particular gasification process for the simulated erosion tests. From examination of the erosion tube size in the failed seats of the full-size valves, it was apparent that the erosion, at least initially. was the result of 'smaller' particle impact rather than the larger clinker.

Based on this observation, it was decided to use as the erodent, a sample sieved using a 600 µm sieve. Sufficient ash (seventeen x 214 kg drums) was subsequently sieved from a single ashlock load at a gasification plant and despatched for testing.

3.3 DEVELOPEMENT

The apparatus envisaged initially, involved the introduction of the erodent particles into a compressed air-stream by means of a venturi nozzle (Appendix B). The mass flow of ash into the air-stream would be controlled by a adjustable orifice plate or valve, allowing precise control of the ash flow rate across the specimen. A 'mixing' or 'accelerating' tube would connect the venturi and the test cell and finally, the ash would be removed from the air-stream down-stream of the test cell. Furthermore, provision had to be made for heating the ash to the working temperature (400°C), as well as for simple loading of ash into the ash hopper.

The basic design, therefore, can be simplified into seven sections, namely :

i) the air/pressure source,
ii) the particle hopper or reservoir,
iii) an erodent feed mechanism,
iv) test cell,
v) ash collection,
vi) heating system,
and vii) the ash loading system.

These components are presented schematically in Figure 3.2

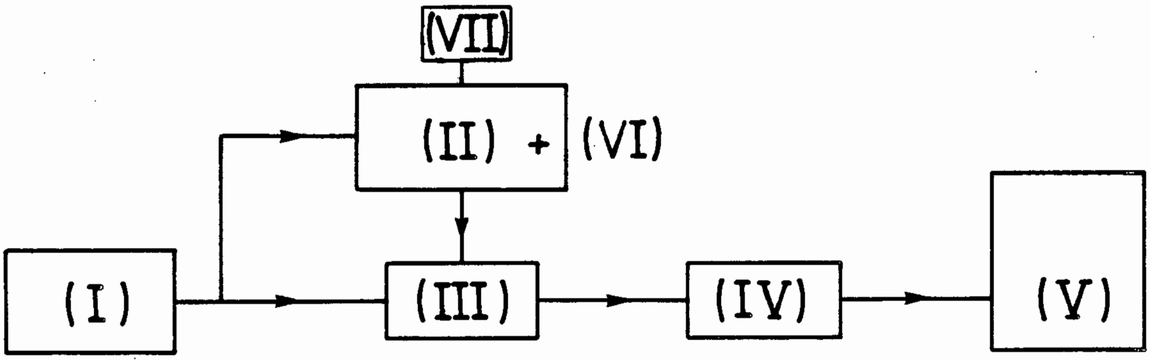

FIG: 3.2 Conceptual layout of envisaged test apparatus. Components labelled as detailed in (i) to (vii) above.

The system, as outlined above, was used as the design criterion; the components were specified and a prototype was constructed. It should be noted at this stage that the design proposed was a 'one-off' experimental rig. As such, there were certain 'unknowns' associated with the rig design. These included the duration of a particular test, be it seconds or minutes (hence the capacity of the ash hopper); the number of tests required to produce measurable specimen mass loss; the effectiveness of the theoretically based venturi as an ash feed; the possibility of severe erosion occuring in the corner lines and the test cell noting the nature of the particles being transported, and the workability of any proposed ash loading system and dust removal system.

The various componenets, as listed i) to vii) above, are presented in separate sections below, the proposed alternatives and the final prototype construction being detailed.

3.3.1 COMPRESSOR/AIR SOURCE

The working pressure has been stipulated at 2,5 MPa, this therefore the minimum pressure requirement.

The calculation of flow rate is based on the two-phase flow theory prediction of a necessary velocity of approximately 10 to 12 ms^{-1}, through a 18,9 mm bore tube, to maintain a homogoneous entrained ash flow (14).

The calculated free air flow rate from the compressor, based on the above mentioned values, is 2,8 ls^{-1}.

The unit decided on was an Atlas-Copco LT-730 compressor (Figure 3.3) with incorporated pressure switch and air receiver.

FIG. 3.3: 2.5 MPa working pressure air source with attached 350 l receiver.

The 350 l capacity receiver reduced time delays on pressurizing the hopper as the vessel could be maintained at the working pressure by control of the air pressure switch.

The relevant principal data for the unit is :

Maximum working pressure	:	3,0 MPa
F.A.D.*	:	5,27 ls^{-1}

* Free air delivery at normal effective working pressure.

3.3.2 ASH HOPPER

The problem of not knowing the duration of an erosion test or the time needed to cause a significant erosion mass loss of the specimen, caused concern as to the design capacity of the hopper unit. Due to the relatively high working pressure experienced in the ash hopper, the unit had to be constructed as a pressure vessel, therefore it was desired that the final dimensions be as small as possible. On the other hand, however, too limited an ash capacity would result in time wastage on recharging and re-pressurizing the vessel between interrupted tests.

An estimate as to the suspected ash flow was made in order to ascertain an approximate flow rate. Assuming an air flow rate of 2,8 ls^{-1} (section 3.3.1), and tentatively suggesting a 5 percent by volume ash content in the air stream, an ash flow rate of 0,14 ls^{-1} was calculated.

Using this figure as a guideline, a hopper volume of 100 l was decided on. This volume gave a theoretical test time of approximately twelve minutes with a full hopper.

The hopper, as constructed, is shown in Figure 3.4.
As is detailed in sections 3.36 and 3.37, the ash hopper was finally constructed to incorporate both heating facilities as well as ash loading facilities. The design, therefore, had to accomodate both the test pressure (2,5 MPa) and test temperature (400°C).

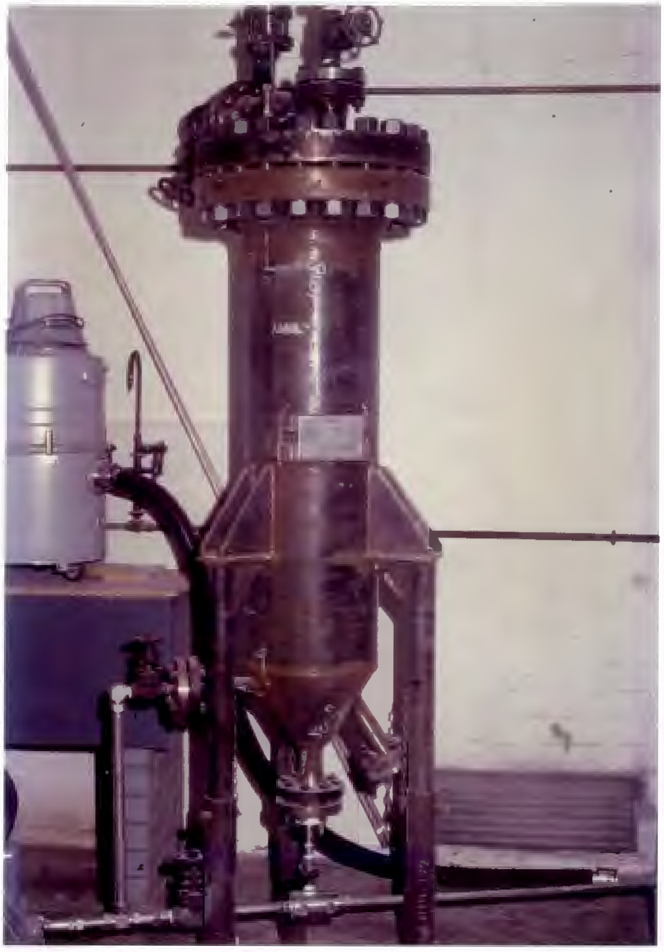

FIG : 3.4 Experimental ash hopper (without insulation).

The dimensions of the hopper are labelled in Figure 3.5 overleaf.

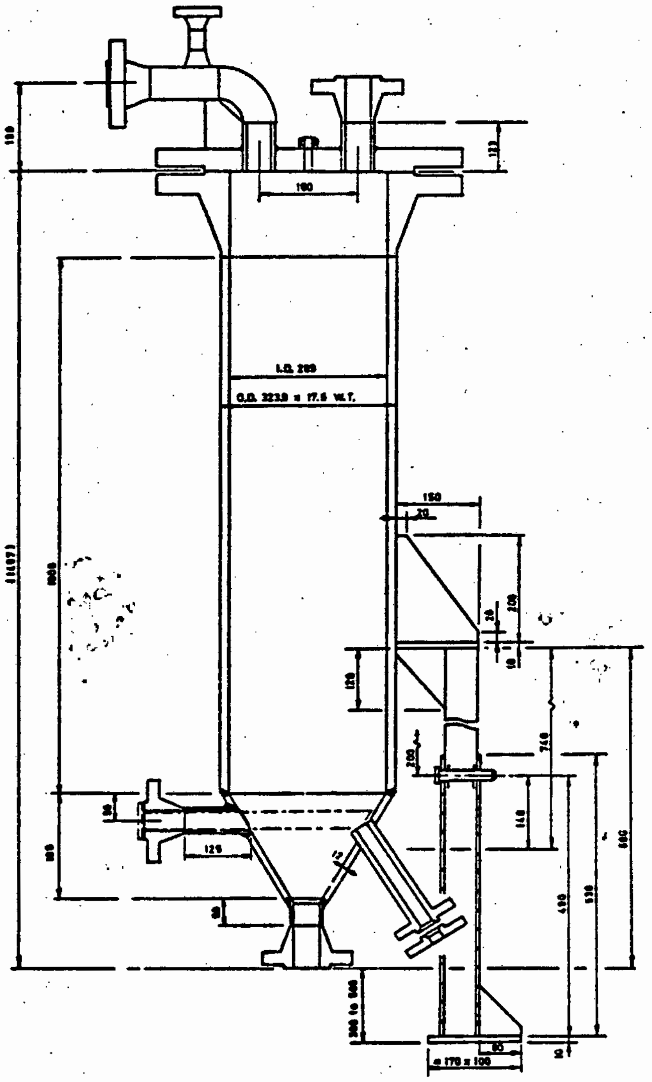

FIG: 3.5 Schematic illustration of ash hopper showing dimensions in mm.

3.3.2.1 Pressure Testing

Hydrostatic pressure tests to 7,3 MPa were conducted on the hopper unit in accordance with recognised standards. As a safety feature, a burst disc was incorporated on the hopper top flange valve assembly (c in Figure 3.14, Section 3.3.7). The rupture pressures of the burst disc, as specified by test certificate, were 3,4 MPa at 22°C and 3,1 MPa at 400°C.

3.3.3 FEED CONTROL AND VENTURI

It was initially envisaged that ash flow from the hopper be controlled by a three quarter inch gate valve, incorporated with a venturi nozzle. The venturi was fabricated from grade 430 stainless steel from the design calculations presented in Appendix B.
Ash flow calibration tests would take form of opening the feed valve to a prescribed setting (micrometer controlled) and running for a predetermined time. The ash passed could be accurately weighed and the relevant curves plotted for future testing.

3.3.4 TEST CELL

The test cell, as the component of the test apparatus to simulate the actual lockhopper erosion, required specific design consideration.
The constraints have been outlined in previous sections, but are listed below:

i) The test cell must operate at a pressure of 2,5 MPa,

ii) The test cell must be able to perform safely and efficiently at the ashlock operating temperature, namely 400°C

iii) The test cell must, as closely as possible, duplicate the flow patterns and velocities expected at the ashlock cone, namely 520 ms^{-1} (section 3.2.2)

iv) The test cell must provide the facility for varying valve geometries and materials.

The criteria for the design are, inter alia,

i) The test cell ought to be designed to avoid erosion and high temperature corrosion of the cell itself,

ii) test specimens should be easily changed

iii) the specimen dimensions should be such that sectioning is unnecessary for scanning electron microscope analysis.

iv) the test cell should incorporate a window for easy viewing of the particle erosion during testing.

The constraints and criteria have provided the basis of the design. Two categories of designs now apparent are firstly a scaled model type, and secondly, a sectional model based on the full size ashlock.

3.3.4.1 Scaled Model

A scaled model would be a replica of the full-scale seat/cone configuration as operates in a gasifcation system. The concept is shown schematically in Figure 3.6 overleaf.

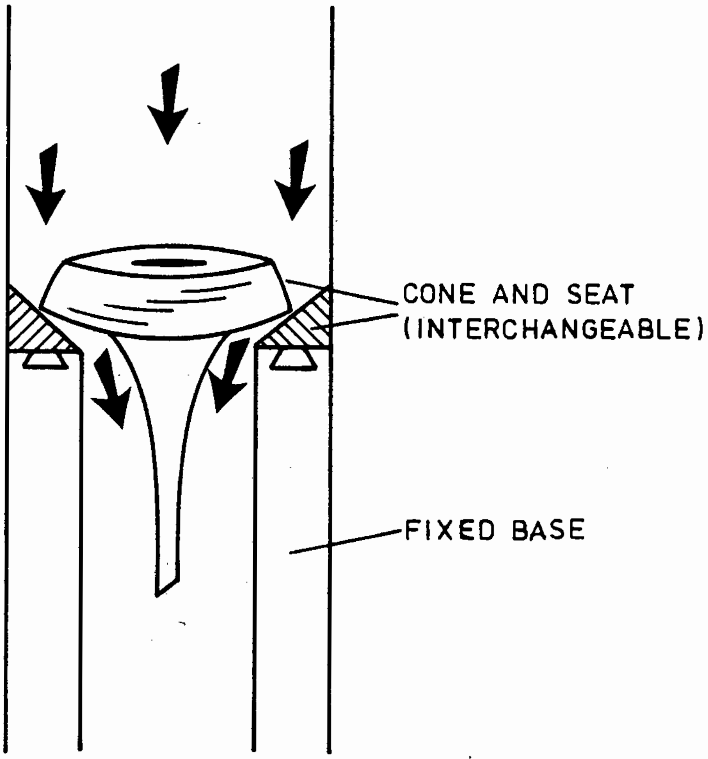

FIG: 3.6 Conceptual diagram of a scaled test cell showing seat and cone specimen positions.

The advantages of a scaled model include simplicity, ease of sealing and operation, and low cost. The disadvantages of a unit of this type, however, are :-

- scaling difficulties : the ash size ought to be reduced in proporotion to the scaled model.
- poor simulation of the in-situ flow conditions due to relatively larger boundary layers.
- poor viewing potential as the erosion contact line is concealed within the cone.

While the disadvantage of obstructed viewing is, as one of the criteria of the design, of a less serious nature, the effects of ash scaling and relative boundary layer interactions are more pertinent. Altering the ash fraction could have a significant and unrepresentative effect on the ersion experienced in the test specimen. (Section 2.1.1).

3.3.4.2 Sectional Model

The 'sectional model', as shown schematically in Figure 3.7, is in essence a 'slice' taken from the full-size ashlock cone. A 10 mm segment from the circumference of the full size seat is essentially flat and it was hoped, therefore, that in this way the scaling difficulties and flow conditions might be improved.

The disadvantages associated with a design of this nature are a possibility of poor sealing and a more complcated fabrication process. However, due to serious drawbacks associated with the scaled model, it was decided to incorporate the alternative sectional model in the test rig.

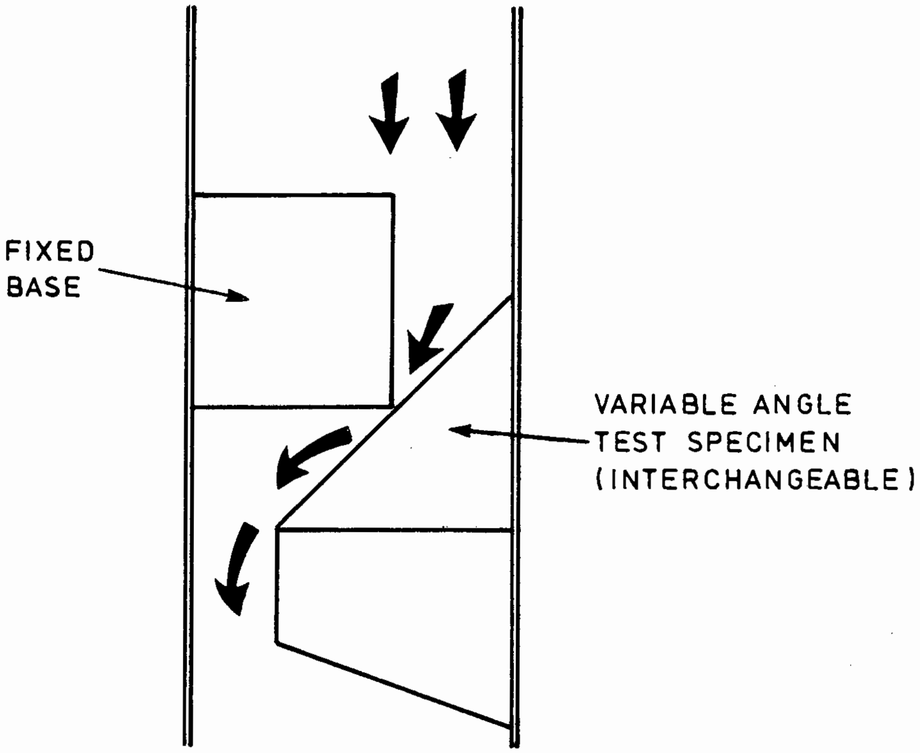

FIG: 3.7 Schematic representation of the proposed sectional test cell.

3.3.4.3 Description of Final Design

The test cell constructed can be separated into components of cover plates, body and specimen holder. Both the two 14 mm thick cover plates and the test cell body were machined from grade 316L stainless steel to inhibit possible elevated temperature corrosion as well as for mechanical strength.

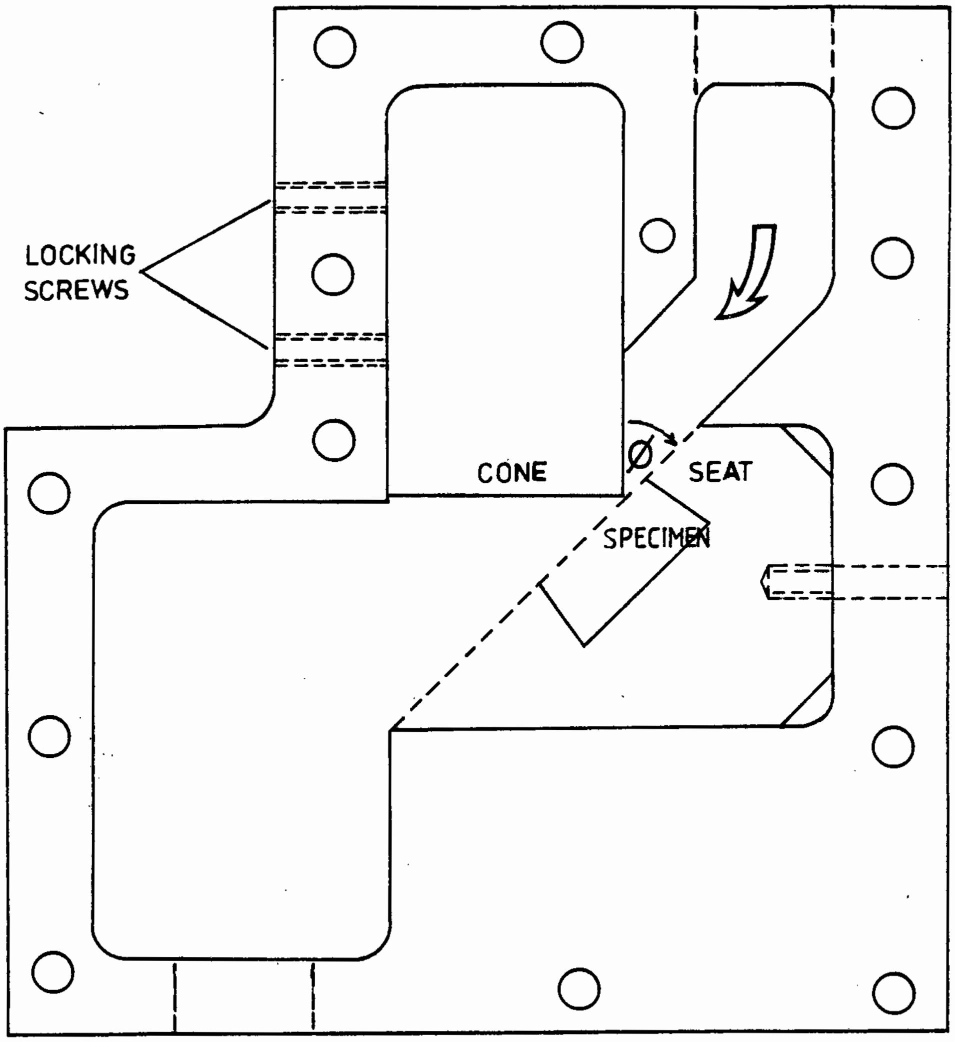

FIG: 3.8 Schematic view of test cell as designed from the sectional model showing specimen seat and cone orientations and seat/cone angle, Ø.

Figure 3.8 shows the layout of the test cell body with the relevant features labelled. The geometry duplicates the sectioned geometry through the ashlock seat/cone, while the 'seat cone angle' as pertaining to the test cell is defined as the inlet angle subtended by the seat and cone specimens upstream of the preset test gap (Ø in Figure 3.8). The specimen holder (see section 3.3.4.4) and the valve/cone sections are locked into position by means of setting screws, the desired gap size having been preset by means of a feeler guage (section 3.5.2). Various stages in the assembly of the test cell are shown in Figures 3.9 and 3.10.

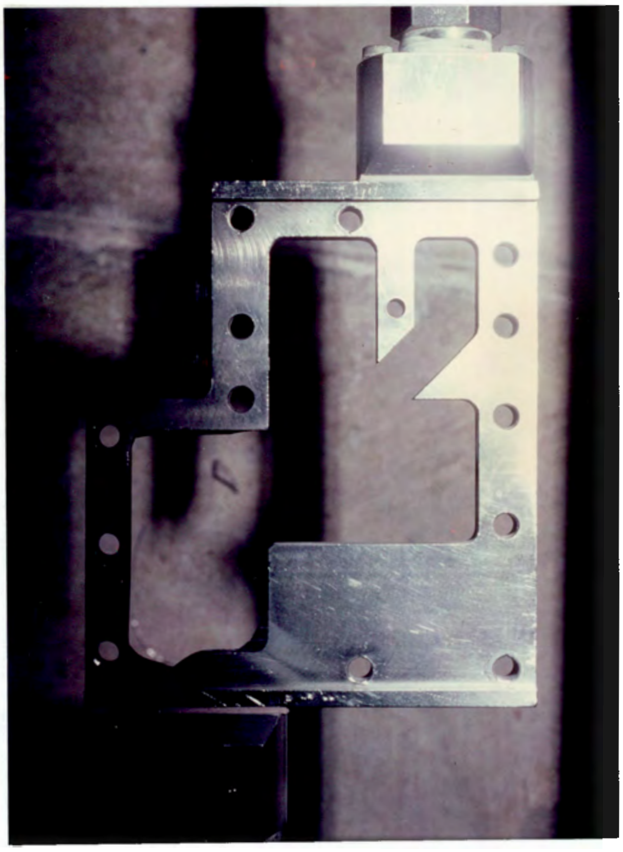

FIG: 3.9 Test cell body as constructed.

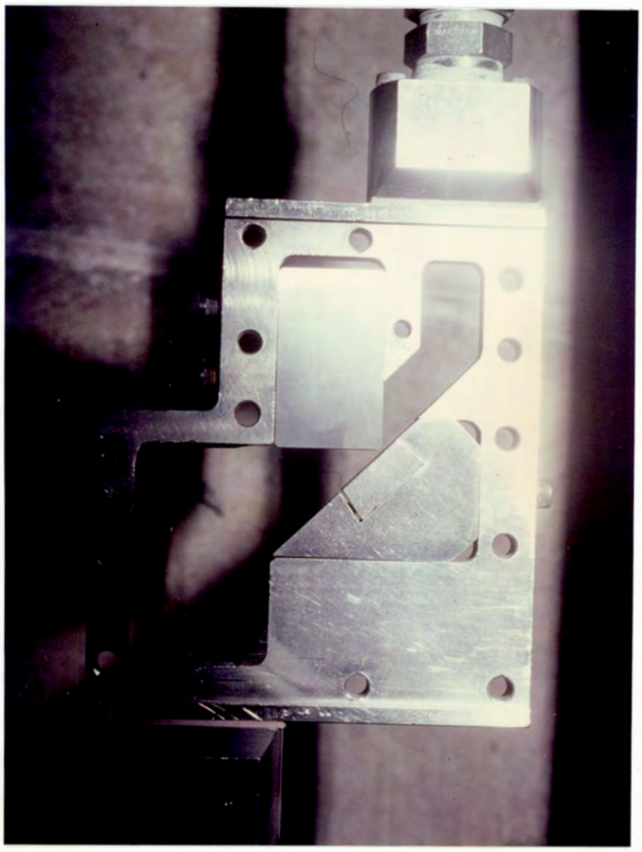

FIG: 3.10 Test cell with seat and cone sections in position as for testing.

3.3.4.4 Specimen Design

The primary requirements when considering the shape and dimensioning of the test specimens were ease of manufacture and the physical size restrictions applied by the scanning electron microscope specimen stage. As the testing programme would encompass certain "special" wear and erosion resistant materials (Chapter 4), sectioning after test would be undesirable. A further advantage would be ease of fixing the test specimen into the test cell where an intricate design would cause time delays on testing.

The specimen shape decided on was trapezial, the dimensions of which, together with those of specimen holder, are presented in Figures 3.11a and 3.11b respectively.

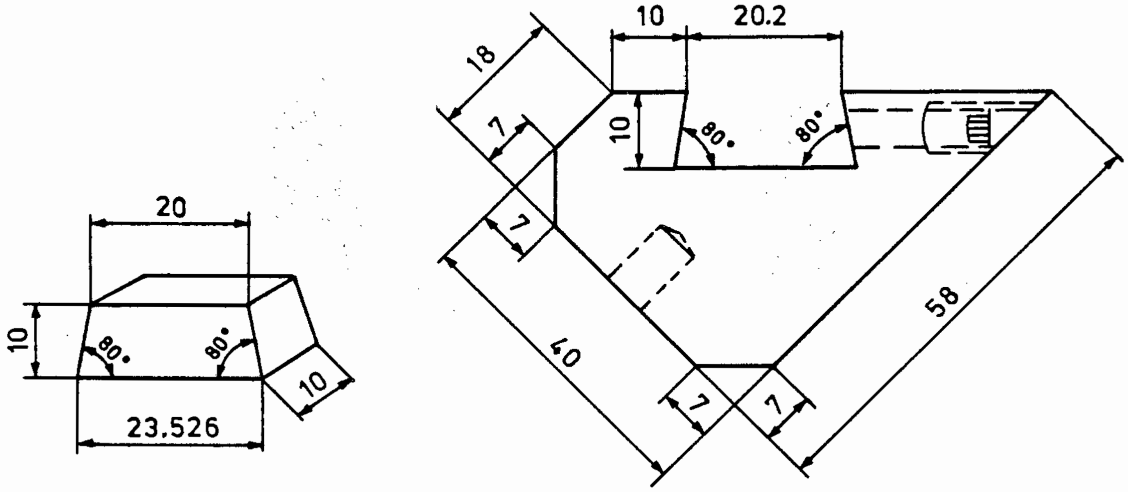

(a) (b)

FIG: 3.11a and 3.11b Trapezial test specimen (a) and specimen holder (b) showing dimensions in mm.

The sample inserts are secured into the dovetailed holder by means of a grub screw. Although examination of failed full-scale valves suggest limited erosion damage to the cone section of the valve, it was decided to include a replacable 'cone' specimen in the test cell. This specimen was rectangular, dimensioned 50mm x 30mm x 10mm, with a one mm wide chamfer at the seating face, as on the full scale valve.

3.3.4.5 Gaskets

As a sealing aid against the pressure and temperature environment, gaskets were cut from 'Permanite' asbestos gasket material. Initial tests, however, resulted in severe erosion of these gaskets, threatening damage to the test cell cover plates. It was therefore decided to use gaskets fashioned from a 0,7 mm thick grade 304 stainless steel sheet, in conjunction with a backing of 'Permanite'.

3.3.5 ASH COLLECTION

The fine, particulate nature of the ash used as the erodent rendered it imperative to devise a practical and efficient system of ash collection during testing. The extraction methods discussed included precipating the ash through a water spray and removing it as a slurry, as well as using a cyclone to separate the particles. The water spray method was dicounted as the concentration of ash to water in a slurry is approximately 2-5 percent, which would necessitate excessive amounts of water to settle a single drum of ash. Although comprehensive cyclone design literature is available (68,69), the relatively low air flow rates calculated to maintain homogeneous two-phase flow, together with the associated high ash concentration, precluded the use of a cyclone. Consequently it was decided to construct a gravity settling chamber with an outlet to an industrial air filter unit capable of extracting particle fines (10µm) from the passing air flow.

In order to obtain ash flow rate measurements, it was necessary to weigh the ash passed through the test cell in a given time. To overcome the undesirable manual de-ashing of the unit and weighing of the erodent separately, the entire ash trapment unit was suspended from an assized scale capable of readings up to 30 g of ash. For the purpose of room temperature calibration tests, the ash trap, as shown in Figure 3.12 was connected to the test cell by means of flexible hose. The unit is a modified ash drum to which an air filter unit is attached. The lid is easily removable to assist in de-ashing the drum when full, while being securely clamped in place during testing.

FIG: 3.12 Suspended ash trap to facilitate ash mass recording with air filter unit evident.

3.3.6 ASH HEATING

3.3.6.1 Options

Two options were considered when approaching the question of heating the test system to the 400°C test temperature. These involved heating either the air stream and introducing the room temperature ash into the preheated gas, or preheating the ash to 400°C and feeding this into the carrier line. Intuitively, it was considered that, on heating the carrier gas and introducing a five percent by volume ash flow into it, the temperature drop of the system would be negligible.

However, theoretical calculations suggested the contrary. A greater power input is needed to heat the 5% ash as compared to the air. The calculations are presented below.

The relevant equations are :

Power Input, $P = m.Cp.T$

and mass flow rate, $m = \rho \cdot Q$

where

P is the Power input (Js^{-1})

m is the mass flow rate (kgs^{-1})

Cp is the specific heat ($Jkg^{-1}K^{-1}$)

T is the temperature increase (K)

ρ is the density (kgm^{-3})

Q is the flow rate (m^3s^{-1})

Air Heating

Dry air density at 20°C (0,1 MPa)
= 1,2047

Moist air density at 20°C (2,5 MPa)
= 1,2047 x [B-0,3783c/760]

(dew point taken at 10°C) = 1,1992

Moist air density at 2,5 MPa (20°C) $= 1,1992 \times \frac{25}{1}$

$= 29,98\ \mathrm{kgm^{-3}}$

From the above data, power needed is approximately 35,9 kW.

Ash Heating

Density of ash (major constituent quartz)=220 $\mathrm{kgm^{-3}}$
specific heat = $0,75 \times 10^3\ \mathrm{Jkg^{-1}K^{-1}}$
ash flow rate = $1,5\mathrm{x}10^{-4}\ \mathrm{m^3s^{-1}}$

The calculated power rating is therefore 94,1 kW. Thus it is evident that, despite only a five percent by volume ash flow, the power output necessary to heat the air stream is 38 percent of that required to raise the ash temperature by 380°C.

Consequently it was imperitive to heat both the compressed air and the erodent particles.

The design adopted involved suspending heating elements into the ash, within the hopper. The heating of the compressed air was to be performed by either a flame or electrical heating system. This problem, however, was avoided by a design and operating procedure change arising from ash flow problems on testing. These problems and the resultant solutions and modifications to the prototype test rig are outlined in subsequent sections.

3.3.6.2 Selected Option

The heaters selected were 3kW Inconel sheathed elements, 3,6 m in length with surface watt density of 3,2 $\mathrm{Wcm^{-2}}$. Connection was made through the hopper top flange by means of 'heating bolts' as shown schematically in Figure 3.13.

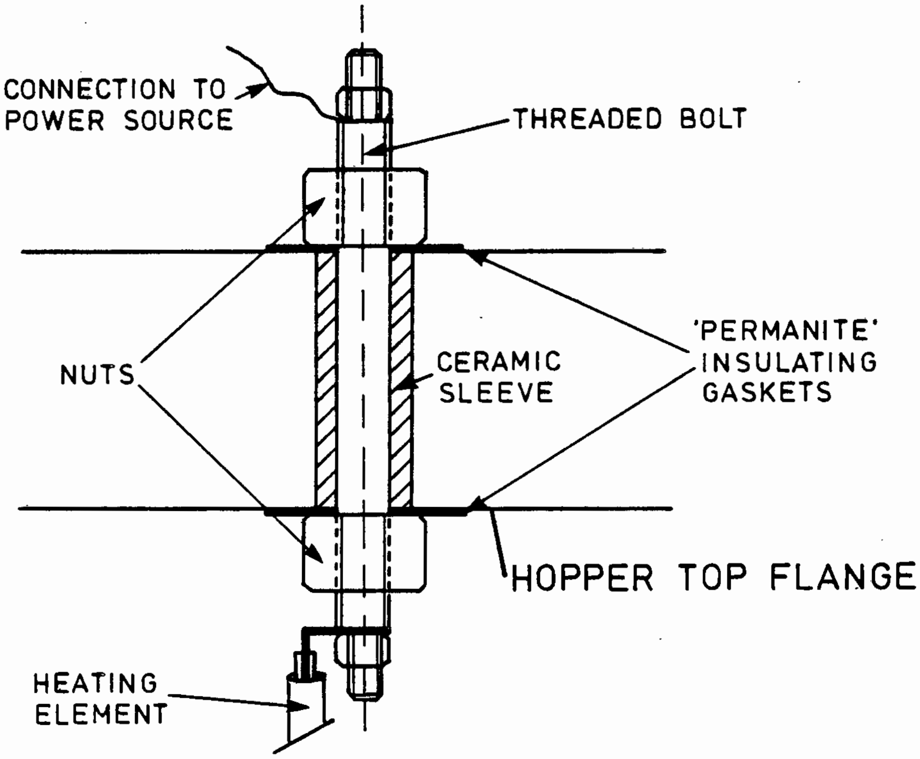

FIG: 3.13 Schematic view of heating bolts connecting heating elements through the hopper top flange.

The elements were connected to a temperature controller and a digital temperature readout, these components being detailed in section 3.5.2.1.

3.3.7 LOADING SYSTEM

The ash loading system had necessarily to be efficient, simple and safe. A pneumatic loading system was investigated and found to be the most suitable method. By using an industrial vacuum cleaner as the vacuum source, the ash is effectively 'sucked' into the hopper via a gate valve on the hopper top flange (See Figure 3.14). The vacuum was attached to a 25 mm bore gate valve on the hopper [a in Figure 3.14] by a 75 mm flexible hose, while the ash suction hose (50 mm) was attached to a 25 mm bore gate valve [b in Figure 3.14].

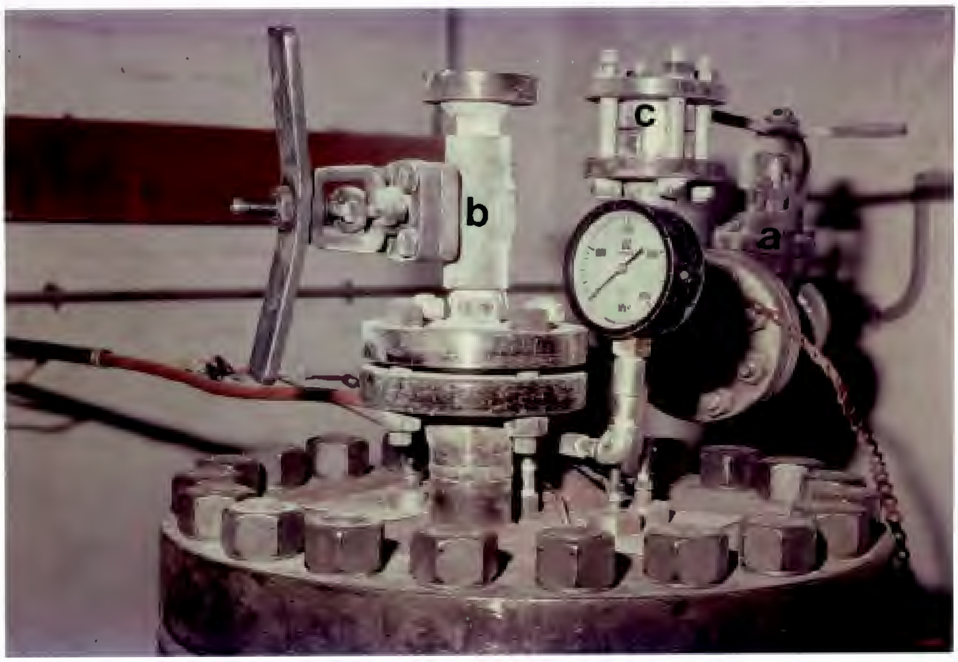

FIG: 3.14 Valve assembly for ash loading showing 50 mm gate valve (a) to vacuum source, 25 mm gate valve (b) to ash sample and burst disc (c).

Calibration test results for the loading system are presented in Chapter 4 (Calibration loading system).

3.4 OPERATING PROBLEMS

On commencement of room temperature testing, certain unforseen problems soon became apparent, impairing the operational efficiency of the test rig. This section outlines the problems experienced, the proposed solutions and the action taken relating to the straight forward problems. The more detailed modifications are presented in a subsequent final design section (Section 3.5).

3.4.1 TEST CELL BLOCKAGE

The proposed gate valve (Section 3.3.3) was unsuitable as an ash feed control mechanism. The operation of the valve was too coarse to deliver a regular, controlled flow, resulting in excessive or uncontrolled amounts of ash passing through from the hopper through the test cell. The test cell gap, therefore initially set at 0,8 mm, regularly clogged with ash. The blockage in the test cell effectively sealed against the 2,5 MPa working pressure and in effect halted the test in progress. This problem was further compounded by the workings of the gate valve becoming clogged with the erodent, thereby preventing efficient valve closure.

This problem was solved by increasing the test cell gap size from 0,8 mm to 1,5 mm as well as replacing the gate valve with a non-adjustable 'on-off' plug valve (Figure 3.15).

FIG: 3.15 Hopper base assembly showing outside thermocouple attachment (a), ash feed valve (b), prototype air inlet line (c), and venturi chamber (d).

Various valve spindle hole sizes were investigated to optimize and standardize the ash flow through the test cell, while avoiding both clogging and 'ash starvation' (section 3.4.2). The optimum spindle hole diameter was found to be 3 mm. Due to erosion by the passing ash, periodic replacement of the feed valve spindle was necessary, although spindles of carbides and ceramic inserts are being considered.

3.4.2 ASH FLOW

Poor flow characteristics of the erodent led to periodic interruption and stoppages during testing due to 'ash starvation'. Two variations of this 'ash starvation' were 'bridging' and 'funneling'. Bridging resulted from, on commencement of testing (opening the feed valve), the ash surrounding the plug valve being removed, leaving a bridge of ash of sufficient stability to resist collapse (Figure 3.16a).

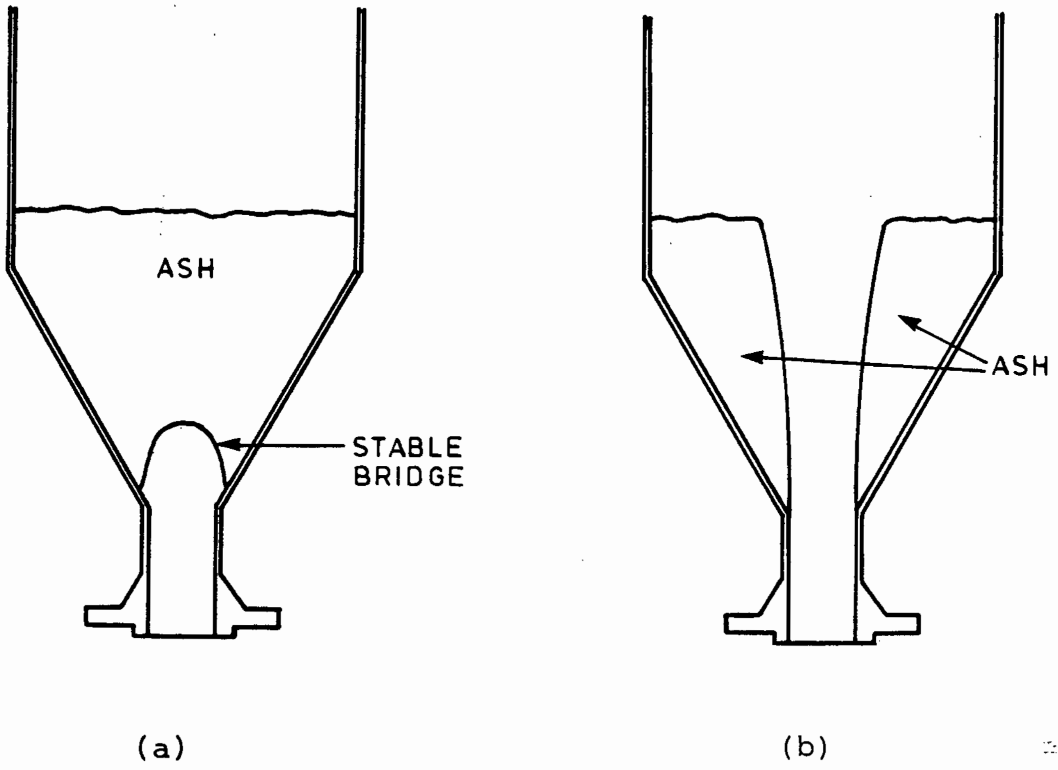

FIG: 3.16a and b Schematic illustration of ash bridging (a) and funneling (b) resulting in ash starvation.

The funneling effect is similar in that only a proportion of the ash is drawn from the hopper on testing. The ash directly above the feed valve being removed, the bulk of the erodent remaining packed against the hopper walls (Figure 3.16b).
Modifications proposed to overcome the ash flow problem included incorporating a 'shaker-vibrator' attachment to the side of the hopper and a mechanical stirrer device (as used successfully by Mobbs, Bowers, Riches and Cole (22) at lower pressures) into the ash. A vibrator mechanism was however found to aggravate the bridging problem, while the practical problems of successfully inserting a stirrer into the hopper precluded its use.

The final proposal to be considered involved fluidizing the ash by means of the pressurizing air stream. This proposal, in which the ash would theoretically attain fluid characteristics and thereby reduce any possibility of flow starvation, was accepted as the proposed solution to the problem. The implementation of this design is discussed more fully in section 3.5.3.

3.4.3 HEATING ELEMENTS

While the principle of ash heating by use of elements suspended in the ash was sound, and the system operated satisfactorily at temperatures up to 150° C, the poor heat conductivity of the ash resulted in sporadic overheating and melting of the elements (Figure 3.17).

FIG: 3.17 Example of failed heater element sections with evidence of melting and fused ash.

3.5 FINAL DESIGN

As a result of the operating problems experienced, certain modifications to the previously described test rig were necessitated. While the test rig design remains nominally as outlined, these changes represent the rig as it presently operates.

3.5.1 FLUIDIZING PORTS

The major concern engendered by the incorporation of a fluidizing system into the ash hopper, was the limited design change capacity available within the design constraints of the in-service hopper. The design adopted positioned the fluidizing openings 60 mm above the feed valve orifice. In an attempt to forestal any bridging or funneling at a higher level in the hopper, one of the ports was extended up into the cone section of the hopper. The entry into the hopper was made via a reducing connector into which two tube connectors were fitted.

The fluidizing lines were constructed from quarter inch stainless steel tubing, each with the facility for independent operation by means of a quarter inch ball valve placed in the line. These modifications are labelled in Figure 3.18 below.

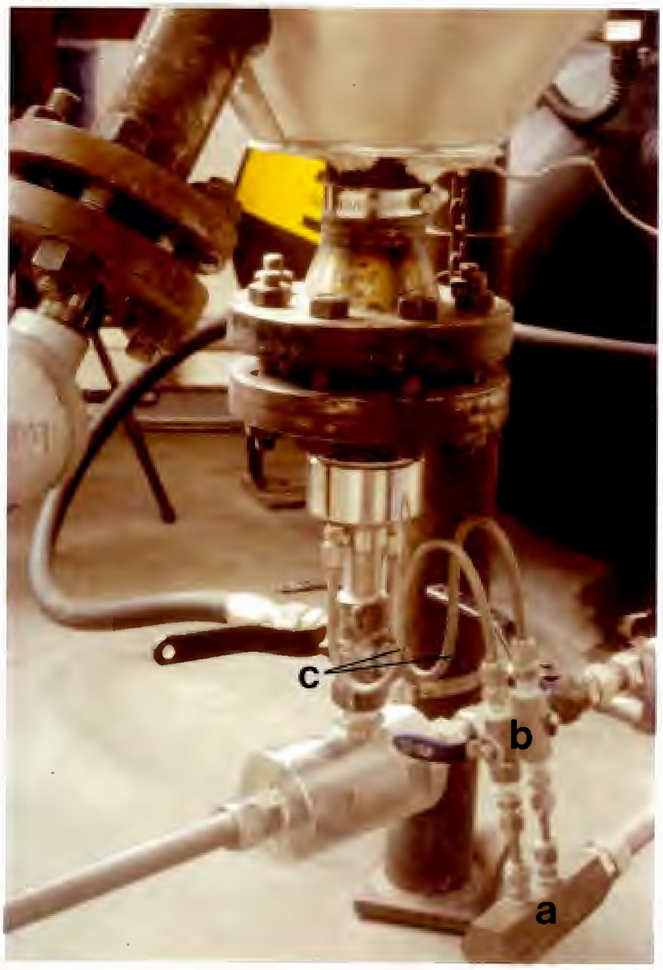

FIG : 3.18 Fluidizing system comprising a manifold (a), ball valves (b) and 6,3 mm fluidizing tubes (c) into hopper base.

3.5.2 HEATING SYSTEM

The reasons for the repeated element failures within the hopper were the combination of the uncontrolled energy output of the elements and the poor heat conductivity of the ash to be heated. The fluidizing modification proposed to improve the ash flow during testing would therefore also benefit ash heating.

3.5.2.1 Temperature measurement and control

The heater control unit, the components labelled, is shown in Figure 3.19.

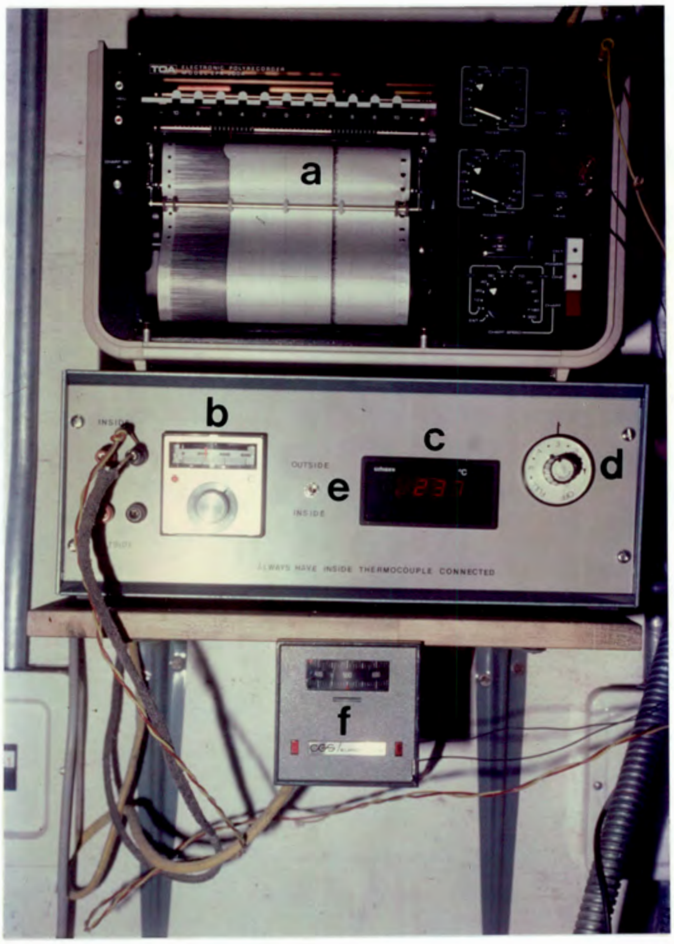

FIG: 3.19 Heater control unit showing chart recorder (a) thermowell controller (b), digital temperature readout (c), power control (d), thermocouple selector switch (e), and the element temperature controller (f).

The temperature of the ash is monitored by an Iron-Constantan thermocouple positioned inside the hopper connected through the wall via a thermowell.

This thermocouple, referred to as the 'inside' thermocouple, is in turn connected to the thermowell control unit which operates the switching of the elements. This thermocouple records the temperature of the ash, which is compared to that preset on the temperature controller. On the ash reaching a predetermined value, the temperature controller activates a relay system which in turn switches off the elements. A second thermocouple attached to the hopper above the ash feed valve serves as a monitor of wall temperature at the hopper base. This 'outside' thermocouple is strictly a recorder device, with no element control facility.

A digitial temperature readout displays the readout from either thermocouples individually. To forestall future element melting, a type-J thermocouple was attached, via the hopper top flange, to the Inconel element sheath suspended within the ash. This thermocouple, coupled to a element temperature control unit preset at 500°C, ensured element surface temperature control by activating the heater relay system, as with the 'inside' thermocouple system. The wiring diagram for the heater control system is presented in Figure 3.20 overleaf.

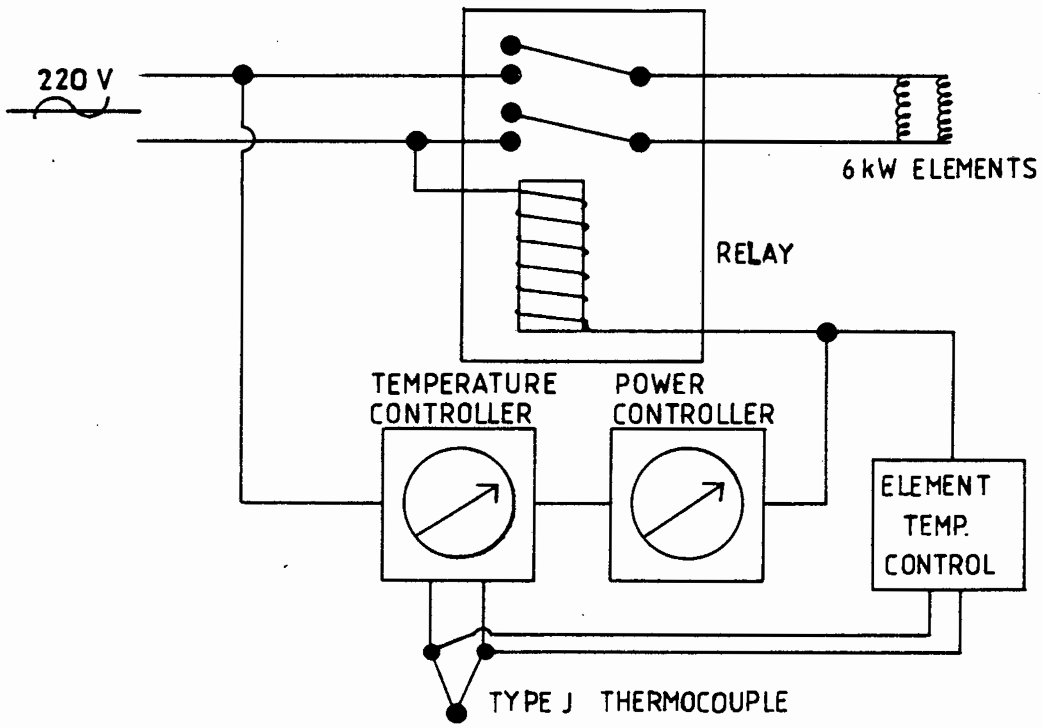

FIG: 3.20 Heater control wiring diagram.

3.5.2.2 Power Controller

In order to reduce the energy output of the elements, an energy or power controller was fitted to the heater controls, shown in Figure 3.19. This controller regulated the heating time, or effectively the "on" time, of the elements. The numbered settings on the controller dial correspond to the percentage time the elements are heating at full power. This intermittent heating allows sufficient time, together with the effects of fluidizing, to dissipate the generated heat, thereby minimizing the effects of local overheating. The power controller calibration plot is presented in Appendix D.

3.5.2.3 Specimen Heating

The question of heating the test cell and specimen to the test temperature of 400°C was also addressed.

It was considered, however, that the surface layers of the specimen would soon attain the ash temperature on commencement of testing. The ash, with its associated high heat capacity, was expected to lose limited energy prior to impact at the specimen surface. While it is realised that the entire specimen would not attain the test temperature, it is only the surface region which is affected by the erosion, and therefore, it was considered that temperatures approaching 400°C would be realized in this area seconds after the commencement of testing. Attempts at monitoring the temperatures attained in these surface layers were dismissed as impractical due to (i) severe erosion of any temperature recording device affixed to the sample, and (ii) shallow depths (±100 μm) at which the probes should necessarily be positioned would be extremely difficult to monitor.

Throughout the elevated temperature testing programme it was endeavoured to maintain the temperature parameters and heating times as constant as possible, thereby assuring that, while if not necessarily at the precise theoretical temperature, the results are reproducable and constant.

3.5.3 CARRIER LINES AND HOSES

The fluidizing lines and mixing tube connecting the venturi and the test cell, were all fabricated from grade 316L stainless steel. A hoop stress analysis to calculate the safe operating wall thickness was performed and is presented in Appendix C. High pressure flexible hose was used to connect the receiver to the carrier line and to the fluidizing parts. With reference to Figure 3.21, a plug valve with a 3,5 mm spindle (5), was positioned as a shut-off upstream of the venture nozzle (4), while a 6 mm plug valve (6) was fitted into the fluidizing line, isolating the two fluidizing ball valves (1).

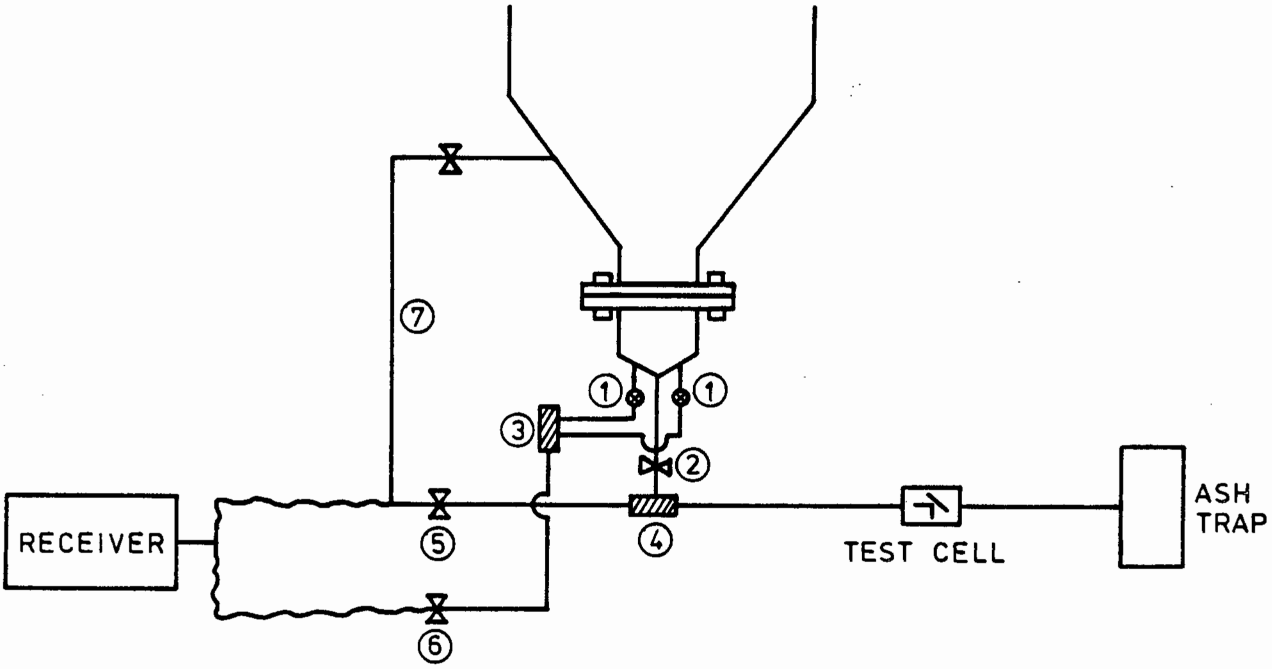

FIG: 3.21 Test rig valve configuration and orientation in final design.

1. ball valves
2. ash feed valve
3. manifold
4. venturi
5. carrier line shut-off valve
6. fluidizing line shut off valve
7. prototype pressurizing line.

3.5.4 CHANGES IN OPERATING TECHNIQUE

The major change in operation involved discontinuing the use of the carrier line during testing. The hopper is pressurized via the fluidizing ports until both the receiver and hopper have equilibrated at the working pressure of 2,5MPa. This procedure does not use the venturi as a pressure differential source but rather as a mixing chamber.

An advantage of the procedure is the simultaneous heating of the erodent and the carrier gas in the same vessel, thereby foregoing the need of separate air heating systems. Further, the single heating chamber results in improved temperature uniformity and temperature control. This system of testing simulates the actual ashlock valve situation more closely in that a homogeneous ash/air mixture flows from the gasifier (hopper) through the failed valve (test cell).

CHAPTER FOUR

EXPERIMENTAL METHOD

4.1 ERODENT ANALYSIS AND PREPARATION

4.1.1 PARTICLE SIZE ANALYSIS

Considerable differences were noted in the ash size distribution of the erosion samples supplied. Size distribution variations within individual drums necessitated mixing to ensure uniformity of the ash and thus avoid the undesirable influence of varying size distribution on erosion results.

The size distribution of the erodent ash over a series of samples was determined by a dry sieve analysis (D197 ASTM standards 1980 part 14). Possible inaccuracies in the sieve analysis arise from :

i) the fact that sieves sort according to shape as well as size,
ii) incomplete sieving (materials lost on a sieve mesh) and
iii) a lack of uniformity in sieve mesh size.

The sizes of the Endecott test sieves used were 600 μm; 212 μm; 106 μm; 63 μm and 38 μm. Prior to sieveing, a mechanical sample splitter complying to ASTM standards was used to minimize variations in characteristics between test and field samples.

4.1.1.1 As received drums

The sieve analyses of the top, middle and bottom sections of the ash in drums 'as received' are presented in Figure 4.1 as a plot of "percentage of sample" versus "equivalent spherical diameter" in µm. Each curve represents the mean of four tests.

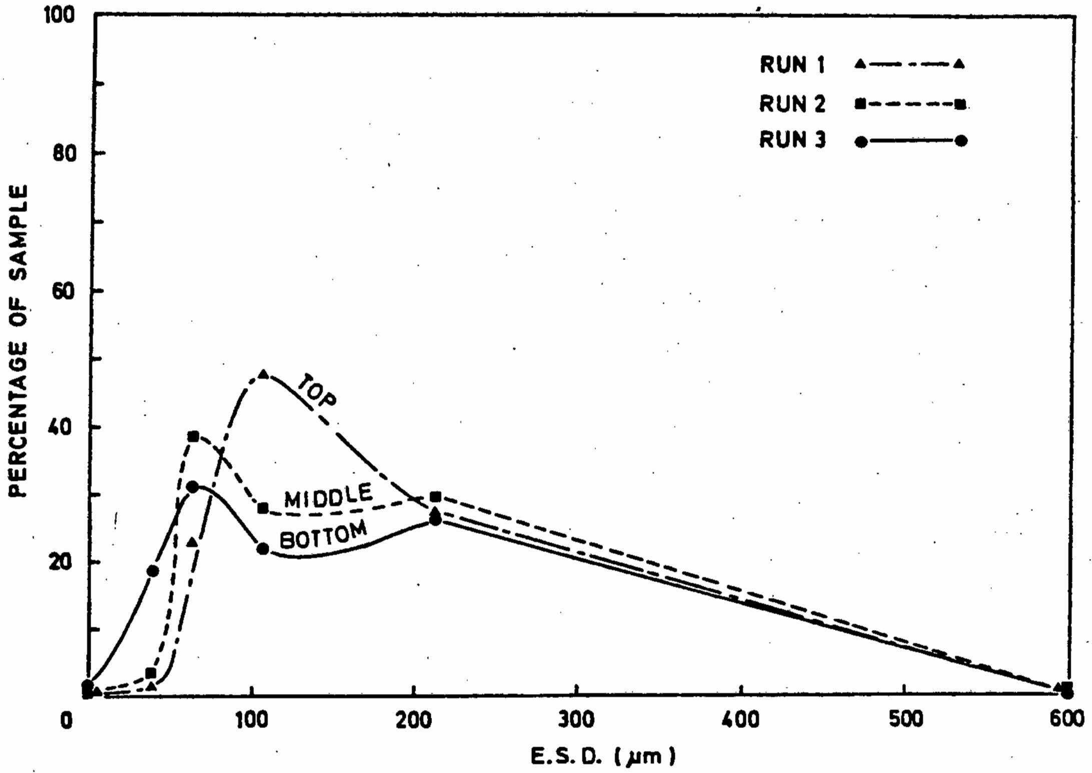

FIG : 4.1 Percentage erodent sample versus equivalent spherical diameter in µm.

Consideration of the curves verifies a differing size distribution through the as-received drum section, with the predominance of 'large' particles increasing towards the top sections of the ash drum. Conversely, the bottom section contains a relatively high percentage of sub-38 µm diameter particles.

4.1.1.2 Mixed sample

Due to the variations noted in Figure 4.1 above, it was necessary to carefully homogenize the ash in the received drums by blending in a concrete mixer. After mixing, a sieve analysis was performed on selected samples. The mean results are presented in Figure 4.2.

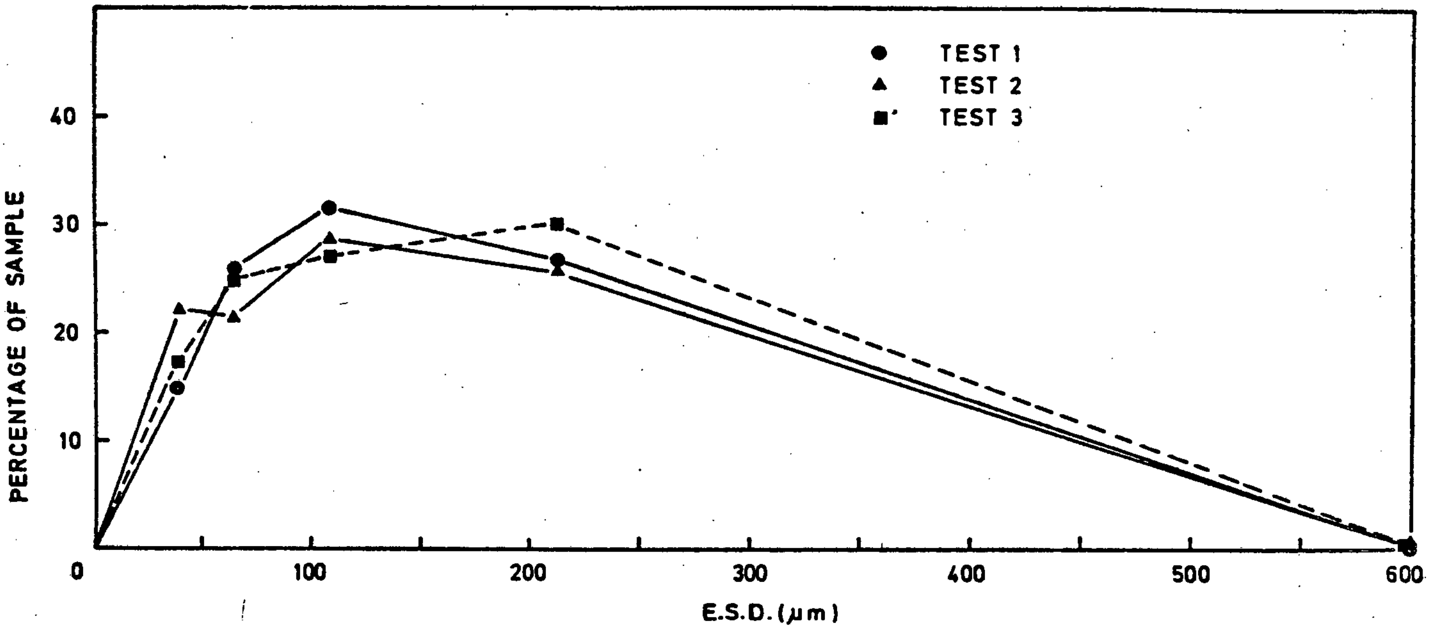

FIG : 4.2 Percentage sample versus equivalent spherical diameter in μm after mixing.

4.1.1.3 After erosion

The sieve analyses of erodent dust analysed after testing are presented in Figure 4.3. The curves represent three samples from a single test. With reference to Figure 4.3, a relative increase in the 'fines' fraction is evident in the dust after erosion as compared to the pre-erosion ash size distribution (Figure 4.2).

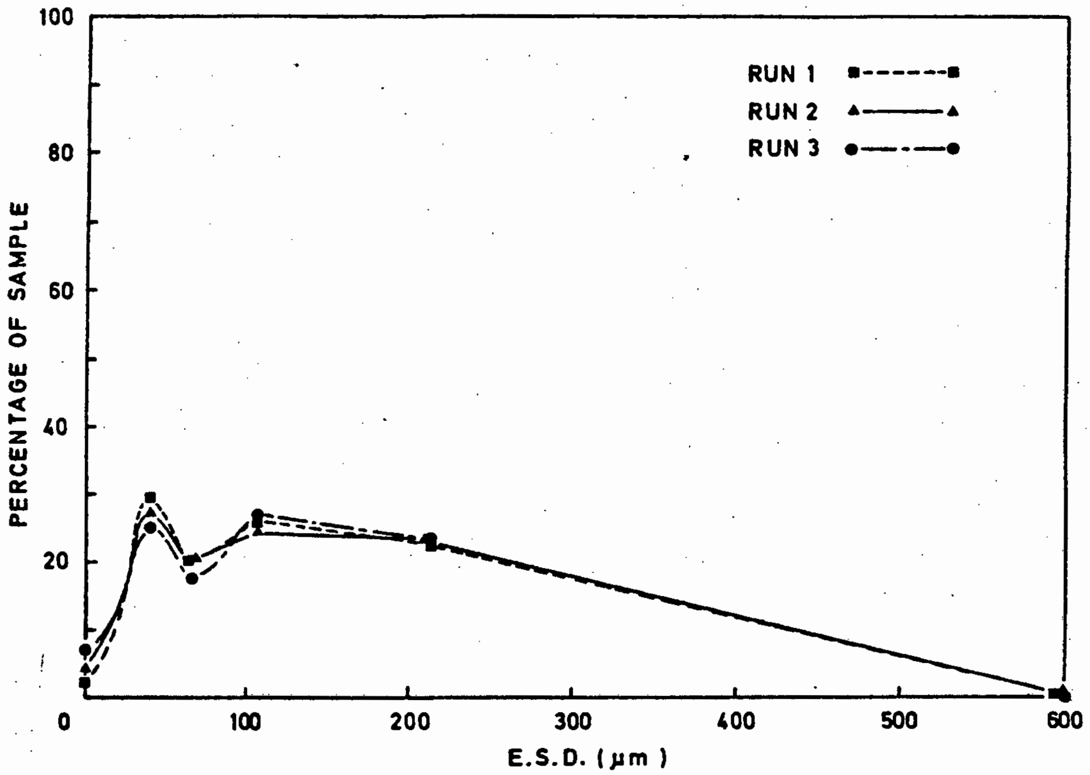

FIG : 4.3 Percentage sample versus equivalent spherical diameter in μm after erosion.

4.1.1.4 Operation II

For comparison purposes, a size distribution analysis was performed on an ash sample obtained from a similar gasification process. The sieve analysis is shown in Figure 4.4. The high incidence (approximately 53 percent) of particles larger than 212 μm in the nominally -600 μm sample is notable. This result emphasizes the need for careful quantification of the erodent fraction prior to testing, and highlights the possible differences in size distributions within nominally similar samples from different areas and processes.

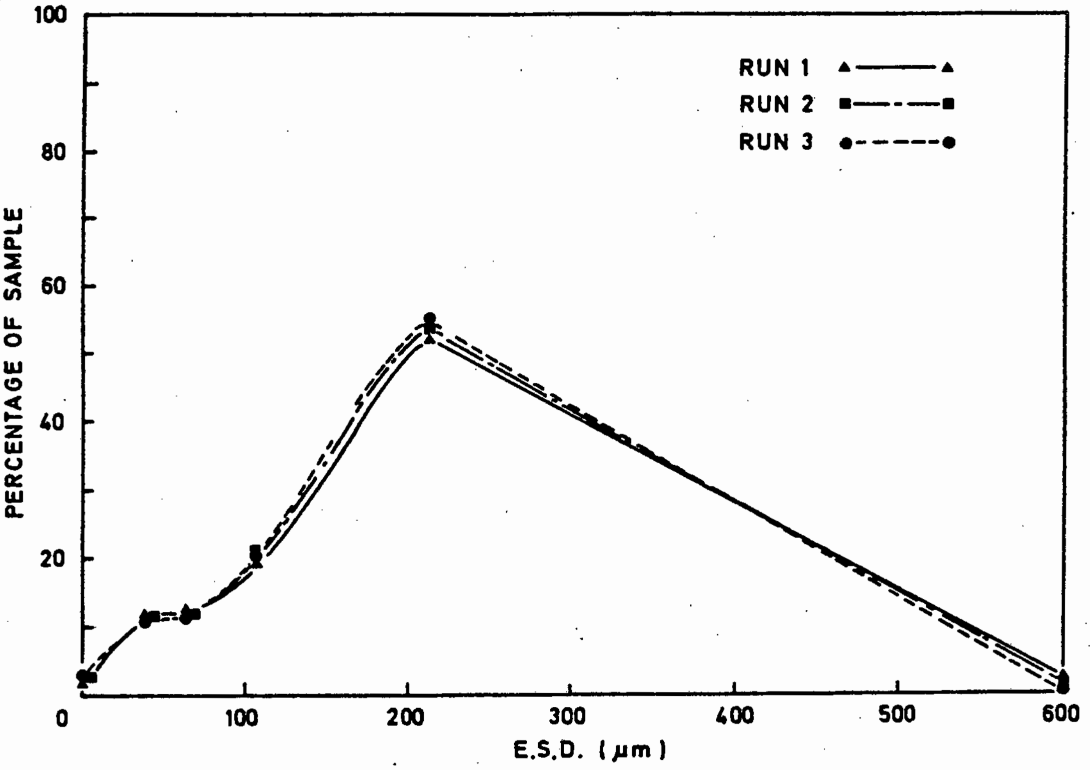

FIG : 4.4 Percentage sample versus equivalent spherical diameter of ash taken from Operation II.

4.1.2 CHEMICAL ANALYSIS OF ERODENT

Chemical analysis by X-ray flouresence and characterization of particle shape and size of the erodent ash was conducted by a colleague (70). The ash content of the ash is approximately 35 percent. The percentage chemical composition is presented in Table 4.1.

TABLE 4.1 : Element composition of typical ash sample as used in the test programme.

ELEMENT/OXIDE COMPOSITION	PERCENTAGE (OR OTHERWISE INDICATED)
SiO_2	52,4
Al_2O_3	31,8
C	4,0
Fe_2O_3	3,9
CaO	2,9
MgO	1,5
Na_2O	1,2
K_2O	0,5
S	0,2
L O I*	5,0
F^-	120 ppm
I^-	100 pp,

(* Loss on ignition)

4.1.3 SIEVING

As a result of the incidence of 'rogue' or outsize particles and conglomerates in the nominally -600 µm despatched ash, it was necessary, after mixing of the various ash fractions, to resieve the erodent before testing on a 600µm sieve.

4.1.4 MOISTURE CONTENT

The moisture content of the ash was determined to be 0,3 percent by weighing a sample of erodent before and after drying at 110°C for eighteen hours.

4.1.5 ASH DRYING

In order to enhance the flow characteristics of the erodent and to further standardize the erosion parameters, the ash was dried on an open-bed drying tray at 150°C for approximately eight hours prior to testing.

4.2 MATERIALS TESTED

4.2.1 SELECTION OF STANDARD

In order to gauge the relative erosion performance of the various materials tested and to establish a ranking table of performances, the selection of a suitable standard was necessary. The choice of standard materials is influenced by, inter alia, factors such as availability, cost, machinability, and erosion mass loss of the specimen material in relation to materials to be tested. As regards the mass loss of the standard, sufficient erosive loss should be realized to obtain accurate reproducible results after a standardized test time. Based on preliminary test results, it was decided to incorporate a medium carbon steel (080M40) as the material standard. All standard specimens have been machined from as received single bar stock to negate possible inconsistencies in properties between melts.

4.2.2 PHYSICAL AND CHEMICAL PROPERTIES

During calibration of the test rig and initial testing, a selection of common engineering materials were tested. These materials were a medium carbon steel standard, 'Cobal 6' hardfacing weld material, type 304 austenitic stainless steel, and grade 101 free-machining brass. A further two 'special' materials, a Turbine Metals Technology diffusion coated cobalt-based material -TMT 51, and a Kennametal tungsten carbide/Cobalt in a 304L/Cu/Fe matrix system -KA2, were also evaluated. The nominal chemical compositions and relevant material standards as well as hardness and density values are noted in Tables 4.2 and 4.3 below.

TABLE 4.2: Chemical compositions in weight percent and relevant standards of materials tested.

Material	Percentage Chemical Composition
En8[1]	0,4C[+] 0,05-0,35 Si 0,6-1,0Mn 0,06S,P bal Fe
304 s/s	0,08C 18-20Cr 8-10,5 Ni bal Fe
'Cobal 6'[2]	0,11C 27-32Cr 3-6W 1-1,5Mn 1-2Si 1Ni 3Fe bal Fe
Brass[3]	58Cu 3Pb 39Zn
TMT 51[4] (Stoody 1)	1,8C 1,2Si 1,0Fe 1,0Ni 24,5Cr 12W bal Co
KA2	50-65Kenface[5](8Co,WCbal)28-33/304L + 15-25Cu/Fe alloy

1. Iscor En 8 080M40 (British Standard 970 of 1972)
2. "Cobal6" is a trade name; hardfacing weld material.
3. 101 free-machining brass based on British Standard 249.
4. Tubine Metals Technology WC diffusion coated sample.
5. Kennametal trade name.

\+ Carbon content analysed by arc emission spectroscopy and verified by wet chemical methods).

TABLE 4.3 Bulk density and hardness values of test materials.

Material	Bulk density (gcm^{-3})	Hardness (VPN30)
080M40	7,8139	215
Cobal 6	8,0223	417
304 s/s	8,0453	202
101 Brass	8,3698	124
TMT proc. 51	8,2239)	523 (base)
	)	642 (coating)
KA2	10,5496)	144 (binder)
	)	1900 (grains)

4.2.3 OPTICAL MICROSCOPY

Microscopy samples were prepared by sequential hand-polishing on a series of SiC-bonded papers with grit sizes of 180, 320, 500, and 800. Thereafter the specimens were polished on a diamond-paste impregnated cloth, from 3 μm diamond paste to one μm paste.

4.2.3.1 080M40 Standard (as received)

A low magnification optical micrograph of the standard material is shown in Figure 4.5 overleaf.

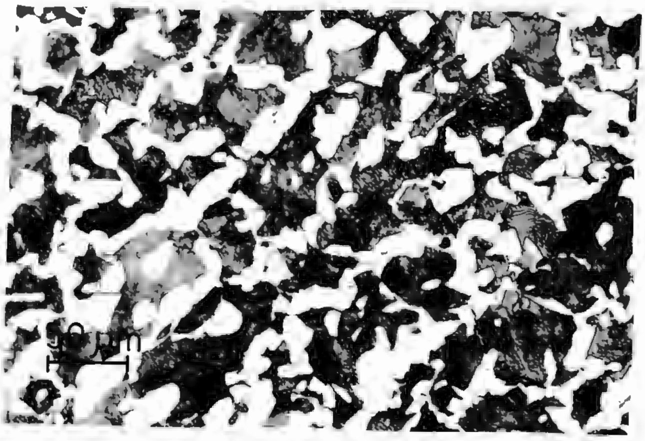

FIG : 4.5 080M40 structure showing a banded ferrite/ pearlite microstructure (2.5% nital).

The 'banded' structure or anisotropy of the ferrite/pearlite microstructure suggests a hot-rolling forming process with still air cooling. A high magnification micrograph of the same specimen is presented in Figure 4.6 below.

FIG : 4.6 High magnification view of Figure 4.5.

4.2.3.2 080M40 Heat treatments

The effect of various heat treatments on the erosion performance of 080M40 was also examined. The thermal treatment and specimen nomenclature are detailed in Table 4.4.

With the exception of the TMT and Kennametal samples, which were received ready for testing, the test specimens were machined from a single bar stock to avoid discrepencies between samples.

TABLE 4.4 Heat treatments of 080M40 medium carbon steel standard.

SAMPLE IDENTIFIER	HEAT TREATMENT	VPN30
A	080M40 as received; Hot rolled	215
Q	i) As received specimen heated at 820°C for 30 minutes ii) Oil quenched	564
T	As for Q i) tempered at 200°C for 30 minutes ii) water quenched	476
TA	As for Q i) tempered at 400°C for 30 minutes ii) water quenched	397
TT	As for Q i) tempered at 600°C for 30 minutes ii) water quenched	308

The microstructures corresponding to the various heat treatments of 080M40 are presented below.

Initial attempts at water quenching the austenitized specimens resulted in frequent (± 50%) instances of quench cracking of the trapezoid specimens. Consequent quenches into oil forestalled specimen cracking while rendering a martensitic structure at room temperature as illustrated in Figure 4.7.

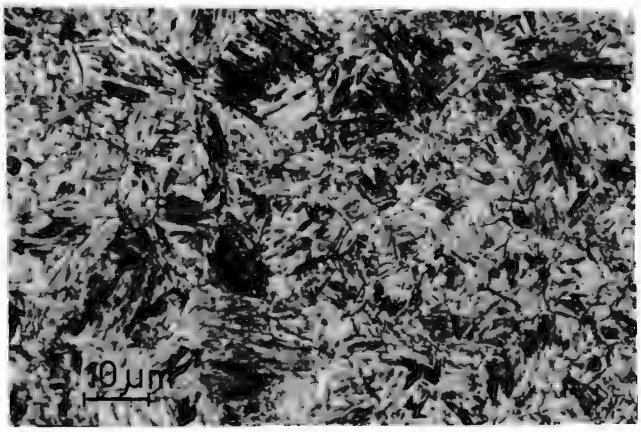

FIG : 4.7 High magnification optical micrograph of 080M40 water quenched from 820°C showing martensitic structure (2.5% nital).

The tempering process at 200°C for 30 minutes results in a softening of the martensitic body-centered tetrogonal structure by limited carbon diffusion from the strained lattice. The microstructure of heat treatment "T" is shown in Figure 4.8.

FIG : 4.8 Structure of sample as quenched from 820°C and tempered at 200°C for half an hour.

Figures 4.9 and 4.10 illustrate the effect of increasing the tempering temperature from 400°C to 600°C respectively. Tempering at 400°C for 30 minutes allows further interstitial carbon precipitation from the body centered tetragonal matrix in the form of carbides. Also noted is the appearance of ferrite grains (white) from the tempered martensite phase.

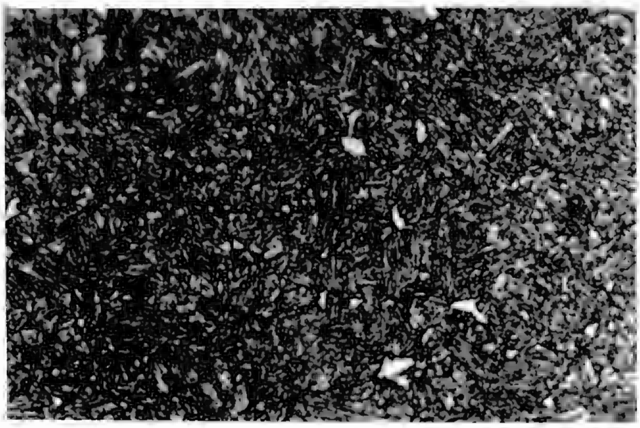

FIG : 4.9 080M40 oil quenched from 820°C and tempered at 400°C for half an hour.

This process is continued in the 600°C temper with extensive carbide precipitation evident, as well as enhanced ferrite grain growth.

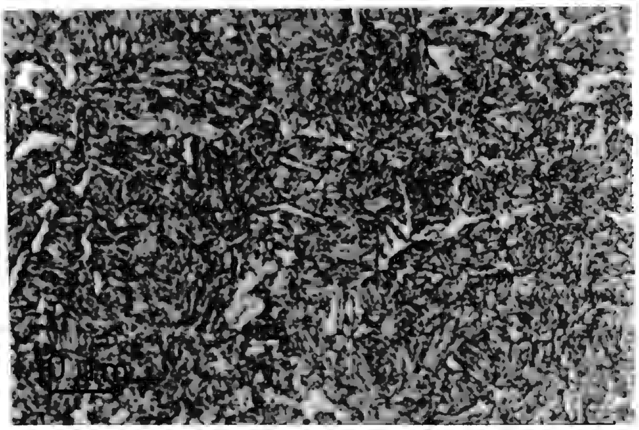

FIG : 4.10 As for Figure 4.9 but tempered at 600°C for half and hour.

4.2.3.3 Cobal 6

The as-cast structure of the 'Cobal 6' hardfacing weld material showing the dendritic nature of the casting is illustrated in Figure 4.11.

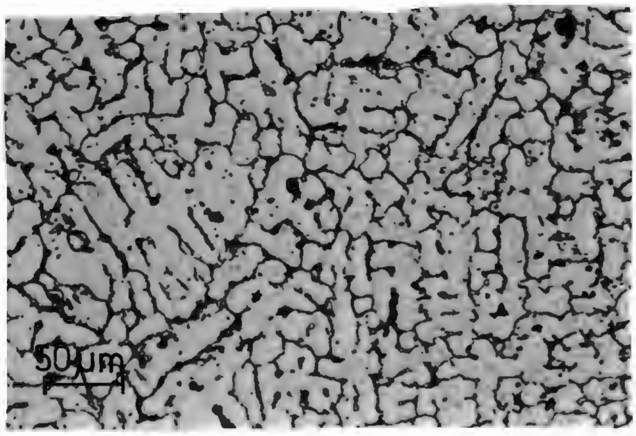

FIG : 4.11 Dendritic nature of as-welded Cobal 6 seat. (hot oxalic acid electro-etch).

Fine carbide precipitation within the structure is evident in Figure 4.12.

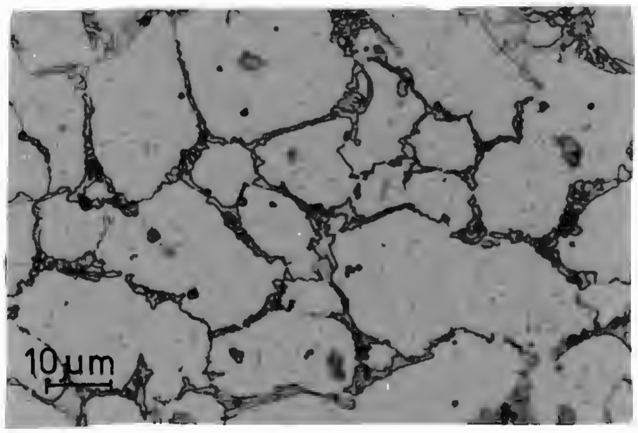

FIG : 4.12 High magnification of Figure 4.11.

4.2.3.4 304 Austenitic stainless steel

A low magnification micrograph of the hot-rolled 304 specimen is shown in Figure 4.13.

FIG : 4.13 Low magnification microstructure of 304 S/S test specimen showing sulphide stringer orientation (Oxalic acid).

Features such as equiaxed austenite grains, annealing twins and stringers may be noted in Figure 4.13 and Figure 4.14, a high magnification micrograph of the above specimen.

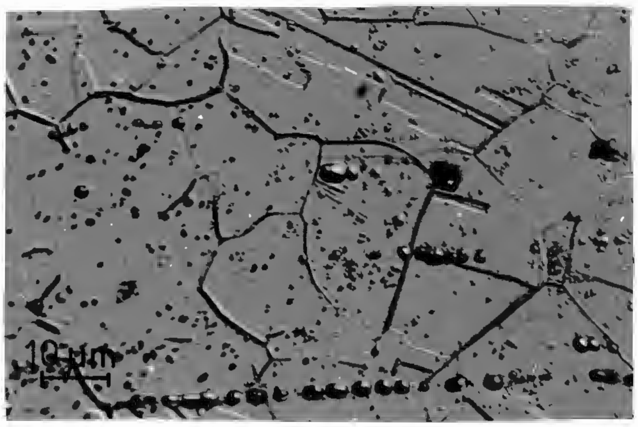

FIG : 4.14 High magnification view of 304 S/S.

4.2.3.5 101 Free-machining brass

The brass microstructure is presented in Figures 4.15 and 4.16.

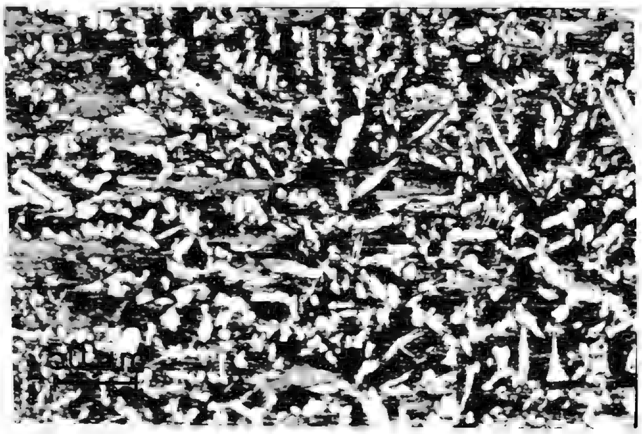

FIG : 4.15 101 free machining Brass hot rolled (ferric chloride).

An α/β brass, the α-phase (white grains) may be seen in a β-phase matrix (dark background) with the lead phase aligned in the rolling direction.

FIG : 4.16 As for Figure 4.15 - high magnification.

4.2.3.6 TMT Process 51

A section through the coated, high cobalt as-cast TMT sample is shown in Figure 4.17.

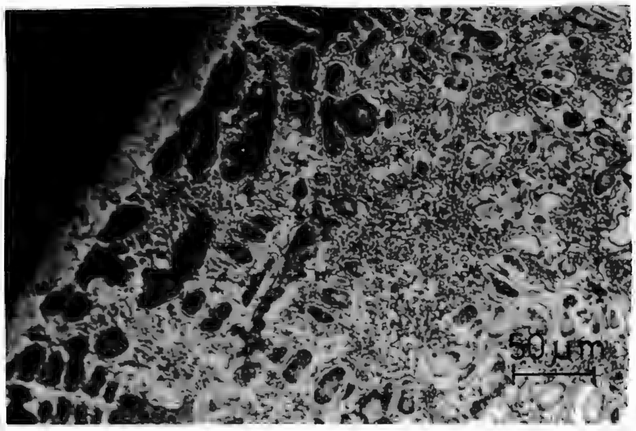

FIG : 4.17 As cast TMT sample showing diffusion coating (ferric chloride etchant).

The dendritic nature of the substrate may be noted and the coated layer (measured thickness 25 - 30 µm) is clearly visible.

4.2.3.7 KA2

The WC-Co grain size distribution in the 304L stainless steel and Cu/Fe alloy matrix of the Kennametal KA2 sample is shown in a low magnification SEM micrograph (Figure 4.18). The grain size is nominally 1,8 mm with an intergranular spacing of 2 mm.

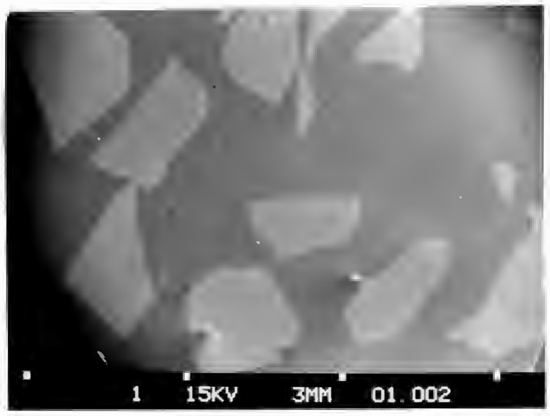

FIGURE 4.18 SEM micrograph of KA2 specimen prior to erosion.

4.3 TEMPERATURE

Calibration and initial testing was conducted at a room temperature of nominally 17°C. During the commissioning of the heating facility, limited testing was performed on the standard material at an intermediate temperature of 150°C while the final test temperature was 400°C. Between elevated temperature testing, regular room temperature verification tests were conducted to assess the continued reproducability of the facility.

4.4 GEOMETRY

Seat/cone angles of 30, 45 and 60 degrees were included in the test programme, with the option of a more detailed geometry test series remaining.

4.5 CALIBRATION

4.5.1 ASH LOADING

The ash loading times were noted during charging of the hopper between tests, and the loading rate calculated. Accepting errors resulting from variation in loading technique and the state of dust clogging of the vacuum filters which effect the efficiency of the unit, an average ash loading rate of 7,5 $kgmin^{-1}$ was recorded.

4.5.2 HEATING

A calibration plot of 'percentage heating time' versus power controller switch setting (Figure 3.19) is presented as Figure 4.19 in Appendix D. The curve is notably non-linear, with setting 5 resulting in a percentage heating time of less than half that of setting six.

A TOA model EPR 200A chart recorder was incorporated with the heater control unit during initial elevated temperature testing in order to assess the ash heating rate (inside thermocouple) and the effect of power controller setting on this rate. On commencement of heating at a particular controller setting, a relatively sharp initial temperature rise (I) was noted followed by a gradual approach to an equilibrium or steady state situation (II). An example of this effect is illustrated in Figure 4.20, Appendix D. By changing the controller setting from "3" to "4", the heating rate is altered, rising to the selected temperature and stabilizing (III).

4.6 TESTING

4.6.1 SPECIMEN PREPARATION

After machining, where necessary, machining marks were removed from the target surface of the specimen by grinding. Thereafter, specimen surfaces were polished on graded SiC papers to a finish at 500 grit SiC. Immediately prior to testing, the test specimen is cleaned in alcohol in an ultrasonic cleaner and dried. Finally the specimen mass is recorded to an accuracy of ± 0,2 mg. After testing, the specimen is again cleaned and weighed; specimens to undergo optical or scanning electron microscopy were stored in a dessicator.

4.6.2 TEST TIME

A standard test time of thirty seconds was decided on. This period was sufficient to result in measurable and reproducable erosive loss in the standard as well as the other basic materials. It became apparent however, that for the 'special' materials, insufficient specimen mass loss was recorded over this period. Results recorded suggested mass losses of less than 0,5 mg in cases, these measurements approaching the accuracy of the balance used. The problem was overcome by extending the test time to a maximum of sixty seconds and, where necessary, repeating the erosion test. A maximum test time of sixty seconds was stipulated due to two factors. While the problems of 'ash starvation' had largely been solved, the ash flow rate from an initial fixed ash mass system into which only high pressure air was introduced, would necessarily decrease with test time.

A test time of sixty seconds however maintained uniform ash flow rates. The second limiting factor was the useful protective life of the stainless steel gasket material. Exposure to ash flows for periods in excess of approximately sixty seconds resulted in perforation of the gasket and subsequent test cell erosion.

4.6.3 TEST PROCEDURE

Note : Valve designations in this section refer to Figure 3.21 section 3.5.3 unless otherwise referenced.

Assuming the hopper to be empty of ash and at room temperature, the stepwise procedure for conducting an erosion test is presented below :

1) Charge hopper with 16±0,5 kg erodent
   a) weigh out desired amount of dried ash,
   b) attach ash loading hoses to loading valves (a and b in Figure 3.14) and open valves,
   c) switch on vacuum unit and load.

2) Set temperature control and heat (refer to Figure 3.19).
   a) Adjust thermowell controller to required test temperature,
   b) set element temperature control to 500°C
   c) set power control to setting 3 (21,5 percent heating) and allow to stabilize overnight (approximately 10 hours)
   d) increase power control to setting 4 to equilibrate ash temperature at preset level.

3) Pressurize air receiver.

While pressurizing air receiver,

4) prepare sample for testing
   - a) clean ultrasonically
   - b) weigh

and 5) load test cell
   - a) insert and affix sample
   - b) adjust cone section (Figure 3.8) to give 1,5 mm gap size as measured by feeler guage
   - c) position gaskets and secure cover plates.

6) Pressurize hoppper
   - a) close loading ports (Figure 3.14)
   - b) commence pressurization by opening the fluidizing line shut-off valve (6) and adjusting the fluidizing ball valves (1) to allow controlled pressurization of hopper over approximately ten minutes.

While pressurizing,

7) Suspend ash trap
   - a) record initial suspended mass
   - b) lower and attach flexible ash feed hose to ash trap

8) Testing

   On pressure equilibration at the 2,5 MPa test pressure in the receiver and ash hopper,
   - a) record ash and hopper temperature ('inside' and 'outside' digital readout)

   - b) while continuing to fluidize open ash feed valve (2) for prescribed test time
   - c) shut feed valve (2)
   - d) close fluidizing ports (1) and line shut-off valve (6)
   - e) record ash and hopper temperature
   - f) open carrier line shut-off (5) briefly (±2 seconds) to clear test cell of residue ash.

9. Determine erodent mass
   - a) detach ash hose
   - b) suspend ash trap and record mass.

10. Depressurize hopper via ash loading valve (b in Figure 3.14).

11. Remove test specimen from cell, clean and weigh

12. Recharge hopper with mass of ash removed during previous test as in step 1.

13. Allow fresh ash to soak until test temperature is attained (± 30 minutes).

14. Continue as from step 3.

4.7 TEST PRECISION

4.7.1 ASH FLOW

Ash flow rates during testing measured in grams per second, for both 0,8 mm and 1,5 mm test cell gap sizes were recorded and are presented in Table 4.5 below.

TABLE : 4.5 Mean ash flow rates as a function of test cell gap size.

GAP SIZE (mm)	MEAN ASH FLOW RATE (gs^{-1})	% STANDARD DEVIATION
0,80	41,9	20,00
1,50	117,7	9,95

Flow rate variations have been noted in a similar gas blast test method (17). Reasons for the flow deviation from the mean value include such factors as erosion or the feed valve spindle, errors in test timing and in resultant ash masses. Errors in the post-test erodent masses would result from inaccuracies on weighing and interrupted ash flow from the hopper.

4.7.2 SPECIMEN VOLUME LOSS

The volume loss results of the specimens tested are the mean of a minimum four test to a maximum of fifteen representative tests as in the case of the test standard. One standard deviation from the mean of the tests conducted was typically within 10 percent for the higher volume loss materials, but the uncertainty increased for the materials with improved erosion performance as the specimen mass loss per test approached the accuracy of the balance employed.

The errors realised in the volume loss results may be ascribed to various factors. Variancies in ash flow, as noted in section 4.7.1, inconsistencies in size distribution of the erodent (section 4.1.1.2) and the dynamic geometry change of the test piece during testing, would all adversely affect the reproducability of results obtained. The specimen geometry change on erosion is illustrated schematically in Figure 4.21.

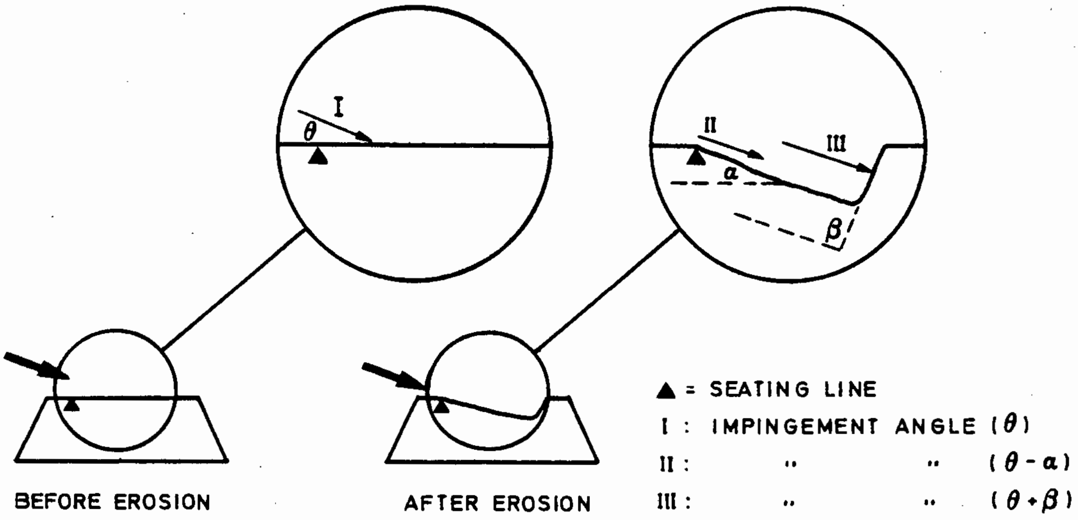

FIG : 4.21 The effect of surface profile change on ash impingment angle.

4.8 CALCULATION OF ASH FLOW CONCENTRATION

An approximation of the ash concentration through the test cell during testing was made in an attempt to assess the possible influence of particle interactions on erosion. As detailed in the test procedure, the compressor continues pumping for the duration of an erosion test. The free air delivery at the 2,5 MPa test pressure is quoted as 5,8 ls^{-1}. Furthermore, the pressure of the receiver/hopper system decreases by 0.15 MPa over a 30 second test period. Assuming these conditions, the concentration may be estimated as presented below :

approximate volume of the system, V = (volume of air receiver) + (volume of hopper)

P_o= initial hopper pressure at start of test (time = t_o)
P_{30} = final hopper pressure (after 30 second test)

By Boyles' law, the volume increase associated with the pressure reducation (p_o-P_{30}) on testing is 28,7 l nominally at 2,37 MPa.

To revert to 2,5 MPa, the approximate volume loss during testing is:

V = 27,2 litres at 2,5 MPa

The above value corresponds to a 30 second test, the rate of volume loss, therefore, is:

Air flow rate, Q $= 0{,}9\ \mathrm{ls}^{-1}$

The total air flow rate at 2,5 MPa, therefore is 6,7 ls^{-1}

This corresponds to a air volume flow of 201 l over the 30 second test time (at 2,5 MPa).

The mean ash flow rate recorded over the test series (section 4.7.1) was 120 gs^{-1} test time.

The ash concentration, C, in grams ash per litres air at 2,5 MPa over a test, may now be expressed :

$C = 1{,}8 \times 10^{-2}\ \mathrm{gcm}^{-3}$

4.9 PRESENTATION OF RESULTS

Controversy exists over the methods, and validity of therefore, presenting mass or volume loss data from erosion tests. Many authors (1,15,32,35 and 62) suggest a dimensionless erosion factor of the form milligram specimen loss per gram of erodent passed. This approach, however, assumes each erodent particle strikes the fracture surface and results in or contributes to erosive loss. This condition only occurs in macroscopic erosion (1) or in vacuum falling rigs as used by Bitter (35). Criticism of this approach is apparent from Smeltzer et al (6) who suggests extraneous results due to particle interactions and proposes an alternative approach of mass loss per particle. Tilly, in subsequent correspondence with Smelter, expresses doubt as to the usefulness of an erosion factor of this nature to engineers. A further approach is to assess materials purely on mass loss over a particular test period (48).

Based on Gulden's (65) analysis of particle concentration and the influence of aerodynamic effects on particle interations, together with discrepencies in ash flow rates during testing (discussed in Chapter 6), it was decided to express erosion performance of individual materials as a rate expression, mm^3s^{-1} of test time. For the purpose of materials ranking and comparision, the volume losses of the specimens were ranked relative to the 080M40 steel standard according to the expression:

Relative Erosion Resistance

$$\text{RER} = \frac{\text{Volume loss 080M40}}{\text{Volume loss specimen}}$$

RER values are taken over a standard 30 second test time, increasing RER infering improved erosion resistance.

CHAPTER FIVE

RESULTS

5.1 VALIDITY OF SIMULATED TESTS

5.1.1 FLOW PATTERNS

5.1.1.1 Macro

Having reproduced the geometry and physical conditions of pressure, erodent and temperature on the in-service valve in the laboratory, it remained to compare the erosion patterns of the two systems as a means of assessing the validity of the simulated condition. Examples of the ashlock valve seats are shown in Figures 5.1 and 5.2. Figure 5.1 shows the seat section prior to installation while Figure 5.2 illustrates the failed seat after erosion.

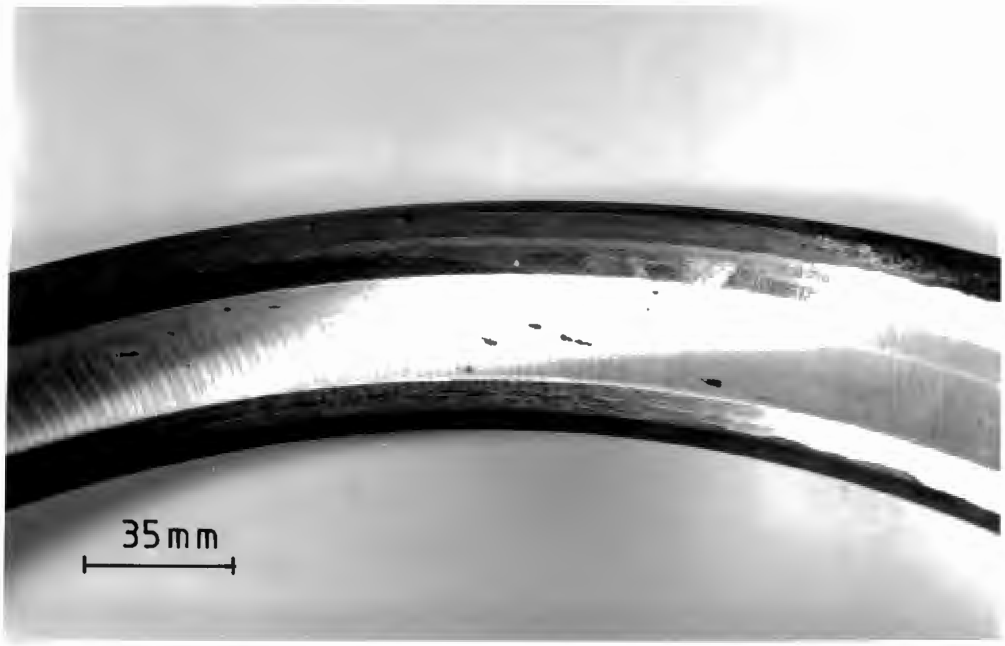

FIG : 5.1 Ashlock valve seat prior to erosion.

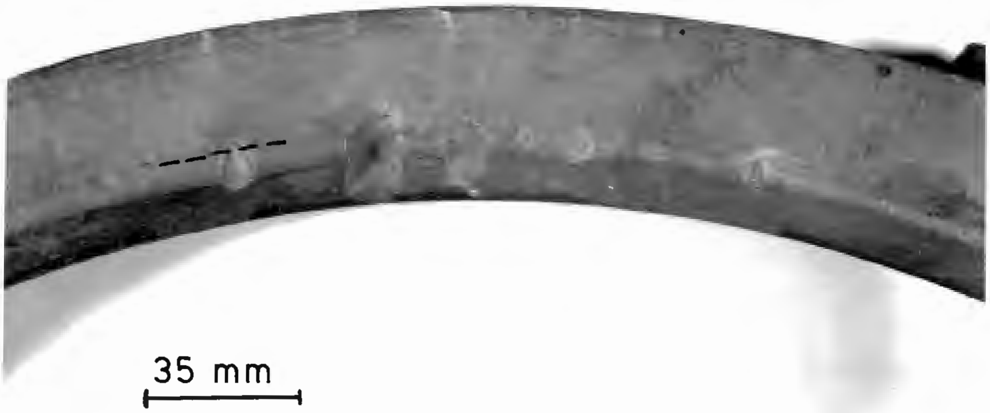

FIG : 5.2 Failed ashlock valve seat showing a range of erosion tube sizes. The broken line indicates the cone seating area.

Erosion damage on a macro-scale takes the form of 'erosion tubes' which initiate and grow progressively and uniformly larger with no apparent preference for lateral or radial growth. This effect is also known as the "wire-drawing effect" (17). It is evident from size consideration of the erosion tubes in Figure 5.2 that erosion sites continue to initiate and propogate randomly over the erosion susceptible surface despite the presence of established damage sites in the area. Representative samples of specimens eroded in the test facility are presented in Figure 5.3. The erosion patterns on the samples reflect the material loss after a standard 30 second test, the mass loss decreasing from Brass, 080M40 to Cobal 6.

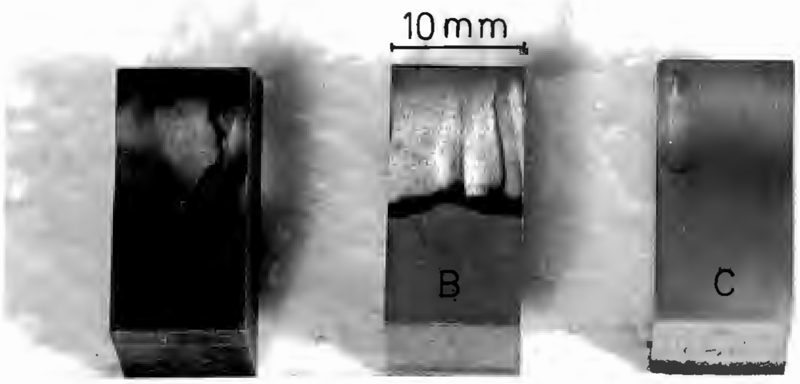

FIG : 5.3 Macro erosion patterns on 080M40 (A), Brass (B), and Cobal 6 (C), test specimens.

5.1.1.2 Erosion initiation

In a simulated tester, it is important that the erosion is initiated in the same area as on the in-service seat. The erosion 'initiation zone' maybe defined as the area from which down-stream erosion originates (Figure 5.4).

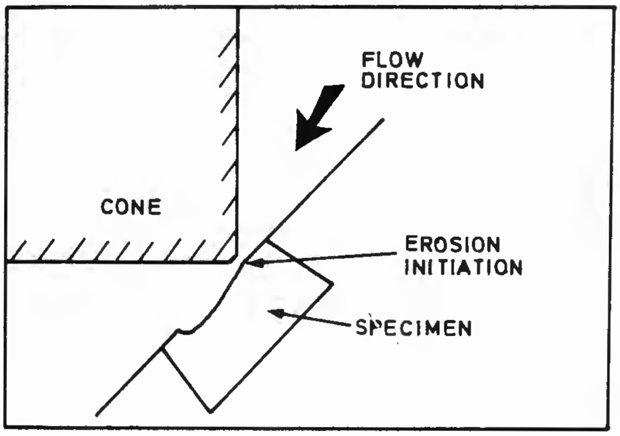

FIG : 5.4 Erosion initiation zone showing erosion down-stream of the valve throat.

The ash flow patterns within the test cell may clearly be noted by the preferential etching by the ash of the stainless steel gaskets in Figure 5.5.

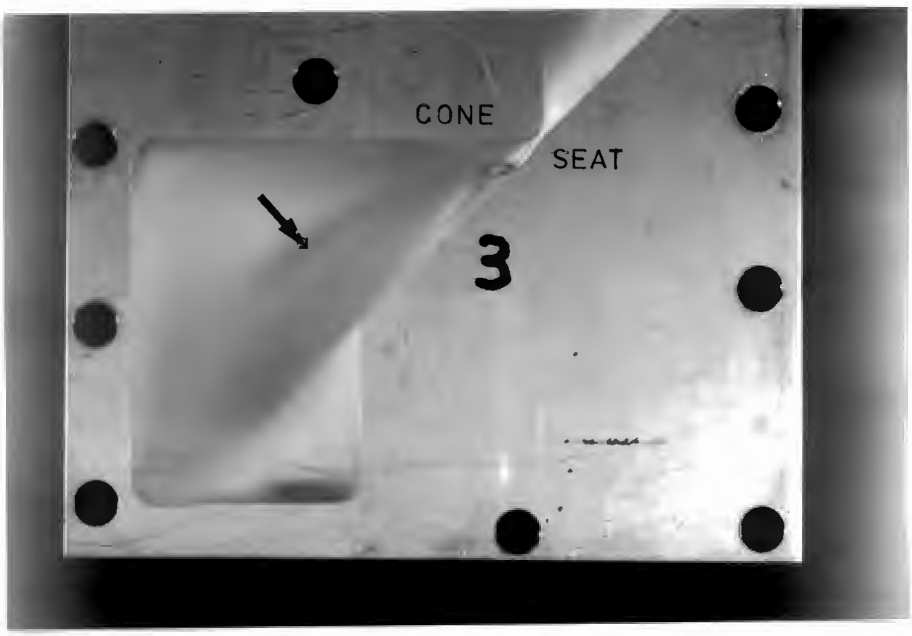

FIG : 5.5 Preferential etching of the stainless steel gasket showing ash flow pattern.

Figure 5.5 represents a cross-section through a failed valve and clearly shows the erosion to initiate at the seat/cone 'contact' point and to propogate downstream of the initiation zone.

It is evident that in both the in-service and test cases, the erosion initiation zone corresponds to the valve seat/cone contact line, and erosion is only evident downstream of this region.

5.1.1.3 Micro

The appearance of the eroded specimen surface was found to vary considerably as a function of viewing area. This is illustrated in Figure 5.6 in which the surface damage acruing from the 'base', 'face' and 'top' areas are presented.

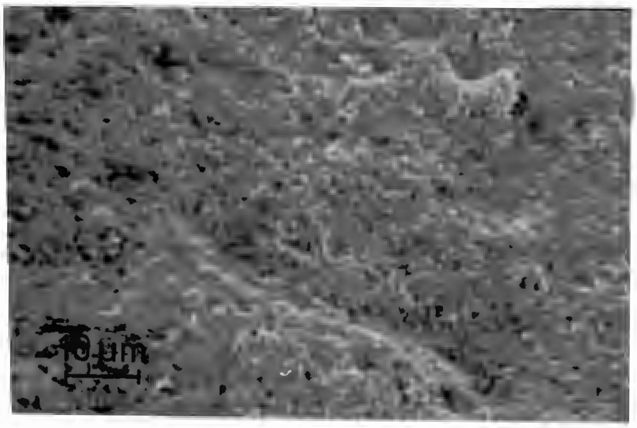

Face

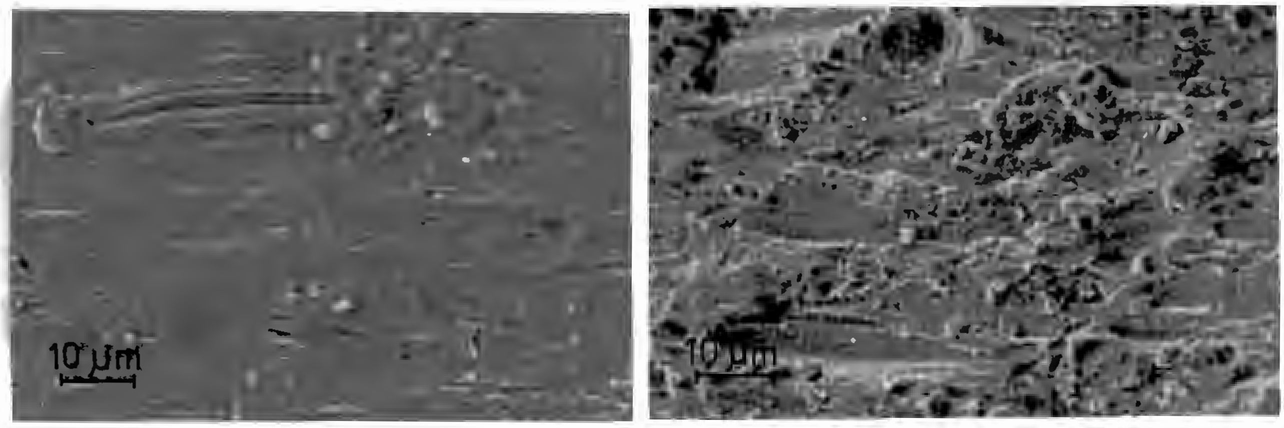

Top

Base

FIG : 5.6 Erosion profile illustrating the differing surface damage regimes of brass under standard conditions.

The heavily deformed base area with apparent long multiple strike damage gives way to the essentially normally impacted 'cliff' or 'face' region. This area has the appearance of a cavitation damaged surface with no individual strikes evident, while the top section shows isolated and very long strikes on a less deformed surface.

Noting the differences in surface features with viewing area, SEM examination of both as received failed seat samples and Cobal 6 test specimens was conducted on the base regions of the specimens. Micrographs comparing the erosion surfaces are presented in Figures 5.7 and 5.8.

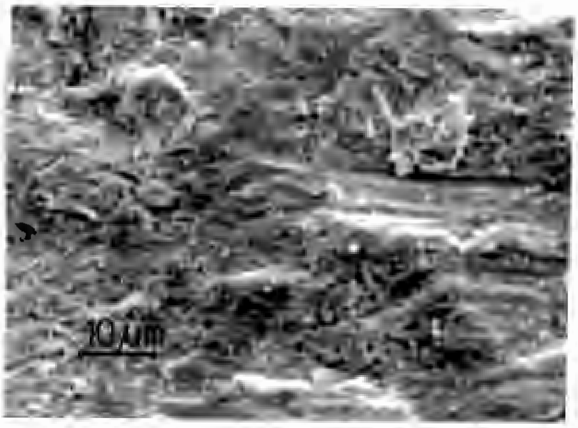

FIG : 5.7

FIG : 5.8

FIG : 5.7 SEM micrograph of eroded in-situ Cobal 6 seat
and
FIG : 5.8 SEM micrograph of eroded Cobal 6 test specimen.

The similarities in shape and size of erosion strikes suggest the selected erodent fraction for laboratory testing to be representative of that resulting in full-scale valve failures.

5.2 MATERIALS PERFORMANCE

5.2.1 CUMULATIVE LOSS

Cumulative volume loss tests were noted for both 080M40 and TMT coating (process 51) in the as-received condition at room temperature. The representative volume loss versus test time plots are presented in Figure 5.9. It is noted that for the 080M40 standard a non-linear trace was obtained.

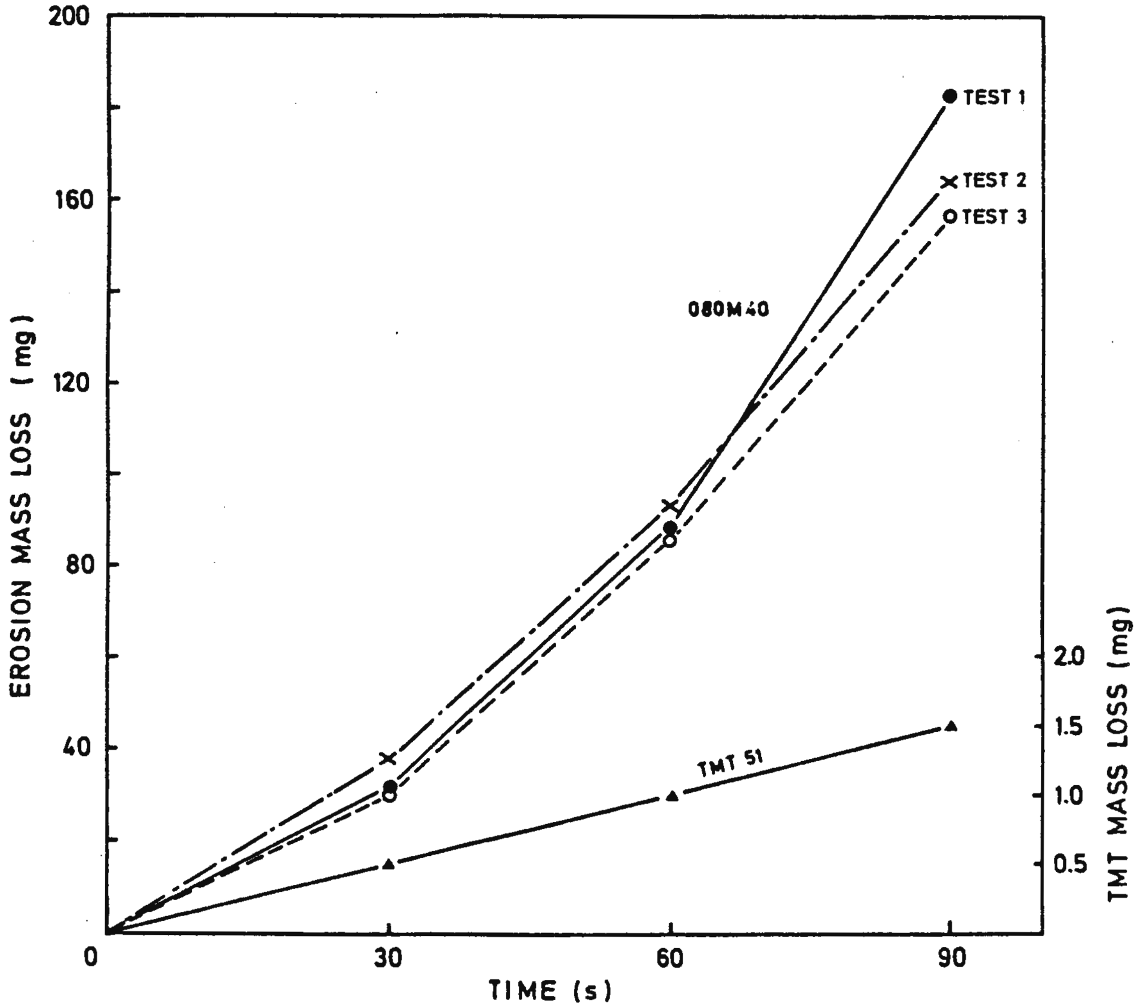

FIG : 5.9 Cumulative mass loss (mg) for 080M40 and TMT 51 samples.

Volume loss versus time plots for the more erosion resistant materials such as TMT (process 51) showed a more linear volume loss rate profile, suggesting the cause of the non-linearly in the softer material to be the changing surface profile and the resultant increased strike area for eroding particles. The discrepancies between the mass losses recorded for the 080M40 cumulative tests are an indication of the reproducability or error in the system.

5.2.2 STANDARD TESTING

The erosion performace of materials tested for 30 seconds at room temperature and at seat/cone test angle of 45° is shown in Table 5.1.

TABLE 5.1 Sample materials performance under standard test conditions.

Material	Mass loss (mg)	Volume loss (cm^3)	RER*
TMT 51	0,5(3)[1]	0,06(4)	66
Cobal 6	20,5	2,56	1,61
KA2	30,7	2,91	1,42
080M40 (A)	32,3	4,13	1,00
304	41,8	5,20	0,79
Brass	432,8	51,71	0,08

* Relative Erosion Resistance.
All RER values quoted are based on the performance of 080M40 in the as-received condition; 45°; 30 second room temperature test.

[1] Mean Mass loss : mass loss per test approaching accuracy of balance.

A general surface damage comparison of selected materials tested at 45° and at room temperature is shown. While the effect on damage appearance in different sections of the test piece is noted, the subsequent micrographs typically reflect the 'base' region of specimens tested.

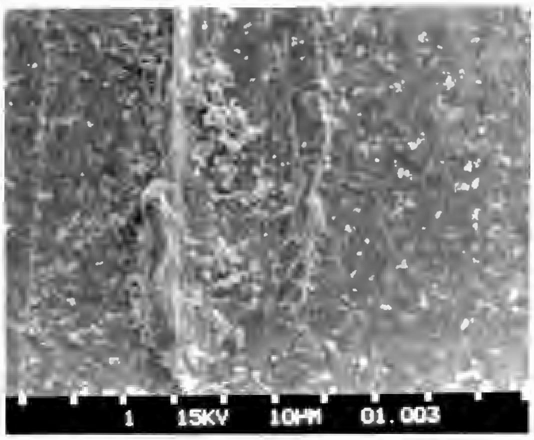

FIG : 5.10 Erosion strike on 080M40 surface resulting in the formation of a raised lip.

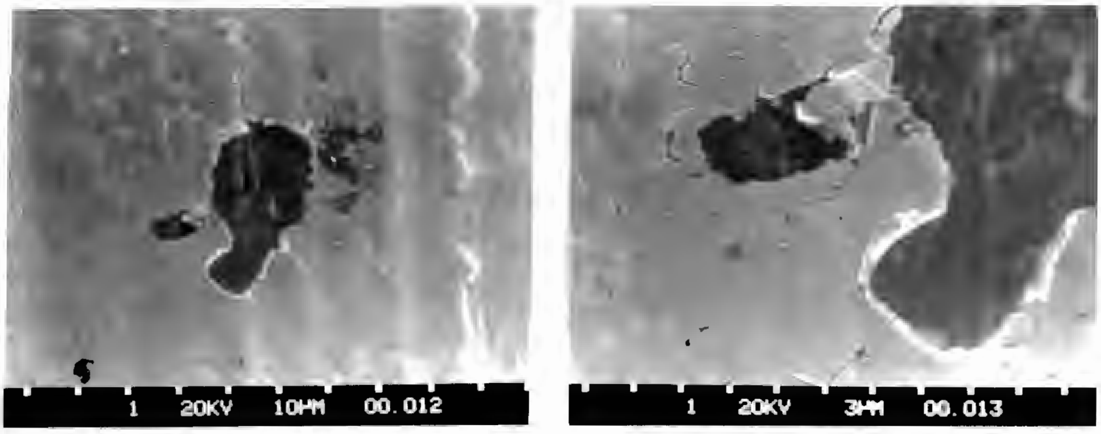

(a) (b)

FIG : 5.11a and b Brittle behaviour of diffusion coated TMT specimen showing general cracking with limited evidence of delamination.

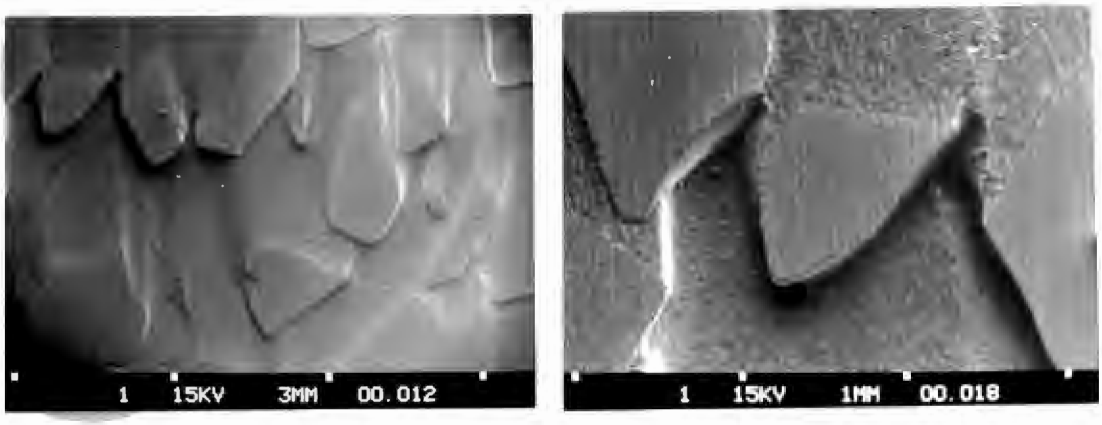

(a) (b)

FIG : 5.12a and b Preferential leaching of binder phase in erosive attack on KA2 specimens.

The contrast between the erosion mechanisms are evident in that the 080M40 loses material by cutting or ploughing as well as subsequent formation and loss of deformation lips (Figure 5.10), while the delamination of the TMT (process 51) specimen is apparent. The third condition, sample KA2 as shown in Figures 5.12a and b, reveals the 304 s/s matrix material to be preferentially leached from between the essentially unaffected tungsten carbide grains.

5.3 EFFECT OF HEAT TREATMENTS

Standard room temperature tests performed on the range of heat treated 080M40 specimens revealed negligible differences in erosion behaviour of the samples. It should be noted that the oil quenched material (Q), with a 2,5 fold hardness increase over the as-received standard, realized a marginally increased relative erosion volume loss. The results are listed in Table 5.2 below, and are presented graphically in Figure 5.13.

TABLE 5.2 Erosion performance of heat treated samples under standard test conditions.

Material Condition	VPN 30	Mass loss (mg)	Volume loss (cm^3)	RER
A - as received	215	32,3	4,13	1,00
Q - oil quench	564	33,75	4,33	0,95
T - oil quench and temper 200°	476	32,9	4,23	0,98
TA - oil quench and temper 400°	397	33,6	4,32	0,96
TT - oil quench and temper 600°	308	33,2	4,26	0,97

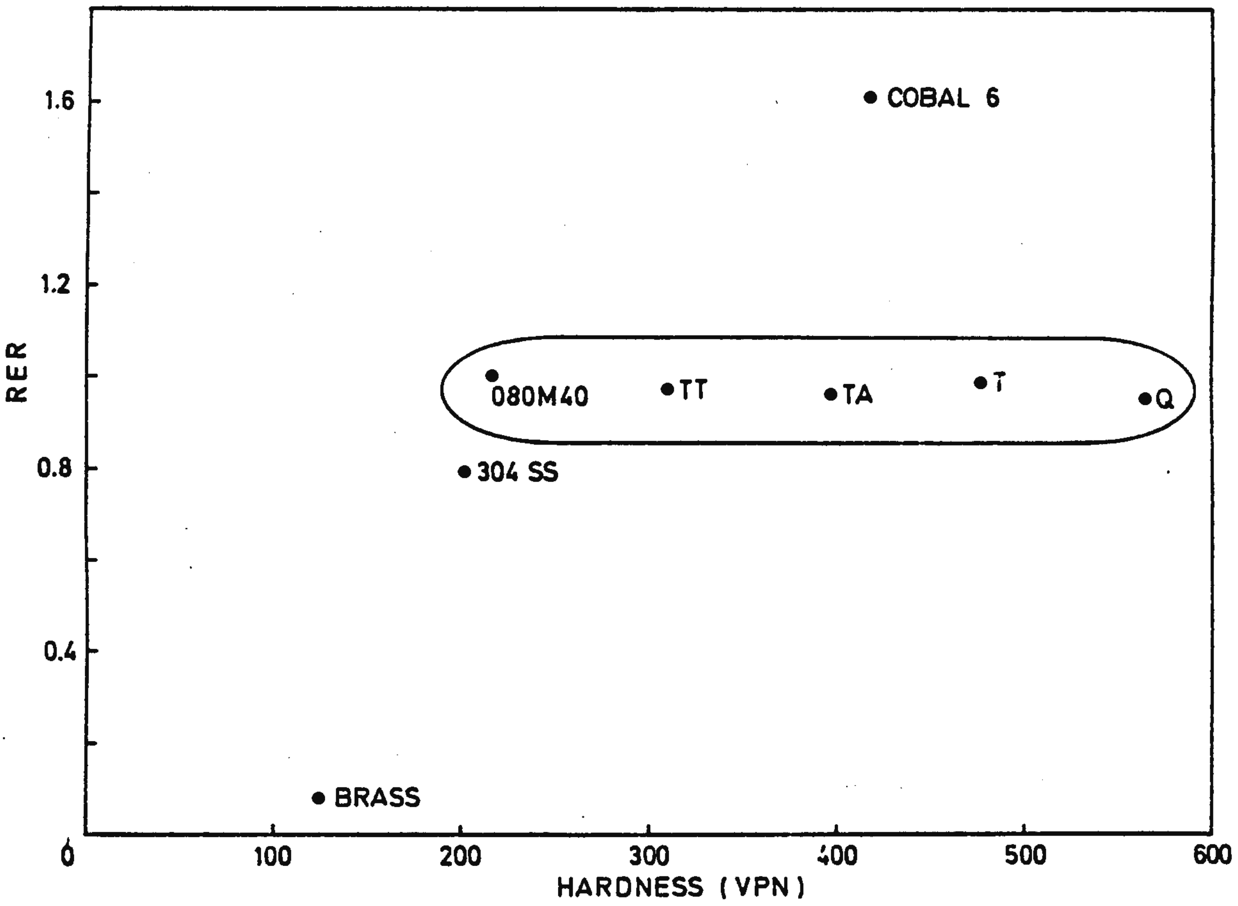

FIG : 5.13 Relative erosion resistance of test materials as a function of bulk hardness

Figure 5.14 of 080M40 oil quenched and tempered from 820°C shows a similar degree of plastic deformation to the 080M40 as received specimen (Figure 5.15) despite a considerable hardness increase (476 VPN vs. 215 VPN).

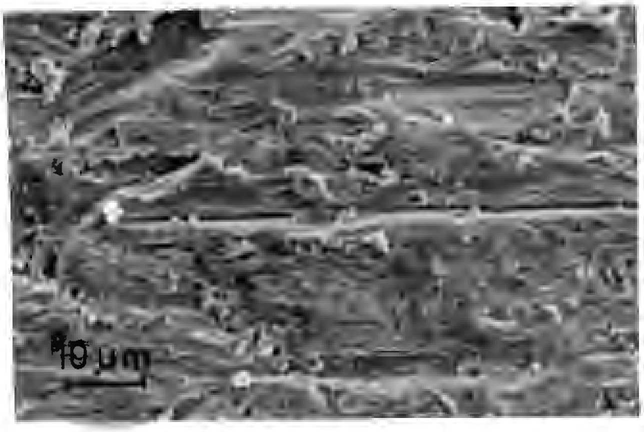

FIG : 5.14

FIG : 5.15

FIG : 5.14 080M40 oil quenched from 820°C showing similar surface damage to the as received specimen (Figure 5.15).

5.4 SUBSURFACE DAMAGE

In an attempt to assess possible subsurface effects resulting from particle impingement an annealed 304 stainless steel specimen was sectioned through the erosion surface, polished and etched. Figure 5.16 clearly shows slip lines extending to a depth of approximately 135 μm, with evidence of a 30 μm recrystallized layer on the surface.

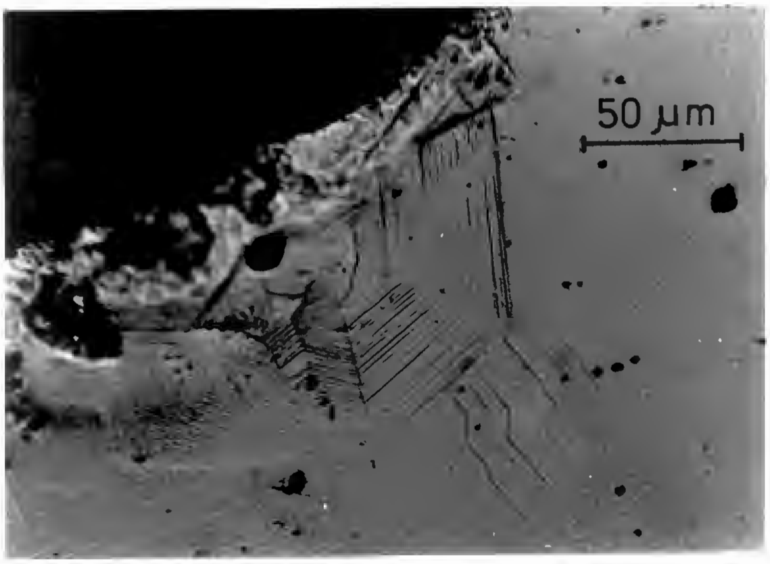

FIG : 5.16 Subsurface damage in 304 S/S specimen caused by erodent impingement in the base/cliff-face region.

5.5 TEMPERATURE

Elevated temperature testing was initially conducted at 150°C and at 400°C on the standard material to ascertain mass (volume) loss variations as compared to room temperature testing. A decrease in erosion with increasing temperature was noted, as is portrayed in Figure 5.17 showing 080M40 mass loss (mg) versus test temperature (°C as measured by the "inside" thermocouple. This thermocouple, positioned in the ash records the ash temperature in the middle of the hopper.

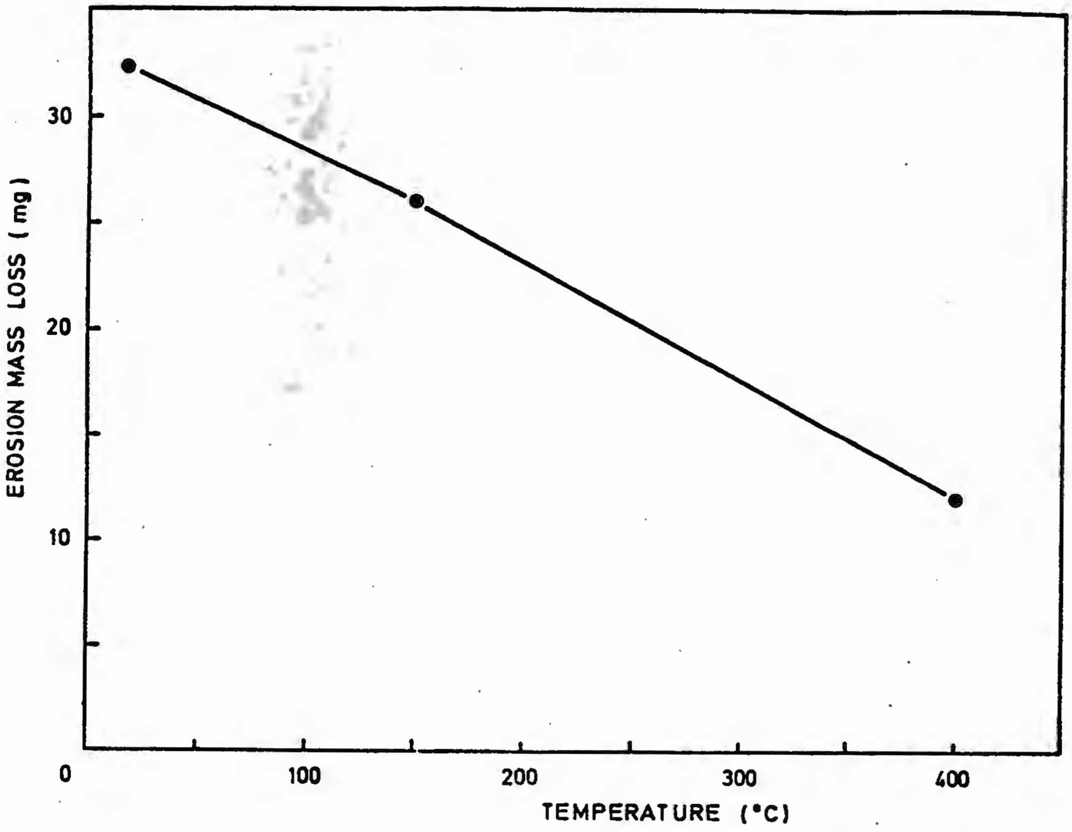

FIG : 5.17 Erosion mass loss of 080M40 versus test temperature in degrees Celsius.

A similar erosion trend was found on selected materials testing at 400°C. Figure 5.18 clearly indicates an increase in relative erosion resistance (decrease in erosion) with increased temperature.

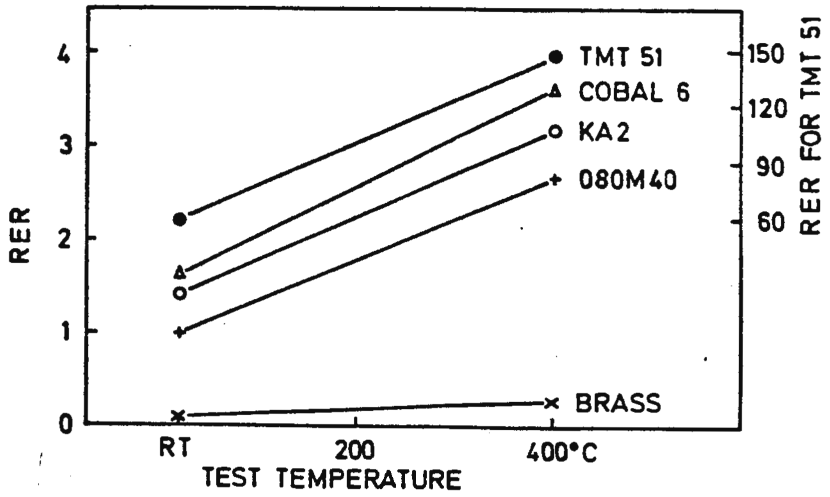

FIG : 5.18 Relative erosion resistance versus test temperature for selected materials based on performance of 080M40 at room temperature.

All the materials tested, except brass, exhibit a similar magnitude of increased erosion resistance with temperature, while registering a decrease in erosion. It can be seen that the improvement of brass with temperature is less marked when compared to the other materials. The high relative performance of the TMT specimen necessitated a separate RER scale as included in Figure 5.18 above.

An example of the erosion surface of the 080M40 standard specimen tested at 400°C and at 45° seat/cone angle is presented in Figure 5.19. While a range of erosion strike sizes can be noted, no evidence of melting or softening in the form of rounded lips or droplets of metal can be seen.

FIG : 5.19 Extensive strike damage on 080M40 surface tested at 400°C in the as received condition.

5.6 GEOMETRY CHANGES

5.6.1 VOLUME LOSS

The results of room temperature testing of 080M40, Cobal 6 and 101 Brass at seat/cone angles of 30°, 45°, and 60° are presented in this section.

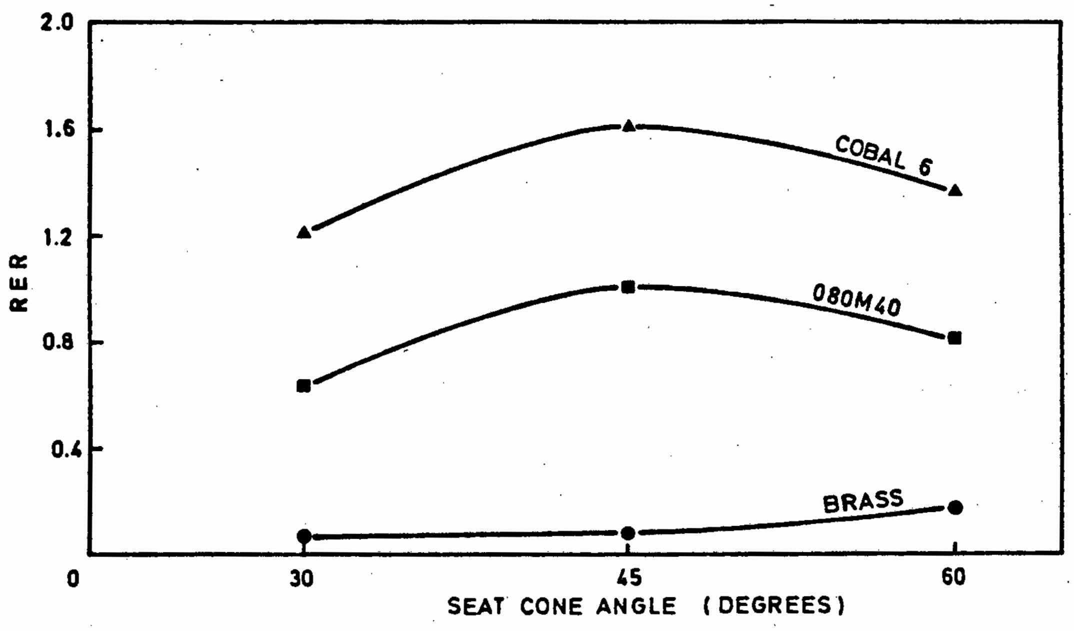

FIG : 5.20 Relative erosion resistance versus seat/cone angle in degrees for Cobal 6, 080M40 and Brass.

Figure 5.20 reveals increased erosion for the 080M40 and Cobal 6 samples at both 30° and 60° angles over the standard 45° geometry, while in the case of 101 Brass maximum erosion resistance is evident at 60°, with negligible RER variation between 30 and 45 degrees. Mass and volume loss data is presented in Table 5.3 overleaf.

TABLE 5.3 : Effect of seat/cone geometry change on room temperature erosion performance of 080M40, Cobal 6 and Brass.

	Material	Mean Loss (mg)	Volume loss (cm^3)	RER*
30°	080M40	51,4	6,58	0,63
	Cobal 6	27,7	3,45	1,20
	101 Brass	493,8	59,00	0,07
45°	080M40	32,3	4,13	1,00
	Cobal 6	20,5	2,56	1,61
	101 Brass	432,8	51,71	0,08
60°	080M40	39,8	5,09	0,81
	Cobal 6	25,1	3,13	1,35
	101 Brass	198,9	23,76	0,17

(* RER Values based on 080M40 at R.T. and 45°)

5.6.2 EROSION PROFILE

The surface profiles of the specimens after erosion were noted and an attempt was made to quantify the resultant erosion geometry acruing from the seat/cone angle change in terms of an **erosion profile ratio.**

Figure 5.21(a,b,c) schematically illustrates the specimen surface deformation caused by altering the seat/cone inlet geometry. The profile typically changes from a long, shallow erosion trace at 30°, through an "intermediate" crater at 45°, to a relatively short and deep crater at 60°. This result appears consistent with the estimated maximum erodent impingement angle as portrayed by the directional arrows in Figure 5.21.

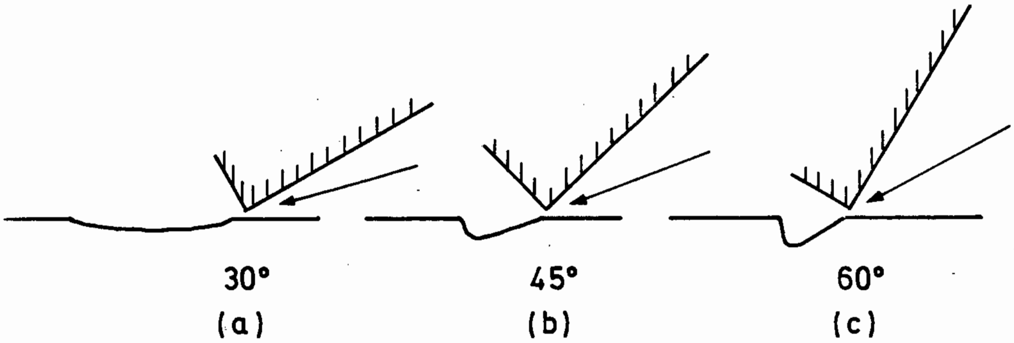

FIG : 5.21 Changing erosion profiles as a function of seat/cone angle.

The enhanced erosion of 101 Brass rendered it possible to assess the surface profile as a function of depth and length of erosion crater. The erosion profile ratio (EPR), the ratio of crater depth (d) to length (l) is illustrated in Figure 5.22.

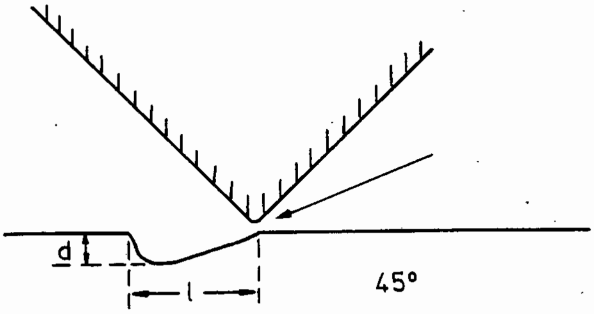

FIG 5.22 : Erosion profile quantified by depth (d) and length (l) of crater.

Typical Erosion Profile Ratio values for Brass are presented in Table 5.4, although similar results are noted for 080M40 and Cobal 6.

TABLE : 5.4 Erosion profile ratio for 101 Brass at varying inlet angles.

Seat/cone angle	depth (d)	length (l)	EPR
30°	1,0	14,0	0,071
45°	1,5	12,0	0,125
60°	1,4	7,5	0,187

Consideration of Figure 5.20 suggests a compromise is needed between the long, shallow erosion surface of the 30° geometry and the short, deeper erodent attack at 60° for optimum erosion resistance of 080M40 and Cobal 6. However, the improved erosion performance of Brass at 60° suggests a materials dependence in angle testing.

CHAPTER SIX

DISCUSSION

6.1 DISCUSSION OF RESULTS

There are three criteria which assess the validity of an apparatus which has been designed to simulate in-site conditions. On a macro scale, the topography of erosion should be similar while SEM micro analysis of the test and service specimen surfaces should be compatable. Finally, the materials ranking in the field should be reproduced in the test rig. These criteria have largely been satisfied in this study. It would appear from a sample of the failed seat as shown in Figure 5.2, that the erosion is initiated randomly over the affected area with both 'large' and 'small' erosion tubes in evidence. The contoured surfaces of the test specimens in Figure 5.3 similarly indicate erosion tubes at an early stage of development. A further feature of both the test pieces and the gasket traces, (Figure 5.5) is the clear erosion initiation point which is also observed in the full scale seat. These results may be interpreted in terms of gas/particle velocities experienced at the throat area, where it is clear that the flow speed increases considerably on passing the seating line. As a result, although the actual velocities are unknown, it may be assumed that a velocity analysis as presented in Appendix A, would be a reasonable interpretation of the situation.

While this evidence supports the validity of the rig, topographical investigation of the eroded surfaces by SEM, shows that the surface features closely resemble those seen on the 'real' gasifier cone. The surface of the Cobal 6 laboratory test piece and the full-scale seat are similar. It follows from this comparision that the particles responsible for the initial stages of the seat erosion at least, are in the range as used in the test series. Having satisfied the validity of the test rig, the final question of materials ranking has shown to be the same.

Standard room temperature testing provided various notable results. A general improvement in erosion resistance for materials with increased bulk hardness was obtained, but there are outstanding features. The apparent excellent performance of TMT (process 51) is due to the improved erosion resistance of the diffusion coating. However, as is shown in Figures 5.11a and b, the coating is removed by a delamination mechanism after prolonged exposure to erosion, and doubts as to the long term performance, integrity and reliability of the system may be raised. Furthermore, the impact loading of the in-situ value during operation (not simulated in the test facility) may detrimentally affect the coating life.

The trend of improved erosion resistance with hardness breaks down most notably in the erosion of heat treated steels. The various heat treatments of 080M40 clearly provide little change in RER despite considerable hardness increases. Thus hardness is not the sole or major criterion in defining erosion resistance. Reasons for this behaviour are unclear. The various theories proposed to explain this effect, as well as the effects of temperature on erosion, give insight into possible mechanisms of material removal. Heat treatments do not change the elastic Moduli of the steels, which could suggest that this property is important in erosion resistance. The mechanical properties of steels are highly strain and strain rate dependent. The extremely severe strains and high strain rates experienced during erosion would eliminate any property variation resulting from prior heat treatments.

The thermal properties of materials may also influence erosion if an adiabatic shear mechanism occurs. This would exist if the material being eroded cannot dissipate the frictionally generated energy caused by localised heating during particle impact. If, the energy can be effectively dispersed from the strike area by enhanced thermal conductivity or a high heat capacity, the extent of the erosion by adiabatic shear removal would decrease.

The suggestion that heat is generated by an erosion strike leads the discussion to the possibility of recrystallization of the surface layers. This proposal may also explain the lack of microstructural effects in steel erosion. Figure 5.16, shows considerable subsurface damage and a possible associated recrystallized layer in 304 stainless steel. Carbon steels could similarly austenitize due to strike heating and then transform locally to martensite. This situation could render all the heat treatments equal as regards erosion performance after brief exposure to impacting particles.

Tests conducted at elevated temperatures clearly showed a decrease in material loss with increased test temperature. This result is interesting when viewed in the light of proposed material removal mechanisms. The increased temperature could result in an increased specimen plasticity or ductility and allow greater energy absorbance. Mechanisms suggesting that removal is solely due to plastic flow, however, would be invalid as this would imply enhanced erosion at elevated temperatures. With regard to a adiabatic shear mechanism, thermal conductivity would decrease with increasing temperature. Thus there would be relatively less heat dissipation from the strike affected area. If the loss mechanism were adiabatic shear, this situation would stimulate this removal mode and increase the loss. However, the recorded results show this is not the case, thus indicating adiabatic shear is not the prevelant mechanism. Support for recrystallization and the associated platelet mechanism (54,61,62) of removal is shown here. With the specimen at elevated temperatures from commencement of erosion, a greater possibility exists for the material to reach recrystallization temperature and undergo a continuous tempering process of the previously worked lower surface regions. Futhermore, assuming that a critical strain has to be attained for metal loss (71), the elevated temperature would continuously remove residual strain and thus improve resistance in this case.

It is conventional in theoretical studies to measure erosion as a function of the impingement angle. By altering the seat/cone angles in the test cell, the changes in the full scale valve were represented. However, it has been noted that the seat/cone angles tested in this work are not directly compatable to conventional impingement angles, but are rather restricted by the practical limitations of service and thus may be of less academic significance. Nevertheless, the results obtained due to differing geometries are interesting. Cobal 6 and 080M40 both show maximum material loss at 30° with an optimum at the standard geometry of 45°. In both cases, the broader inlet angle of 60° again tends to increase the volume loss. Brass, on the other hand, behaves in a more 'traditional' manner in that the erosive loss decreases as the inlet or impingement angle increases from 30° to 60°. This behaviour is most readily accounted for in Figure 2.4 from which we see the ductile brass to be most susceptible to erosion at low impingement angles. The possibility exists that Cobal 6 and 080M40 are of an intermediate ductility or brittleness that would serve to modify the extreme curves portrayed in Figure 2.4 and account for their performance. An important consideration, however, apart from the inherent range of impingement angles with this test method, is the dynamic geometry change during erosion.

It is clearly shown (Figure 4.21) that no specific erosion direction may be isolated as the primary erosion component. The results of the geometry changes should therefore be approached in terms of benefit to sealing or altering flow patterns across the full-scale valve, rather than as significant to theoretical research.

As the aim of the project is ultimately to assess the most favourable erosion resistant material in conjunction with valve design, the best performer under the specific conditions needs to be established. The limited impact resistance of thin coatings has been noted, and thus it would appear that considerable advantage may be gained from tungsten carbide systems. From the sample tested, it is clear that the matrix material is the limiting factor for erosion resistance. Preferential leaching of the binder phase in carbide systems indicates that material design should be approached in terms of carbide grain size, intergranular spacing and alternative binder phases. While both temperature and geometry have been shown to effect material performance, limited scope for change exists in the way of on-site operating conditions.

6.2 DESIGN

It was noted in Chapter 3 that certain 'unknowns' in the operation of the proposed test rig made design and the prediction of performance difficult. The facility, as constructed, has been shown to operate satisfactorily due largely to the considerable modifications of the prototype. This section therefore suggests a possible 're-design' in hindsight, noting the problems encountered.

The gas blast principle was sound and any redesign should be based on this method. Considering the problem areas, the non-uniformity of particle size distribution caused inconsistencies. Apart from causing errors in results, the varying size distribution caused considerable changes in the ash flow. In the test rig as fabricated, the primary problem areas were ash flow and ash heating, these being indirectly aggravated by the large physical size of the apparatus. The remaining features such as ash loading, test cell and ash removal operated as envisaged and could be retained. Of these components, the test cell is the most important being the heart of the simulation and must therefore be unchanged, having successfully reproduced the in-situ results.

A redesign to allieviate the problem areas of ash feed (flow) and heating is shown schematically in Figure 6.1. Conceptually the modification would introduce a fixed aliquot of hot ash into a heated carrier stream. The duration of the test would be determined by the size of the ash aliquot. The feed mechanism would be a soft iron piston or plunger, magnetically operated, which would push the erodent from the cylindrical 'hopper' into the air stream at a constant rate.

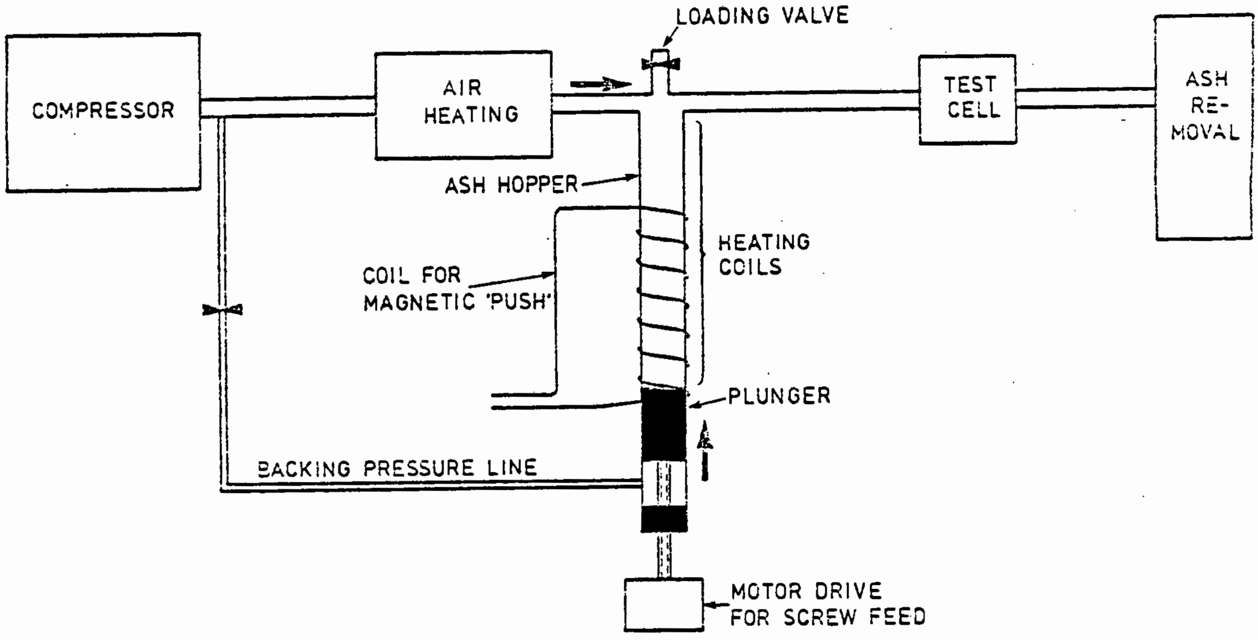

FIGURE 6.1 Schematic representation of theoretical test rig 're-design' showing both magnetic and screw feeds

An alternative to the magnetically operated plunger could be a mechanical feed through a high pressure seal at the cylinder base as shown in Figure 6.1. Based on data from the present apparatus, a hopper capacity of approximately four kilograms would be sufficient to generate measureable specimen mass loss. Loading could be effected by means of a gate valve positioned above the erodent hopper.

The problems associated with heating a gas containing entrained ash, would be avoided by preheating the carrier stream by means of propane burners. The ash would be heated to test temperature by winding heating coils around the hopper and allowing to soak. Care should be taken in this respect to ensure that the hopper bore does not exceed approximately 100 mm due to the previously noted poor heat conductivity of the ash. This method of heating would also reduce localized 'hot spots' on the elements, as well as facilitate replacement of blown elements which posed considerable difficulties in the past.

The heated carrier gas would entrain the erodent on passing the mouth of the hopper, while the concentration could be accurately controlled by movement of the plunger.

Finally, in dimensioning the modified components, size would be kept to a minimum to facilitate operation.

APPENDIX A

Calculations

i) Flow velocity a) $M = 1$ at exit (eg. hole in reservoir, non-converging/diverging nozzle)

M = Mach number

P_r = Receiver pressure (MPa)

P = Atmospheric pressure (MPa)

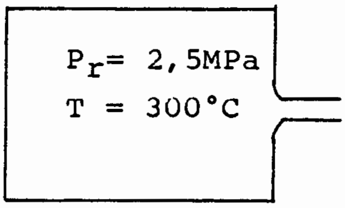

From isentropic flow tables:

$$\frac{P}{P_r} = 0{,}528 \text{ for choked flow } (M = 1 \text{ at exit})$$

$$\text{in this case } \frac{P}{P_r} = \frac{0{,}1}{2{,}5}$$

$$= 0{,}04$$

Therefore comparing 1 and 2, there is sufficient pressure to cause choking and the nozzle is overexpanded.

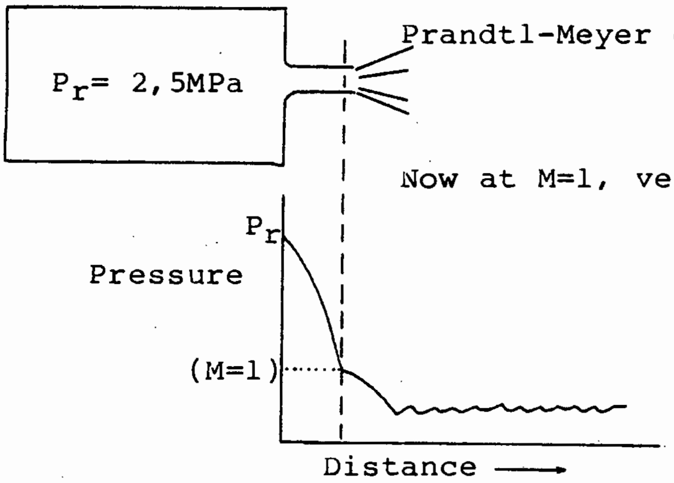

Now at $M=1$, velocity = a (speed of sound)

and $a = \sqrt{\gamma R T_{abs}}$

$= 520 \text{ ms}^{-1}$

APPENDIX B

Venturi

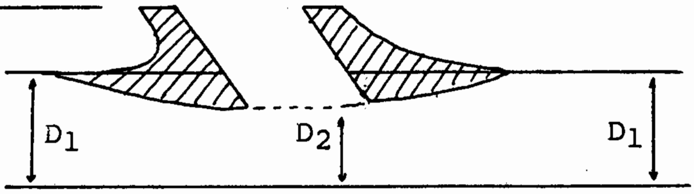

from isentropic flow tables

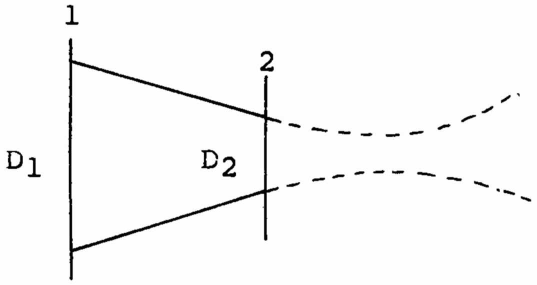

Assume $D_1 = 18,85$ mm

$D_2 = 7,5$ mm

find P_2

(referring to isentropic tables and gas dynamics theory)

$$\frac{A_1}{A_2} = 6,25$$

$M_1 = 0,0353$ (M = V/a = 12/340)

$P_1 = 2,5$ MPa

From tables @ M = 0,0353

$$\frac{A_1}{A^*} = 16,891 \qquad \frac{P_1}{P_r} = 0,9992$$

$$\frac{A_2}{A^*} = \frac{A_2}{A_1} \cdot \frac{A_1}{A^*}$$

$$= \frac{16,891}{6,25}$$

$$\frac{A_2}{A^*} = 2,7026$$

from tables @ $A/A^* = 2,7026$

$M = 0,22$ approx. and $P_2/P_r = 0,9668$
($V = 75\text{ms}^{-1}$)

$$\text{Now } P_2 = \frac{P_2}{P_r} \cdot \frac{P_r}{P_1} \cdot P_1$$

$$= 0,9668\ (1/0,992)\ .\ 2,5$$

$$P_2 = 2,44$$

thus pressure differential $= P_1 - P_2 = 8,7$ psi

APPENDIX C

Tube wall thickness for 4,0 MPa maximum working pressure.

(using thin cylinder theory)

$\sigma H = pd/2t$

$\sigma L = pd/4t$

p is the pressure (MPa)
d is the diameter (m)
t is the wall thickness (m)
σH is the hoop stress
σL is the longitudinal stress

$$H = \frac{4{,}0 \times 10^{6}\ (25 \times 10^{-3})}{2t}$$

Let maximum σH be 150 MPa (stress for 1% elongation in 10 000 hours @ 540°C)

$t = 0{,}3$ mm

thus seamless grade 316L stainless steel 25mm O.D. x 1,65mm wall would be adequate for the application.

APPENDIX D

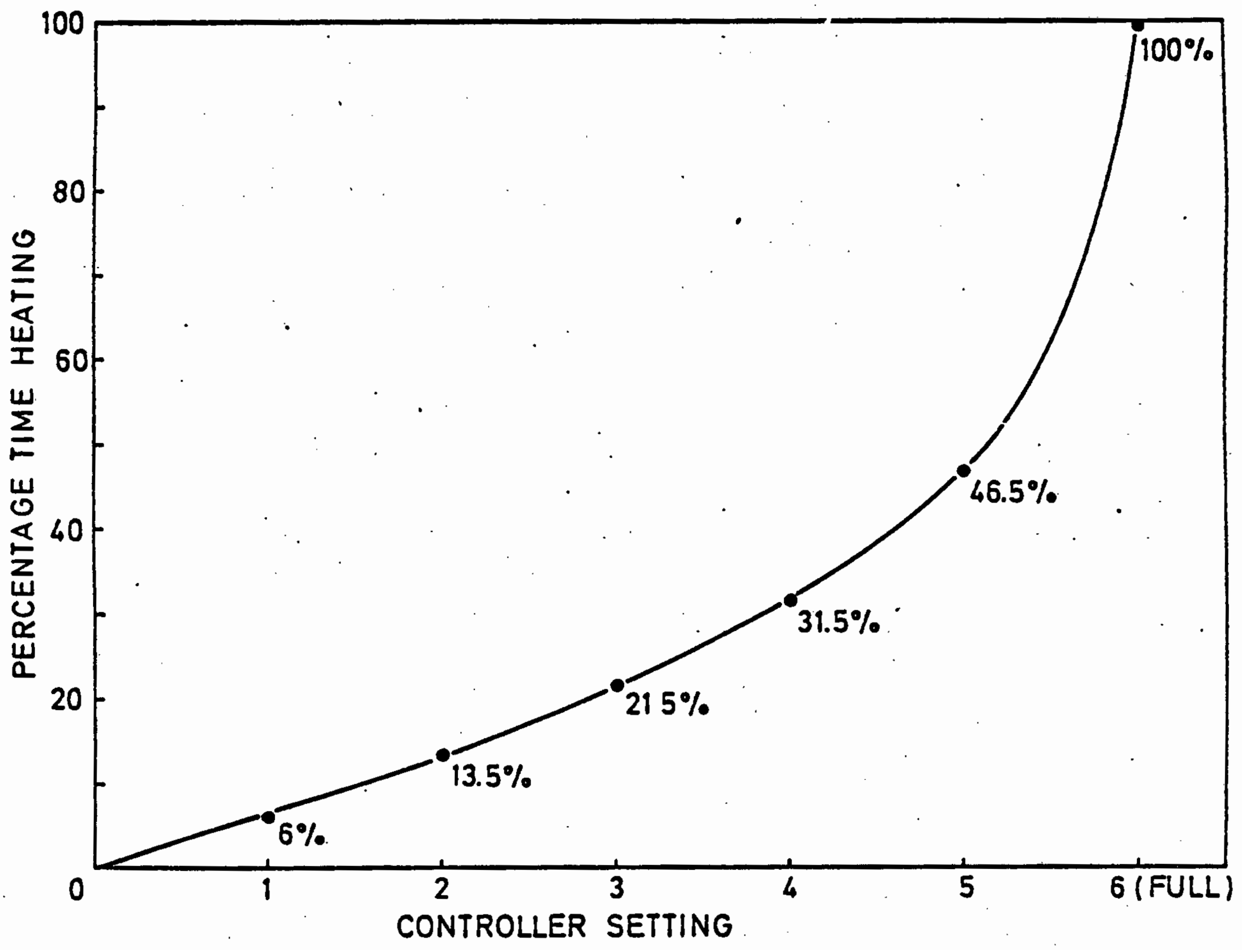

FIG : 4.19 Plot of 'percentage heating time' versus 'power controller setting' (Section 4.5.2).

APPENDIX D (cont)

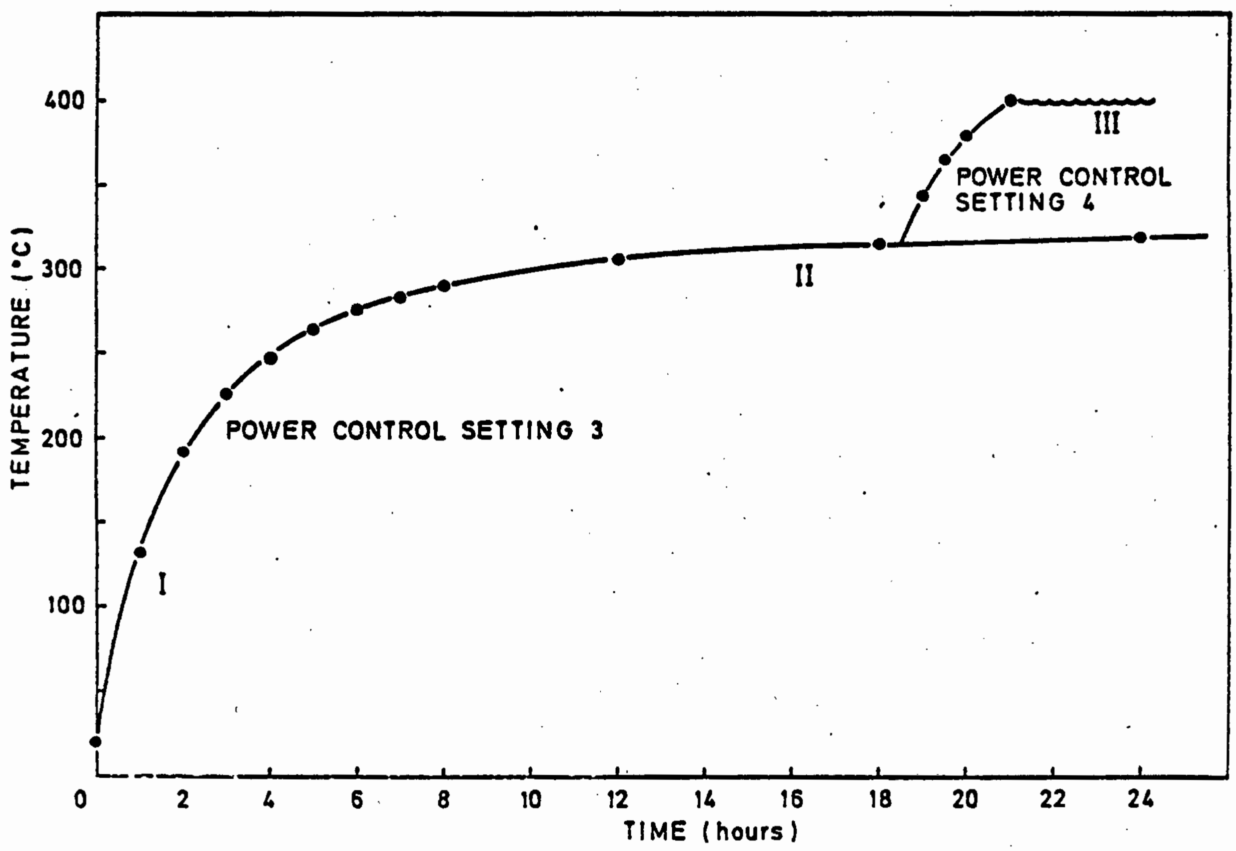

FIG : 4.20 Heating profile as a function of time and power controller setting (Section 4.5.2).

REFERENCES

1. HUTCHINGS, I.M.
Mechanical and Metallurgical aspects of the erosion of metals. Corrosion/Erosion of coal conversion system materials - Conference proceedings. Berkeley, California. January 24-26 1979.

2. WINTER, R E. HUTCHINGS, I.M.
Solid particle erosion studies using single angular particles. Wear, **29**, 1963, 181-194.

3. QUADIR, T. SHEWMON, P.
Solid particle erosion mechanisms in copper and two copper alloys. Metallurgical Transactions. ASM, **12A** July 1981.

4. NIAM, M. BAHADUR, S.
Workhardening in erosion due to single particle impacts. Wear of Materials 1983, 340-345.

5. MORSI, S.A. ALEXANDER, A.J.
An investigation of particle trajectories in 2-phase flow systems. Journal of Fluid Mechancis, 1972, **55**, Part 2 193-208.

6. SMELTZER, C.E. GULDEN, M. COMPTON, W.A.
Mechanisms of metal removal by impacting dust particles. Journal of Basic Engineering, **92**, 1970, 639-654.

7. FINNIE, I.
Erosion of Metals. Corrosion/erosion of coal conversion system materials - Conference proceedings. Berkeley, California, Jan. 24 -26 1979, 429-443.

8. GOODWIN, J.E. SAGE, W. TILLY, G.P.
Study of erosion by solid particles. Proceedings: Institute of Mechanical Engineers,1969/70, **184(1)** 279-292.

9. SUH, N.P.
Relationship of solid particle erosion to other types of wear. Corrosion/erosion of coal conversion system materials - Conference proceedings, Berkeley, California. Jan. 24-26 1979, 552-560.

10. SHEWMON, P.G.
Particle size threshold in the erosion of metals. Wear, **68**, 1981, 253-258.

11. FINNIE, I.
Some observations on the erosion of ductile metals. Wear, **19,** 1972, 81-90.

12. HEAD, W.J. HARR, M.E.
The development of a model to predict the erosion of materials by natural contaminants. Wear, **15,** 1970, 1-46.

13. BHATTACHARYYA, S. YATES, D. HILL, V.
Erosion/corrosion of materials in coal gasifier environments. Proceedings of 5th International conference on erosion by liquid and solid impact. Cambridge, Sept. 3-6, 1979. 451-459.

14. MILLS, D. MASON, J.S.
Analysis of factors influencing surface erosion patterns on bends in pneumatic conveying lines. Proceedings of 5th International Conference on Erosion by Liquid and Solid Impact, Cambridge, Sept. 3-6 1979, 51.1-51.10.

15. GAT, N. TABAKOFF, W.
Effects of temperature on the behaviour of metals under erosion by particulate matter. ASTM Journal July 1980, 177-186.

16. SHERMAN, M.M. ALEXANDER, E.C. HOPKINS, A.T.
The erosion performance of ceramic materials in a freestream dust environment. Proceedings of 5th International Conference on Erosion by Solid and Liquid Impact, Cambridge, Sept. 3-6 1979, 331-336.

17. HANSEN, J.S. KELLY, J.E. WOOD, J.W.
Erosion testing of potential valve material for coal gasification systems. Bureau of Mines Report of Investigations, BuMines RI 8335 of 1979.

18. LEVY, A. CHIK, P.
The effects of erodent composition and shape on the erosion of steel. Wear, **89,** 1983, 151-162.

19. SALIK, J. BUCKLEY, D.H.
The effect of mechanical surface and heat treatments on erosion resistance. Wear of Materials 1981, 592-596.

20. SÖDERBERG, S. HOGMARK, S. SWAHN,H.
Mechanisms of material removal during erosion of a stainless steel. American Society of Lubrication Engineers, 37th Annual meeting May 10-13, 1982.

21. GANE, N. MURRAY, M.J.
The transition from ploughing to cutting in erosive wear. Proceedings of 5th International Conference on Erosion by Liquid and Solid Impact, Cambridge, 3-6 Sept., 1979, 40.1-40.7

22. MOBBS, F.R. BOWERS, H.M. RICHES, D.M. COLE, B.N.
Influence of particle size distribution on the high speed flow of gas-solid suspensions in a pipe. Inst. of Mechanical Engineers : Proceedings 1969-1970, **184,** Part 3C.

23. SARGEANT, G.A. KESHAVEN, M.K. MEHROTRA, P.K. CONRAD, H.
The erosion of plain carbon steels by ash particles from a coal gasifier. Wear of Materials 1981, 613-618.

24. RAASK, E.
Impact erosion wear caused by pulverized coal and ash. Proceedings of 5th International Conference on Erosion by Solid and Liquid Impact, Cambridge, 3-6 Sept. 1979, 41.1-41.7.

25. ZAHAVI, J. SCHMITT, G.F.
Solid particle erosion of polymeric coatings. Wear, **71,** 1981, 191-210.

26. HUTCHINGS, I.M.
Mechanisms of erosion of metals by solid particles. Erosion : Prevention and Useful applications ASTM STP 664 (Ed. Adler, W.F.) 1979, 59-76.

27. MAJI, J. SHELDON, G.L.
Mechanisms of erosion of a ductile material by solid particles. Erosion : Prevention and Useful applications, ASTM STP 664 (Ed. Adler, W.F.) 1979, 136-147.

28. EDINGTON, J.W. WRIGHT, I.G.
Study of particulate damage in Haynes Stellite 6B: SEM of eroded surfaces. WEAR, **48,** 1978, 131-144.

29. RUFF, A.W. IVES, L.K.
Measurement of solid particle velocity in erosive wear. Wear, **35,** 1975, 195-199.

30. FINNIE, I. WOLAK, J. KABIL, Y.H.
Erosion of metals by solid particles. Journal of Materials, **12,** 1967, 682-700.

31. SÖDERBERG, S. HOGMARK, S. ENGMAN, U. SWAHN, H.
Erosion classification of materials using a centrifugal erosion tester. Tribology International, Dec. 1981, 333-343.

32. FOLEY, T. LEVY, A.
The effect of heat treatment on the erosion behaviour of steel. Wear of Materials 1983, 346-353.

33. LEVY, A. BAKKER, T.
Erosion behaviour of hard surface coatings/inserts. U.S. Department of Energy Report 1981, Contract number W-7405-ENG-48.

34. CONRAD, H. SHIN, Y. SARGEANT, G.A.
Erosion of sintered WC-Co alloys. Proceedings of International Conference on Recent Developments in Specialty Steels and Hard Materials, Pretoria, South Africa, Nov. 8-12 1982, 423-429.

35. BITTER, J.G.A.
A study of erosion phenomena - Part I. Wear, **6,** 1963, 5-21.

36. TILLY, G.P.
Erosion caused by airborne particles. Wear, **14,** 1969, 63-79.

37. TABAKOFF, W. WAKEMAN, T.
Test facility for material erosion at high temperature. Erosion : Preventation and Useful applications. ASTM STP 664 (Ed. Adler, E.F.), 1979, 123-135.

38. LAITONE, J.A.
Aerodynamic effects in the erosion process. Wear, **56,** 1979, 239-246.

39. DANYLUK, S. SLACK, W.J. PARK, J.Y. MAMOUN, M.M.
Solid particle erosion of a cyclone from a coal gasification pilot plant. Wear of Materials 1981, 619-624.

40. STRINGER, J.
Industrial experience and design requirements with respect to erosion and corrosion in coal conversion systems. Corrosion/Erosion of Coal Conversion System materials - Conference Proceedings, Berkeley, Calif., Jan. 24-26 1979, 14-60.

41. BARKALOW, R.H. PETIT, F.S.
Corrosion/Erosion of materials in coal combustion gas turbines. Corrosion/Erosion of Coal Conversion System materials - Conference Proceedings, Berkeley, Calif., Jan. 24-26 1979, 139-173.

42. BARKALOW, R.H. PETIT, F.S.
High temperature erosion and erosion-hot corrosion with various types of solid particles. Proceedings of 5th International Conference on Erosion by Liquid and Solid Impact, Cambridge, Sept. 3-6 1979, 44.1-44.9.

43. DAPKUNAS, S.J.
A summary of erosion experience in the U.S. Department of Energy's Coal conversion plants. Proceedings of 5th International Conference on Erosion by Liquid and Solid Impact, Cambridge, Sept. 3-6 1979, 43.1-43.14.

44. LEVY, A.V.
The role of plasticity in erosion. *Proceedings of 5th International Conference on Erosion by Liquid and Solid Impact*, Cambridge, Sept 3-6 1979, 39.1-39.10

45. HOCKEY, B.J. WIEDERHORN, S.M.
Erosion of ceramic materials : The role of plastic flow. *Proceedings of 5th International Conference on Erosion by Liquid and Solid Impact*, Cambridge, Sept. 3-6 1979, 26.1-26.9.

46. TABAKOFF, W. RAMACHANDRAN, J. HAMED, A.
Temperature effects on the erosion of metals used in turbo-machinery. *Proceedings of 5th International Conference on Erosion by Liquid and Solid Impact*, Cambridge, Sept. 3-6 1979, 47.1-47.5.

47. JONES, M.H. LEWIS, R.
Solid particle erosion of a selection of alloy steels. *Proceedings of 5th International Conference on Erosion by Liquid and Solid Impact*, Cambridge, Sept. 3-6 1979, 52.1-52-9.

48. GREEN, G.M. TAGGART, R. POLONIS, D.H.
Influence of microstructures on erosion of plain carbon steels. *Metallography*, **14**, 1981, 191-212.

49. FINNIE, I. LEVY, A. MCFADDEN, D.H.
Fundamental mechanisms of erosive wear of ductile materials by solid particles. *Erosion : Prevention and Useful Applications*, ASTM STP 664 (Ed. Adler, W.F.), 1979, 36-58.

50. RICKERBY, D.G.
Correlation of erosion with mechanical properties in metals. *Wear*, **84**, 1983, 393-395.

51. WRIGHT, I.G.
Solid particle erosion of oxidation-resistant alloys in high temperature, low velocity gas streams. *Proceedings of 5th International Conference on Erosion by Liquid and Solid Impact*, Cambridge, Sept. 3-6 1979, 46.

52. WRIGHT, I.G.
Corrosion/erosion of components in coal conversion environments. *Corrosion/Erosion of coal conversion system materials - Conference proceedings*, Berkeley, Calif., Jan. 24-26 1979, 103-138.

53. ZAMBELLI, G. LEVY, A.V.
Erosion of oxide scales on metal substrates. *Corrosion/Erosion of coal conversion system materials - Conference proceedings*, Berkeley, Calif., Jan. 24-26 1979, 480-551.

54. BROWN, R. JIN JUN, E. EDINGTON, J.W.
Mechanisms of erosive wear for 90° impact on copper and iron targets. Wear of Materials 1981, 1-13.

55. ENGMAN, U.
Results from high temperature erosion of ceramics. Wear of Materials 1983, 319-332.

56. BROWN, R. EDINGTON, J.W.
Occurence of melting during the solid particle erosion of copper. Wear, **73**, 1981, 193-200.

57. RAO, P.VEERHABHADRA RAO, B.C.SYAMALA
Similarities in different experiments of erosion caused by cavitation and liquid impingement. Journal of Testing and Evaluation ASTM, **9**, No.3, May 1981, 179-188.

58. HAMMARSTEN, A. SÖDERBERG, S. HOGMARK, S.
Erosion mechanisms studied by recovery and analysis of wear fragments. Wear of Materials 1983, 373-381.

59. MALKIN, S.
Correlation between solid particle erosion of metals and their melting energies. Wear, **68**, 1981, 391-396.

60. SHEWMON, P.G.
Mechanism of erosion of aluminium alloys. Proceedings of 5th International Conference on Erosion by Liquid and Solid Impact, Cambridge, Sept. 3-6 1979, 37.1-37.5.

61. RICKERBY, R.G. MACMILLAN, N.H.
Erosion of aluminium and magnesium oxide by spherical particles. Wear of Materials 1981, 548-563.

62. BELLMAN, R. LEVY, A.
Platelet mechanism of erosion of ductile metals. Wear of Materials 1981, 564-576.

63. BITTER, J.G.A.
A study of erosion phenomena - Part II. Wear, **6**, 1963, 169-190.

64. HUTCHINGS, I.M.
Some comments on the theoretical treatment of erosive particle impacts. Proceedings of 5th International Conference on Erosion by Liquid and Solid Impact, Cambridge, Sept. 3-6 1979, 36.1-36.6.

65. GULDEN, M.E.
Solid particle erosion of high technology ceramics (Si_3N_4, Glass bonded Al_2O_3, and MgF_2). *Erosion : Prevention and Useful applications*, ASTM STP 664 *(Ed. Adler, W.F.), 1979, 101-122.*

66. WRIGHT, I.G. SHETTY, D.K. CLAUER, A.H. STROPSKI, J.T.
Evaluation of advanced materials for slurry erosion service. *Testing programme report BCL-3.5*, Battelle, Ohio.

67. DEPARTMENT OF ENERGY NEWSLETTER
Materials selection for the SRC - I demonstration plant. *DOE Newsletter*, **No.46,** Oct. I 1983.

68. DANIELSON, J.A.
Air pollution Engineering Manual, U.S. Department of Health, Eductation and Welfare publication (1967).

69. BRAUER, H. VARMA, Y.B.G.
Air pollution control equipment, Springer-Verlag publication 1981.

70. RESENTE, A.C.
Characterization of coal ash and study of eroded metal surfaces. *MAT 410 project*, Department of Metallurgy and Materials Science, University of Cape Town, 1983.

71. BALL, A.
On the importance of work hardening in the design of wear resistant materials. Wear, **91,** 1983, 201-207